This is a repository copy of *Multiwavelength studies of MHD waves in the solar chromosphere: An overview of recent results*.

White Rose Research Online URL for this paper:
http://eprints.whiterose.ac.uk/86089/

Version: Accepted Version

Article:
Jess, D.B., Morton, R.J., Verth, G. et al. (3 more authors) (2015) Multiwavelength studies of MHD waves in the solar chromosphere: An overview of recent results. Space Science Reviews. Published Online 05 Mar 2015 . ISSN 0038-6308

https://doi.org/10.1007/s11214-015-0141-3

Reuse
Unless indicated otherwise, fulltext items are protected by copyright with all rights reserved. The copyright exception in section 29 of the Copyright, Designs and Patents Act 1988 allows the making of a single copy solely for the purpose of non-commercial research or private study within the limits of fair dealing. The publisher or other rights-holder may allow further reproduction and re-use of this version - refer to the White Rose Research Online record for this item. Where records identify the publisher as the copyright holder, users can verify any specific terms of use on the publisher's website.

Takedown
If you consider content in White Rose Research Online to be in breach of UK law, please notify us by emailing eprints@whiterose.ac.uk including the URL of the record and the reason for the withdrawal request.

eprints@whiterose.ac.uk
https://eprints.whiterose.ac.uk/

Space Science Reviews **DOI 10.1007/s11214-015-0141-3** **manuscript No.**
(will be inserted by the editor)

Multiwavelength studies of MHD waves in the solar chromosphere

An overview of recent results

D. B. Jess, R. J. Morton, G. Verth, V. Fedun,
S. D. T. Grant & I. Giagkiozis

arXiv:1503.01769v2 [astro-ph.SR] 11 Mar 2015

Received: 7 November 2014 / Accepted: 15 February 2015

Abstract The chromosphere is a thin layer of the solar atmosphere that bridges the relatively cool photosphere and the intensely heated transition region and corona. Compressible and incompressible waves propagating through the chromosphere can supply significant amounts of energy to the interface region and corona. In recent years an abundance of high-resolution observations from state-of-the-art facilities have provided new and exciting ways of disentangling the characteristics of oscillatory phenomena propagating through the dynamic chromosphere. Coupled with rapid advancements in magnetohydrodynamic wave theory, we are now in an ideal position to thoroughly investigate the role waves play in supplying energy to sustain chromospheric and coronal heating. Here, we review the recent progress made in characterising, categorising and interpreting oscillations manifesting in the solar chromosphere, with an impetus placed on their intrinsic energetics.

Keywords Sun: compressible waves · Sun: incompressible waves · Sun: chromosphere · Sun: spicules · plasma wave heating

D. B. Jess & S. D. T. Grant
Astrophysics Research Centre
School of Mathematics and Physics
Queen's University Belfast
Belfast BT7 1NN, Northern Ireland, UK
E-mail: d.jess@qub.ac.uk, sgrant19@qub.ac.uk

R. J. Morton
Department of Mathematics & Information Sciences
Northumbria University
Newcastle Upon Tyne, NE1 8ST, UK
E-mail: richard.morton@northumbria.ac.uk

G. Verth & I. Giagkiozis
Solar Physics and Space Plasma Research Centre (SP^{2}RC)
The University of Sheffield
Hicks Building, Hounsfield Road
Sheffield, S3 7RH, UK
E-mail: g.verth@sheffield.ac.uk, i.giagkiozis@sheffield.ac.uk

V. Fedun
Space Systems Laboratory
Department of Automatic Control and Systems Engineering
University of Sheffield
Sheffield, S1 3JD, UK
E-mail: v.fedun@sheffield.ac.uk

I. Giagkiozis
Complex Optimization and Decision Making Laboratory
Automatic Control and Systems Engineering Department
University of Sheffield
Sheffield, S1 3JD, UK
E-mail: i.giagkiozis@sheffield.ac.uk

1 Introduction

Ever since the Sun's corona was found to be dominated by emission lines characteristic of multi-million degree temperatures, it was obvious that the heating of the plasma was not dominated by purely thermodynamic processes. As a result, research quickly built momentum in an attempt to understand which non-thermal processes, especially those of magnetic origin, were responsible for the continual supply of energy. This has since become known as the "coronal heating problem". Over the years, efforts to provide a conclusive heating mechanism for the outer solar atmosphere have produced two (seemingly) distinct classes of theory: magnetic reconnection and waves. In the former, it is suggested that regular reconfigurations of the embedded magnetic field lines will produce extreme localised heating through the conversion of magnetic energy into heat (Priest 1986; Priest & Schrijver 1999). Large-scale flare events are one of the most dramatic eruptive phenomena on our Sun that can be triggered by magnetic reconnection, often releasing in excess of 10^{31} ergs of energy during a single event. However, the relative rarity of these large-scale flares means that they cannot provide the necessary basal heating that the outer solar atmosphere requires to maintain its multi-million degree temperatures. Instead, it has been suggested that rapidly occurring, small-scale flare events, or "nanoflares" with individual energies $\sim 10^{24}$ ergs, may occur with such regularity in the solar atmosphere that they can provide the continual source of heat required to maintain the elevated temperatures (Parker 1988). Unfortunately, however, the small spatial sizes and radiative signatures of such events places them within or below the noise threshold of current observations (Terzo et al. 2011), and therefore only tentative evidence exists to support their presence in the outer solar atmosphere (Klimchuk & Cargill 2001; Bradshaw et al. 2012; Testa et al. 2013; Jess et al. 2014).

On the other hand, wave heating theories can be substantiated by a vast number of publications detecting oscillatory phenomena throughout the solar atmosphere since the early 1960s (Leighton 1960; Leighton et al. 1962; Noyes & Leighton 1963). Purely wave-based heating requires that waves, generated near the solar surface through the continual convective churning of plasma, propagate upwards, dissipate a considerable portion of their energy in the chromosphere, and *still* have sufficient energy remaining to heat the corona. However, the solar atmosphere is highly magnetic in nature. Localised magnetic field strengths often exceed 1000 G, and can even exceed 6000 G in extreme cases (Livingston et al. 2006), resulting in the oscillatory modes becoming highly modified, producing anisotropic waves that can be accurately modelled using magnetohydrodynamic (MHD) approximations (Roberts 1981a,b; Edwin & Roberts 1983; Cally 1986; Hasan & Sobouti 1987; Goossens et al. 1992; Nakariakov & Roberts 1995; Erdélyi & Fedun 2006a,b, 2007b, 2010; Verth et al. 2008, to name but a few). In the MHD approximation there exist three types of waves, Alfvén (see Figure 5), *fast* and *slow* magnetoacoustic waves (Figure 1; Erdélyi 1997; Zhugzhda & Nakariakov 1999; Nakariakov & Verwichte 2005). A number of wave modes have been observed at discrete layers of the solar atmosphere, ranging from the deepest depths of the photosphere through to the outermost extremities of the corona (Ulrich 1970; Penn & Labonte 1993; Aschwanden et al. 1999, 2002, 2004; Nakariakov et al. 1999; Ballai et al. 2011; Morton et al. 2011; Scullion et al. 2011; Jess et al. 2012c; Srivastava et al. 2013; Luna et al. 2014, to name but a few of the hundreds of examples to date). However, the goal is now to utilise multiwavelength observations to be able to track the waves as a function of height, ultimately allowing researchers to diagnose changes in wave energy and look for the corresponding signatures of localised atmospheric heating. In the past flare and wave heating mechanisms have often been considered as opposing and deeply conflicting viewpoints. However, in more recent years with the advent of higher sensitivity instrumentation, it has become apparent that not only can eruptive flare events trigger oscillatory phenomena (e.g., Verwichte et al. 2004; Wang & Solanki 2004; De Moortel & Brady 2007; Van Doorsselaere et al. 2007, 2009a; Jess et al. 2008b; Luna et al. 2008; Srivastava & Goossens 2013; Yuan et al. 2013), but that waves interacting with magnetic field lines can also induce the instabilities necessary to incite reconnective phenomena (e.g., Isobe & Tripathi 2006; Isobe et al. 2007; Jess et al. 2010a; Li & Zhang 2012; Jackiewicz & Balasubramaniam 2013; Shen et al. 2014). Furthermore, Chen et al. (2010, 2011) have also demonstrated how MHD waves can be initiated within large-scale coronal streamers following the impact of a rapidly propagating coronal mass ejection, suggesting how oscillatory motion can be triggered over an incredibly wide range of spatial scales. Therefore, it does not seem inconceivable that the once opposing viewpoints may actually work in harmony to sustain the basal heating required to balance atmospheric radiative losses.

While the majority of research over the last 70 years has been dedicated to the understanding of multi-million degree coronal signatures, it is the solar chromosphere that provides more tantalising prospects for rapid advancements in astrophysical understanding. Even though the chromosphere is only a thin layer spanning approximately 1000 km, it may play a pivotal role in our understanding by acting as the interface between the relatively cool photospheric plasma and the super-heated corona. Furthermore, whilst the chromosphere is only heated to a few thousand degrees above the corresponding photospheric layer, the relatively high densities found within the chromosphere, compared to those in the corona, means that it requires at least double the energy input to balance its radiative losses (Table 1, Withbroe & Noyes 1977; Anderson & Athay 1989). Typical chromospheric radiative losses are on the order of 10^6–10^7 $\mathrm{erg\,cm^{-2}\,s^{-1}}$ (or 1000–10 000 $\mathrm{W\,m^{-2}}$), compared with values of 10^4–10^6 $\mathrm{erg\,cm^{-2}\,s^{-1}}$ (or 10–1000 $\mathrm{W\,m^{-2}}$) for the solar corona

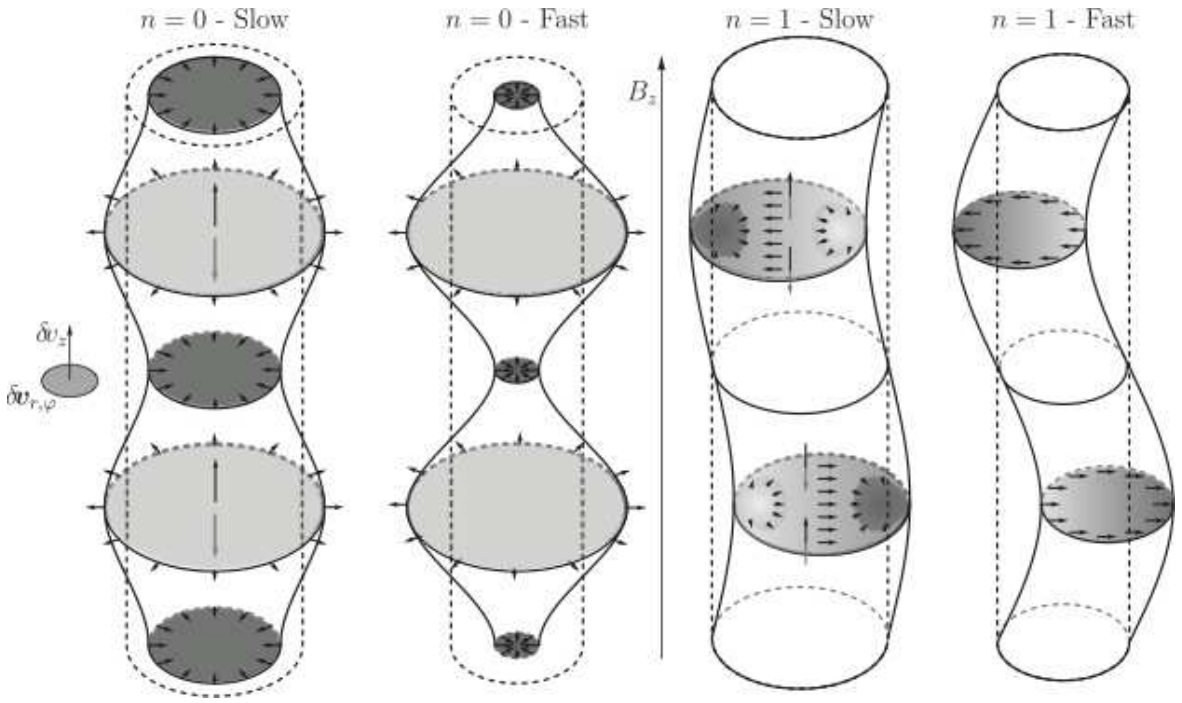

Fig. 1 Schematic diagrams of MHD waves in synthetic cylindrical waveguides. The velocity perturbations in the z direction, denoted by δv_z, are depicted by vertical arrows within the tube while the velocity perturbations in the (r, φ)-plane, $\delta \boldsymbol{v}_{r,\varphi}$, are illustrated using horizontal arrows. The horizontal plane cuts on the flux tubes illustrate the density perturbations, with darker and brighter shades signifying higher and lower densities, respectively, with respect to equilibrium. The two schematics to the left represent slow and fast sausage modes (with azimuthal wavenumber $n = 0$), while the two figures to the right represent slow and fast kink modes ($n = 1$). Notice that for the slow modes the main component of the velocity perturbation is in the z direction (plasma-$\beta < 1$), which is associated with, in contrast to the fast modes, stronger density perturbations.

(Withbroe & Noyes 1977). As a consequence, the solar chromosphere is universally recognised as an important layer when attempting to constrain any potential energy transfer mechanisms between the photosphere and the corona.

Seismological approaches have long been used to characterise solar atmospheric structuring through the analysis of propagating and standing wave motion. Dating back to the mid 1970s, the first detection of a truly global solar pressure oscillation inspired researchers to use such data to investigate the properties of the solar interior, hence initiating the field of helioseismology (Hill & Stebbins 1975; Brown et al. 1978). Then, following the launch in the 1990s of (at the time) high resolution satellite imagers capable of observing the Sun's corona, numerous examples of wave and oscillatory behaviour were detected through EUV diagnostics (e.g., Ofman et al. 1997; Deforest & Gurman 1998; Aschwanden et al. 1999; Nakariakov et al. 1999, to name but a few of the early examples). This led researchers to probe the detected oscillatory phenomena in order to better understand coronal parameters that were unresolvable using traditional imaging and/or spectroscopic approaches, thus creating the field of coronal seismology (see, e.g., the review paper by Nakariakov & Verwichte 2005). Coronal seismology has proven to be a powerful tool, with vast numbers of high-impact publications produced to date, including those related to the uncovering of magnetic fields (Nakariakov & Ofman 2001), energy transport coefficients (Aschwanden et al. 2003) and sub-resolution fine-scale structuring (King et al. 2003). Ultimately, the goal is to employ such seismological techniques in order to better understand the energy dissipation rates within the corona, and therefore determine the specific role MHD wave and oscillatory phenomena play in providing heat input to the outer solar atmosphere. Of course, a natural extension is to apply such innovative approaches to the solar chromosphere, a region that is rife with ubiquitous wave activity. This form of analysis has only recently risen to the forefront of chromospheric research, aided by the recent advancements made in telescope facilities, instrumentation and theoretical knowledge.

From a purely theoretical and modelling point of view, the chromosphere presents a substantially different plasma environment for MHD wave modes compared to the corona. The coronal plasma regime modelled for such waves often assumes a one-fluid, low plasma-beta and fully-ionized plasma. In contrast, realistic MHD modelling of chromosphere should be multi-fluid, finite plasma-beta and include the additional effects of partial ionisation and radiative transfer under non-local thermodynamic equilibrium (non-LTE) conditions (Hansteen et al. 2007). However, even in this more complex plasma environment, on observable MHD time/length scales, the particular defining properties of different wave

Table 1 Energy losses experienced in quiet Sun, coronal hole and active region locations at both coronal and chromospheric heights. Regardless of the solar location it is the chromosphere that displays the greatest energy losses. Table adapted from Withbroe & Noyes (1977).

Parameter	Quiet Sun	Coronal hole	Active region
Transition layer pressure (dyn cm^{-2})	2×10^{-1}	7×10^{-2}	2
Coronal temperature (K at $r \approx 1.1\ R_{\odot}$)	$1.1 - 1.6 \times 10^{6}$	10^{6}	2.5×10^{6}
Coronal energy losses (erg cm^{-2} s^{-1})			
Conductive flux F_c	2×10^{5}	6×10^{4}	$10^{5} - 10^{7}$
Radiative flux F_r	10^{5}	10^{4}	5×10^{6}
Solar wind flux F_w	$< 5 \times 10^{4}$	7×10^{5}	$< 10^{5}$
Total corona loss $F_c + F_r + F_w$	3×10^{5}	8×10^{5}	10^{7}
Chromospheric radiative losses (erg cm^{-2} s^{-1})			
Low chromosphere	2×10^{6}	2×10^{6}	$> 10^{7}$
Middle chromosphere	2×10^{6}	2×10^{6}	10^{7}
Upper chromosphere	3×10^{5}	3×10^{5}	2×10^{6}
Total chromospheric loss	4×10^{6}	4×10^{6}	2×10^{7}

modes in fine-scale magnetic flux tubes remain unchanged. However, such modes, including torsional Alfvén, sausage and kink, could be subject to frequency-dependent effects not encountered in the corona (e.g., ion-neutral damping; Soler et al. 2013, 2015). This has important implications for understanding the true nature of wave-based heating in the chromosphere. Furthermore, such frequency dependent effects must also be taken into account when performing remote plasma diagnostics from MHD wave mode observations, i.e., *chromospheric seismology*.

Over the last decade there has been a significant number of reviews published that document the abundance of MHD wave phenomena in the outer solar atmosphere. Such detailed overviews include quasi-periodic (Nakariakov et al. 2005), standing (Wang 2011), magnetoacoustic (Van Doorsselaere et al. 2009b; De Moortel 2009) and Alfvén (Mathioudakis et al. 2013) waves. However, the majority of these reviews are solely focused on coronal oscillations, and as a result, choose to ignore the presence of MHD waves occurring in the lower regions of the solar atmosphere. Older review articles have touched on the manifestation of waves and oscillations in the solar chromosphere, including those that discussed observations of spicules (Zaqarashvili & Erdélyi 2009), filaments (Lin 2011) and more-general chromospheric plasma (e.g., Frisch 1972; Bonnet 1981; Narain & Ulmschneider 1990, 1996; Taroyan & Erdélyi 2009). However, since the confirmation of omnipresent waveforms in the chromosphere is a relatively recent achievement, until now there has been a distinct lack of a dedicated and wide-ranging review article that details both the observational and theoretical advancements made in chromospheric wave studies. As a result, we now take the opportunity to gather recent observational and theoretical publications and provide the solar physics community with a thorough overview of ubiquitous MHD wave phenomena intrinsic to the solar chromosphere.

2 Observational & Theoretical Difficulties

Even though the Sun's chromosphere has been identified as a key area of interest by the solar physics community, it is unfortunately an incredibly difficult portion of the atmosphere to observe and interpret efficiently. Firstly, the chromosphere is predominantly observed through a collection of deep absorption lines in the optical portion of the electromagnetic spectrum. These features include the Fraunhofer absorption lines of Ca II H & K ($3933 - 3968$ Å), Mg I $b_{1,2,4}$ ($5167 - 5184$ Å), Hβ (4861 Å), Na I $D_{1,2}$ ($5889 - 5895$ Å) and Hα (6563 Å), in addition to some near-UV and UV spectral signatures such as the Mg II *h* & *k* lines ($2795 - 2803$ Å), the C IV resonant doublet ($1548 - 1550$ Å) and H I Lα (1216 Å). Observing such deep, dark optical absorption cores results in minimal light levels reaching the telescope detectors once atmospheric (if using a ground-based facility), telescope, lens, filter and camera transmission factors have been taken into consideration. Jess et al. (2010c) derived photon count-rate statistics for a number of chromospheric spectral profiles and indicated that $\ll 1\%$ of the incident flux on Earth's atmosphere is converted into counts at the imaging detector. As a result, longer exposure times need to be employed to maintain adequate signal-to-noise ratios. This can have the adverse effect of blurring any rapidly evolving underlying chromospheric features such as spicules, mottles, fibrils and jets. Furthermore, it is impossible (engineering wise) to fabricate an infinitesimally narrow bandpass filter that would only capture the deepest core of the chromospheric spectral line. Typical Lyot–type filter widths are on the order of 200 mÅ FWHM, with some more specialised spectral imagers including the Interferometric BIdimensional Spectrometer (IBIS; Cavallini 2006) and the CRisp Imaging SpectroPolarimeter (CRISP; Scharmer et al. 2008) achieving pass-bands as narrow as 50 mÅ FWHM. Nevertheless, line core intensities often contain significant photospheric flux leaking into the filter pass-bands, creating a complex puzzle as to which features and measurements correspond to photospheric and/or chromospheric structures (Hall 2008). To complicate matters yet further, upwardly or downwardly propagating material will induce intrinsic Doppler shifts into the spectroscopic line profiles, thus causing the static wavelength filters to sample features far out into the spectral wings (which contain significant photospheric continua), rather than the true chromospheric absorption core. Indeed, employing a narrowband (80 mÅ) Lyot filter capable of imaging the wings of both the Hβ Fraunhofer and Ba II 4554 Å resonance lines, Sütterlin et al. (2001) revealed how such Doppler shifts permeate all high-resolution lower atmospheric observations, thus complicating the source of fine-scale intensity fluctuations.

Chromospheric densities experience a significant decrease from their corresponding photospheric counterparts, and as a result radiative transition rates generally dominate over collisional rates (Uitenbroek & Briand 1995; Uitenbroek 1997, 2001, 2002). This makes the chromosphere a non-local thermodynamic equilibrium (non-LTE) environment, resulting in the need for full radiative transfer modelling of all simulated processes. Moving away from 1D hydrostatic models, Klein et al. (1976, 1978) and Carlsson & Stein (1992, 1995, 1997), to name but a few, have demonstrated the strenuous computational requirements necessary for efficient 1D modelling in full non-LTE. However, as time progressed, it became clear that even 2D non-LTE models (e.g., van Noort et al. 2002; Carlsson & Leenaarts 2012) of the solar atmosphere were not entirely representative of the observed chromospheric structures (de la Cruz Rodríguez et al. 2012; Leenaarts et al. 2012). In the modern era, full 3D non-LTE modelling has only been made possible by the continual computational improvements in both speed and storage delivered to end users. Nevertheless, even 3D non-LTE simulations of chromospheric processes have significant caveats attached, manifesting as uncertainties in the multi-level atomic transitions, atmospheric mixing-lengths, non-gray radiative transfer components and sensitivities to asymmetric spectral line profiles (Cuntz et al. 2007; Caffau et al. 2011; Beeck et al. 2012; Leenaarts et al. 2012; Prakapavičius et al. 2013). Therefore, while the use of 3D non-LTE simulations to assist with the interpretation of chromospheric phenomena and wave energy transportation is beneficial, the complex nature of the chromosphere itself introduces considerable difficulties when attempting to efficiently and accurately diagnose basal heating contributions.

The solar chromosphere also introduces observational difficulties through its collection of incredibly diverse, rapidly evolving structures covering spatial scales ranging from sub-arcsecond (e.g., spicules, mottles, fibrils, etc.) through to those in excess of many hundreds of arcseconds (e.g., filaments; Figure 2). Not only does the chromosphere comprise of structures covering a vast spread of spatial scales, but it also displays signatures of supersonic motion and high-frequency oscillatory phenomena in the forms of evaporated material (e.g., Acton et al. 1982; Antonucci et al. 1984, 1985; Keys et al. 2011a) and magnetically guided compressible and incompressible waves (De Pontieu et al. 2004, 2007a, 2011; Erdélyi & Fedun 2007a; Jess et al. 2009; McIntosh et al. 2011; Morton et al. 2012, to name but a few of the more recent high-impact articles). Our present fleet of telescopes able to observe the solar chromosphere includes the 0.5 m Solar Optical Telescope (SOT; Tsuneta et al. 2008a; Suematsu et al. 2008) onboard the Hinode spacecraft (Kosugi et al. 2007), the 0.76 m Dunn Solar Telescope (DST; formerly the Vacuum Tower Telescope; Dunn 1969) in New Mexico, USA, the 1 m Swedish Solar Telescope (SST; Scharmer et al. 2003) on the island of La Palma, the 1 m New Vacuum Solar Telescope (NVST; Liu et al. 2014a) at the Fuxian Solar Observatory, China, the 1.5 m GREGOR telescope (Schmidt et al. 2012) at the Teide Observatory, Tenerife, and the 1.6 m New Solar Telescope (NST; Cao et al. 2010) at

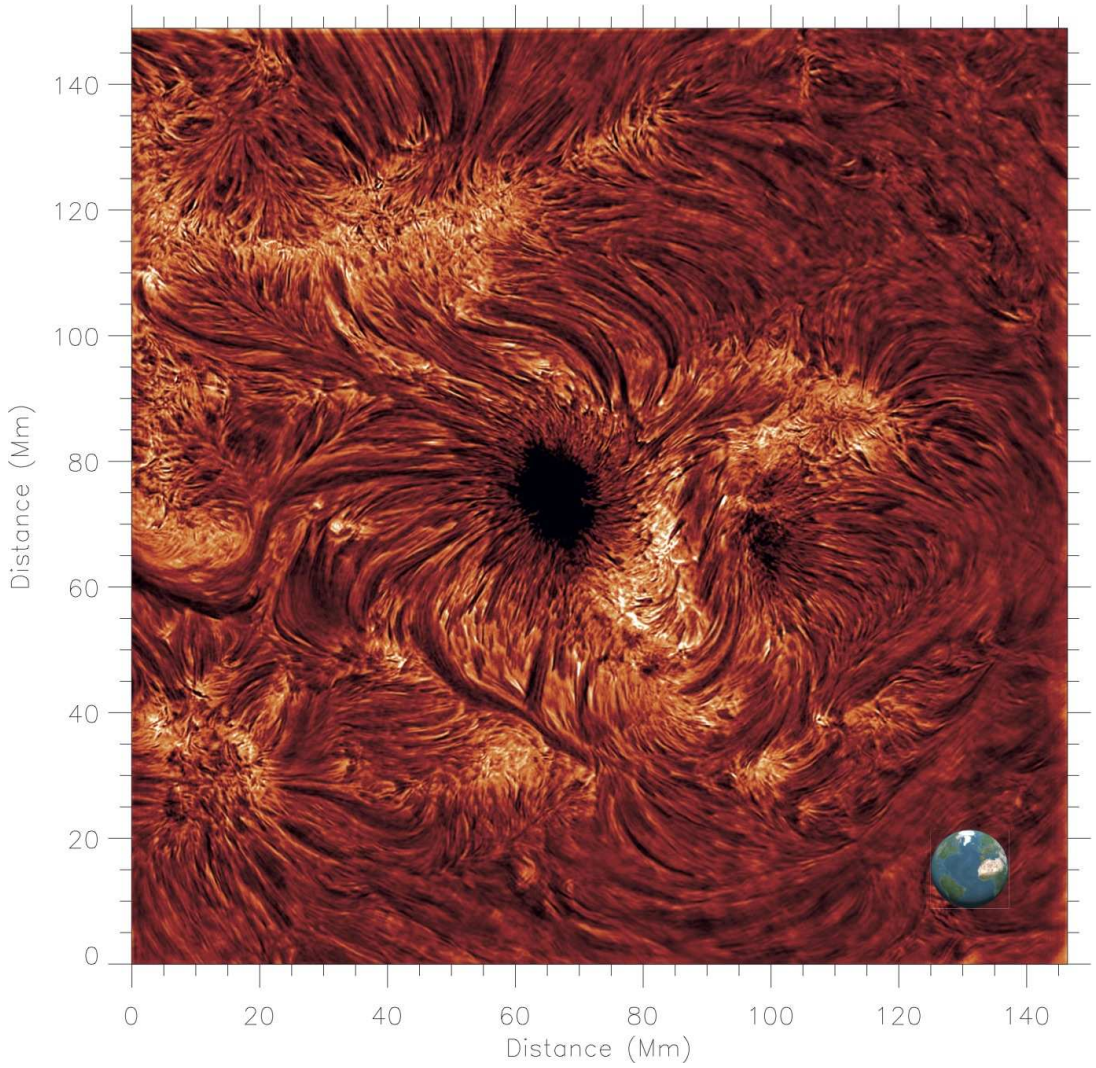

Fig. 2 An image of a solar active region acquired through a narrowband 0.25 Å Hα-core filter. Employing a new generation of large format, low noise CMOS sensors, it is now possible to obtain chromospheric fields-of-view in excess of $200'' \times 200''$ (at the diffraction limit) with frame rates exceeding $60\ \mathrm{s}^{-1}$. A scale representation of the Earth is depicted in the lower-right section of the image. This snapshot, courtesy of D. B. Jess, was acquired using an Andor Technology 4.2 MP Zyla CMOS detector (15 ms exposure time at a frame rate of $64\ \mathrm{s}^{-1}$) at the Dunn Solar Telescope, NM, USA.

the Big Bear Solar Observatory (BBSO; Zirin 1970) in California, USA. Each facility has its own unique merits, some of which include high-cadence multiwavelength imaging, spectropolarimetric imaging, high resolution spectrographic instrumentation, high-order adaptive optics, and those in locations with excellent year-round observing conditions. The current suite of solar telescopes capable of observing the chromosphere have revolutionised our understanding of small-scale dynamic processes occurring within the interface between the relatively cool photosphere and the super-heated multi-million degree corona. It is not uncommon for these facilities to be able to obtain full spectral imaging scans of chromospheric absorption profiles (e.g., Ca II, Hα, etc.) in as little as a few seconds (Figure 3), diffraction-limited narrowband imaging of deep absorption line cores at frame rates exceeding $40\,\mathrm{s}^{-1}$, and spectral resolutions ($\frac{\lambda}{\delta\lambda}$) exceeding $500\,000$ at wavelengths covering the optical through to the near-infrared. However, even with these powerful telescopes employing modern detectors and instrumentation, there is clear evidence to suggest that there are still lower-atmospheric phenomena manifesting below our currently imposed resolution limits (von Uexkuell & Kneer 1995; Lagg et al. 2007; Jess et al. 2008a; Cauzzi et al. 2008, 2009; Socas-Navarro et al. 2009; Vourlidas et al. 2010; Andić et al. 2013). Thus, for the last number of years there has been an impetus placed on further developing the spatial, temporal and spectral resolutions of our ground- and space-based solar facilities. The solar physics community eagerly awaits the arrival of the first next-generation high-resolution facilities, including the $2\,\mathrm{m}$ National Large Solar Telescope (NLST; Hasan et al. 2010) in Ladakh, India, and the $4\,\mathrm{m}$ Daniel K. Inouye Solar Telescope (DKIST, formerly the Advanced Technology

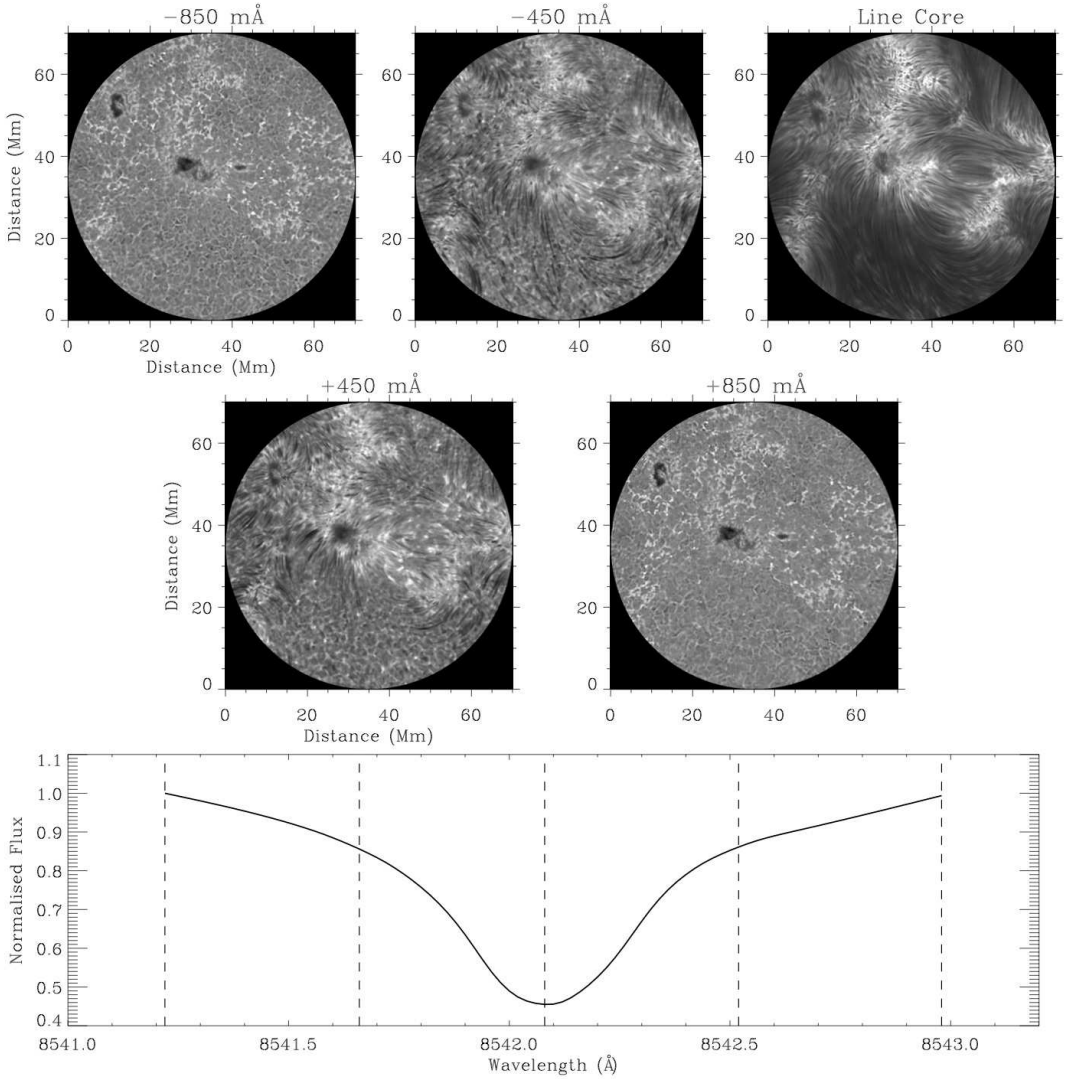

Fig. 3 A spectral imaging scan, taken by the IBIS instrument on 2011 December 10 across the Ca II absorption line at 8542 Å, revealing a collection of magnetic pore structures. The panels display the corresponding intensity images at specific wavelength positions corresponding to the Ca II line core −850 mÅ (upper-left), −450 mÅ (upper-middle), ±0 mÅ (upper-right), +450 mÅ (middle-left) and +850 mÅ (middle-right), respectively. The lower panel shows an 'at rest' Ca II profile where the vertical dashed lines indicate the wavelength positions used to capture the sequence of images displayed in the upper panels. Note how the chromosphere reveals itself as the imaging wavelength approaches the deepest part of the absorption profile. Images based on the data presented by Jess et al. (2014).

Solar Telescope, ATST; Keil et al. 2003; Rimmele et al. 2010) atop the Haleakalā volcano on the Pacific island of Maui, due to receive first light in 2018 and 2019, respectively. Through drastically increased aperture sizes, chromospheric structures down to ~ 20 km in size will be able to be detected, tracked and studied in unprecedented detail.

While we await the final stages of construction on these revolutionary facilities we can continue pushing the boundaries of scientific understanding by employing current generation of telescopes in novel ways. In this review we will detail recent observations and theoretical interpretations of oscillatory phenomena found to be propagating through the solar chromosphere. Due to the cutting-edge research being undertaken around the world in an attempt to address the long-standing question of how energy and heat manages to pass through the chromosphere on its way to the corona, often the observations and interpretations put forward by solar physicists can be anecdotal and fraught with overzealous assumptions. Nevertheless, without somewhat speculative conclusions the research field would not be advancing at the rate it is today as researchers attempt to verify or refute the hypotheses put forward. In this review we will attempt an objective overview of recent observational and theoretical wave developments, and try to place each scientific result in the context of atmospheric heating constraints. In the following section we will summarise the most important theoretical results that form the foundation knowledge upon which we can start interpreting observed chromospheric waves.

3 Theory of Linear MHD Waves

3.1 Linearising the Ideal MHD Equations

In the absence of a magnetic field, the supported plasma eigenmodes are sound waves which are isotropic (i.e., their speed is independent of the direction of propagation) and non-dispersive. However, in the presence of a magnetic field the number of supported waves is dramatically increased. Importantly, although some of these waves have similarities with sound waves, they can be highly anisotropic. This is because their characteristics depend on the degree of alignment of the wavevector ($\boldsymbol{k}$) with the direction of the background magnetic field ($\boldsymbol{B}_0$), and the ratio of the kinetic pressure (p_0) to the magnetic pressure ($\boldsymbol{B}_0^2/2\mu_0$). This ratio is the plasma-β, defined as $\beta = 2\mu_0 p_0/\boldsymbol{B}_0^2$, where μ_0 is the magnetic permeability of free space. A commonly used method to explore the properties of waves in magnetised plasmas is to consider the linearised ideal MHD equations. Let us consider small perturbations about a static equilibrium (i.e., no background flow) where $\boldsymbol{v}_0 = \boldsymbol{0}$,

$$\frac{\partial}{\partial t}\delta\rho = -\nabla\cdot(\rho_0\delta\boldsymbol{v}), \tag{1a}$$

$$\rho_0\frac{\partial}{\partial t}\delta\boldsymbol{v} = -\nabla\delta p + \frac{1}{\mu_0}\left[(\nabla\times\boldsymbol{B}_0)\times\delta\boldsymbol{B} + (\nabla\times\delta\boldsymbol{B})\times\boldsymbol{B}_0\right], \tag{1b}$$

$$\nabla\delta p = v_S^2\nabla\delta\rho, \tag{1c}$$

$$\frac{\partial}{\partial t}\delta\boldsymbol{B} = \nabla\times(\delta\boldsymbol{v}\times\boldsymbol{B}_0), \tag{1d}$$

where ρ_0, p_0 and $\boldsymbol{B}_0$ are the density, kinetic pressure and magnetic field quantities at equilibrium, with all being functions of the spatial coordinates. Furthermore, $\delta\rho$, δp and $\delta\boldsymbol{B}$ are the corresponding perturbed quantities, while $\delta\boldsymbol{v}$ is the velocity perturbation and $v_S = \sqrt{\gamma p_0/\rho_0}$ is the adiabatic sound speed, and, γ is the ratio of specific heats.

3.2 Wave Modes in a Uniform Unbounded Magnetized Plasma

Now let us explore the equations in Equation 1 in a very simple setting to illustrate the identifying characteristics of MHD wave modes. For an unbounded, homogeneous and magnetised plasma, p_0, ρ_0 and $\boldsymbol{B}_0$ are constant, resulting in Equation 1 being rewritten as (Priest 2014),

$$\frac{\partial}{\partial t}\delta\rho = -\rho_0\nabla\cdot(\delta\boldsymbol{v}), \tag{2a}$$

$$\rho_0\frac{\partial}{\partial t}\delta\boldsymbol{v} = -\nabla\left(\delta p + \frac{\boldsymbol{B}_0\cdot\delta\boldsymbol{B}}{\mu_0}\right) + \frac{1}{\mu_0}\nabla\cdot(\boldsymbol{B}_0\delta\boldsymbol{B}), \tag{2b}$$

$$\nabla\delta p = v_S^2\nabla\delta\rho, \tag{2c}$$

$$\frac{\partial}{\partial t}\delta\boldsymbol{B} = (\boldsymbol{B}_0\cdot\nabla)\delta\boldsymbol{v} - \boldsymbol{B}_0(\nabla\cdot\delta\boldsymbol{v}), \tag{2d}$$

where the two terms in the right hand side of the momentum equation Equation 2b are the total pressure perturbation,

$$\delta p_T = \delta p + \boldsymbol{B}_0\cdot\delta\boldsymbol{B}/\mu_0, \tag{3}$$

comprised of the perturbation of the kinetic pressure, δp, and the magnetic pressure perturbation, $\boldsymbol{B}_0\cdot\delta\boldsymbol{B}/\mu_0$. The second term in right hand side of Equation 2b is the magnetic tension. Considering plane wave solutions for the perturbed quantities,

$$\delta\boldsymbol{v}, \delta\boldsymbol{B}, \delta p, \delta\rho \propto e^{i(\boldsymbol{k}\cdot\boldsymbol{x}-\omega t)}, \tag{4}$$

where $\boldsymbol{x}$ is the position vector and $\boldsymbol{k}$ is the wavevector, the equations in Equation 2 can be combined to produce a dispersion relation. Specifically, there exist two possibilities: (*i*) $\boldsymbol{k}\cdot\delta\boldsymbol{v} = 0$ which corresponds to the incompressible case, and, (*ii*) $\boldsymbol{k}\cdot\delta\boldsymbol{v} \neq 0$ that corresponds to the compressible case. Using Equation 2 and $\boldsymbol{k}\cdot\delta\boldsymbol{v} = 0$, we arrive at the following dispersion relation in terms of the phase speed, $v_{ph} = \omega/k$ (where $k = |\boldsymbol{k}|$), and the angle, θ, between the wavevector, $\boldsymbol{k}$, and the background magnetic field, $\boldsymbol{B}_0$,

$$\begin{aligned} v_{ph}^2 &= \frac{\boldsymbol{B}_0^2}{\mu_0\rho_0}\cos^2\theta \\ &= v_A^2\cos^2\theta, \end{aligned} \tag{5}$$

Table 2 Phase speeds of the slow, fast and Alfvén waves for a uniform unbounded magnetised plasma.

		$\beta \gg 1, v_A \ll v_S$	$\beta \ll 1, v_A \gg v_S$
$\boldsymbol{k} \cdot \delta\boldsymbol{v} = 0$	$\boldsymbol{k} \| \boldsymbol{B}_0$	Alfvén wave, $v_{ph}^2 \sim v_A^2$	Alfvén wave, $v_{ph}^2 \sim v_A^2$
	$\boldsymbol{k} \perp \boldsymbol{B}_0$	Alfvén wave – does not propagate	Alfvén wave – does not propagate
$\boldsymbol{k} \cdot \delta\boldsymbol{v} \neq 0$	$\boldsymbol{k} \| \boldsymbol{B}_0$	Fast wave, $v_{ph}^2 \sim v_S^2$ approximately isotropic magnetic and kinetic pressure in phase Slow wave, $v_{ph}^2 \sim v_A^2$ magnetic and kinetic pressure out of phase	Fast wave, $v_{ph}^2 \sim v_A^2$ approximately isotropic magnetic and kinetic pressure in phase Slow wave, $v_{ph}^2 \sim v_S^2$ magnetic and kinetic pressure out of phase
	$\boldsymbol{k} \perp \boldsymbol{B}_0$	Fast wave, $v_{ph}^2 \sim v_S^2$ approximately isotropic magnetic and kinetic pressure in phase Slow wave – does not propagate	Fast wave, $v_{ph}^2 \sim v_A^2$ approximately isotropic magnetic and kinetic pressure in phase Slow wave – does not propagate

which is an anisotropic, non-dispersive wave whose only restoring force is the magnetic tension. The phase speed in Equation 5 corresponds to phase speed of the Alfvén wave (Alfvén 1942), where $v_A = |\boldsymbol{B}_0|/\sqrt{\mu_0 \rho_0}$. In the compressible case ($\boldsymbol{k} \cdot \delta\boldsymbol{v} \neq 0$) the system of equations in Equation 2 can be combined producing the following dispersion equation,

$$v_{ph}^4 - (v_S^2 + v_A^2) v_{ph}^2 + v_S^2 v_A^2 \cos^2\theta = 0 \ . \tag{6}$$

Equation Equation 6 has two roots in terms of the square of the phase speed, i.e.,

$$v_{ph}^2 = \frac{1}{2}\left(v_S^2 + v_A^2\right) + \frac{1}{2}\left(v_S^4 + v_A^4 - 2v_S^2 v_A^2 \cos 2\theta\right)^{1/2}, \tag{7a}$$

$$v_{ph}^2 = \frac{1}{2}\left(v_S^2 + v_A^2\right) - \frac{1}{2}\left(v_S^4 + v_A^4 - 2v_S^2 v_A^2 \cos 2\theta\right)^{1/2}. \tag{7b}$$

The solutions in Equation 7 correspond to two magneto-acoustic modes: the fast mode ($v_{fast} = |v_{ph}|$; Equation 7a) and the slow mode ($v_{slow} = |v_{ph}|$; Equation 7b). In summary, there are three MHD modes, the Alfvén mode Equation 5, whose restoring force is only magnetic tension, and the two magneto-acoustic modes whose restoring force is a combination of the magnetic tension and the total pressure Equation 3. The phase speed in Equation 6 depends on the angle, θ, and the ratio of the sound speed versus the Alfvén speed. This quantity is proportional to the plasma-β, which can be rewritten in the form of $\beta = (2/\gamma)v_S^2/v_A^2$. First let us explore the two extremes of the plasma-β, namely $\beta \gg 1$ and $\beta \ll 1$. Notice that $\beta \gg 1$ means that $v_S \gg v_A$, while $\beta \ll 1$ is equivalent to $v_A \gg v_S$. In the limit where $\beta \gg 1$, Equation 7 is reduced to,

$$v_{ph}^2 \sim \begin{cases} v_S^2 & \text{for } Equation\ 7a, \\ v_A^2 \cos^2\theta & \text{for } Equation\ 7b, \end{cases} \tag{8}$$

where the solution corresponding to Equation 7a is the dominant mode, while the solution to Equation 7b is a second order correction. As a result, for $\beta \gg 1$ the Alfvén and slow modes vanish and the fast mode, now the only mode, converges to the sound speed, v_S. This result is quite intuitive considering that a high plasma-β (i.e., $\beta \gg 1$) implies that the kinetic pressure dominates the magnetic field, thus the magnetic pressure and tension in Equation 2b can be neglected. This reduces Equation 2b to the linearised Navier-Stokes equation. For a low plasma-β scenario (i.e., $\beta \ll 1$), Equation 7 reduces to,

$$v_{ph}^2 \sim \begin{cases} v_A^2 & \text{for } Equation\ 7a, \\ v_S^2 \cos^2\theta & \text{for } Equation\ 7b, \end{cases} \tag{9}$$

which indicates that the fast magneto-acoustic wave converges in magnitude to the Alfvén speed and propagates isotropically.

Next, we consider $\boldsymbol{k} \parallel \boldsymbol{B}_0$ and $\boldsymbol{k} \perp \boldsymbol{B}_0$. The first case naturally corresponds the $\theta = 0$, and so Equation 7 is reduced to

$$v_{ph}^2 \sim \begin{cases} v_A^2 & \text{for } Equation\ 7a, \\ v_S^2 & \text{for } Equation\ 7b, \end{cases} \tag{10}$$

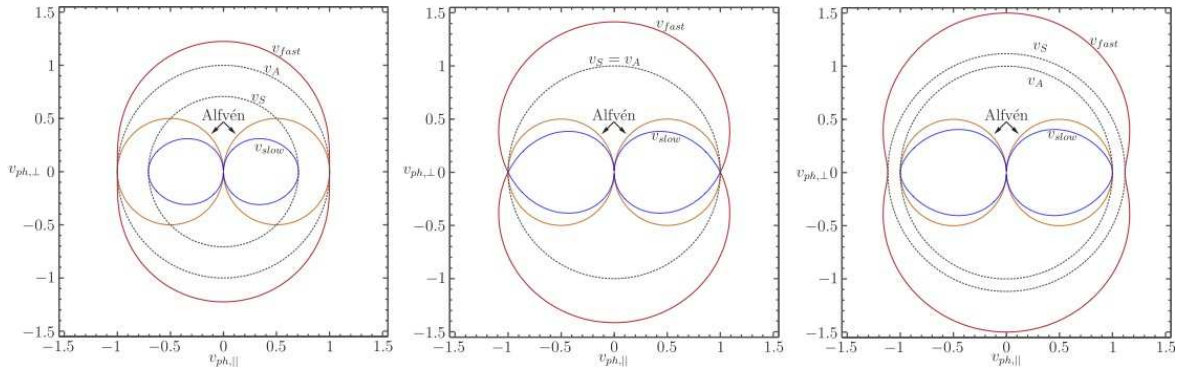

Fig. 4 Friedrichs diagrams for $v_S < v_A$ with $\beta = 1/\gamma$ (left), $v_S = v_A$ and $\beta = 2/\gamma$ (middle) and $v_S > v_A$ with $\beta = 2.5/\gamma$ (right). The phase speed perturbation of the slow magnetoacoustic wave is illustrated in blue, the Alfvén wave in orange and the fast magnetoacoustic wave in red. The dotted lines correspond to the sound and Alfvén speed. The horizontal and vertical axes labelled as $v_{ph,||}$ and $v_{ph,\perp}$ respectively represent the velocity perturbation components along and perpendicular to the equilibrium magnetic field, $\boldsymbol{B}_0$.

while for $\boldsymbol{k} \perp \boldsymbol{B}_0$ (i.e., $\theta = \pi/2$) Equation 7 reduces to,

$$v_{ph}^2 \sim \begin{cases} v_A^2 + v_S^2 & \text{for } Equation\ 7a, \\ 0 & \text{for } Equation\ 7b. \end{cases} \tag{11}$$

The first observation in this case is that the fast magneto-acoustic mode is no longer isotropic since its phase speed varies from v_A to $\sqrt{v_A^2 + v_S^2}$. Note that in the limit $v_A \gg v_S$, the phase speed of the fast mode becomes $\sim v_A$ which is in agreement with Equation 9. Under these conditions the fast mode can be considered to be approximately isotropic.

An important relation between the slow and fast magneto-acoustic modes is revealed if we combine Equation 1a, Equation 1c and Equation 1d to obtain the following relation between magnetic pressure and kinetic pressure,

$$\frac{1}{\mu_0} \boldsymbol{B}_0 \cdot \delta\boldsymbol{B} = \frac{v_A^2}{v_S^2} \left(1 - \frac{v_S^2}{v_{ph}^2} \cos^2 \theta \right) \delta p. \tag{12}$$

Therefore, according to Equation 12, when $v_{ph} < v_S \cos\theta$ the kinetic and magnetic pressures are out of phase by π and so these restoring forces oppose each other. From Equation 7b it follows immediately that this condition holds for the slow magneto-acoustic waves, and is clearly illustrated in Figure 4. In the case where $v_{ph} > v_S \cos\theta$, the magnetic and kinetic pressure perturbations are in phase with one another. This condition holds for the fast magneto-acoustic wave (see Equation 7a) depicted in Figure 4. For situations where $v_{ph} = v_S \cos\theta$, the magnetic pressure tends to zero, and apart from the trivial solution, this condition is satisfied when: (*i*) $v_A > v_S$ for $\theta = 0, \pi$ corresponding to the slow magneto-acoustic wave, (*ii*) $v_A = v_S$ and is satisfied by the the Alfvén wave, and lastly, (*iii*) $v_S > v_A$ which is satisfied by the fast magneto-acoustic wave at $\theta = 0, \pi$. Also notice that for $v_A \gg v_S$ the magnetic pressure is dominant, while for $v_S \gg v_A$ the plasma pressure dominates.

In summary, in linearised ideal MHD for a homogeneous plasma there are three distinct waves: the slow and fast magneto-acoustic and the Alfvén. The phase speeds of these waves are well ordered: $0 \leq v_{slow} \leq v_A \leq v_{fast}$, and also their velocities are mutually perpendicular, $\boldsymbol{v}_{slow} \perp \boldsymbol{v}_A \perp \boldsymbol{v}_{fast}$ (Goedbloed & Poedts 2004). The Alfvén mode is incompressible and is supported purely by the magnetic tension, while the restoring forces for the two magneto-acoustic modes is a combination of the total pressure and magnetic tension. In Table 2 we provide a brief summary of the results in this section. For $\beta \ll 1$, which is valid in magnetically dominated regions of the Sun's atmosphere, the fast mode is approximately isotropic while the slow and Alfvén modes exhibit strong anisotropies, with both components having *preferred* propagation directions along the magnetic field. It must be stressed that the Alfvén and slow modes do not propagate in directions perpendicular to the magnetic field.

3.3 Wave Modes in a Magnetic Flux Tube

To help us understand the much richer variety of MHD waves modes that can supported in more complex magnetic geometries, a useful first step is to consider a simple straight magnetic cylinder. Edwin & Roberts (1983) chose the particular case of a constant magnetic field inside, $B_i\hat{\boldsymbol{z}}$, and outside, $B_e\hat{\boldsymbol{z}}$, the flux tube with a discontinuity at the tube boundary $r = r_a$, where r_a is the tube radius. Similarly the equilibrium density and pressure inside and outside the tube

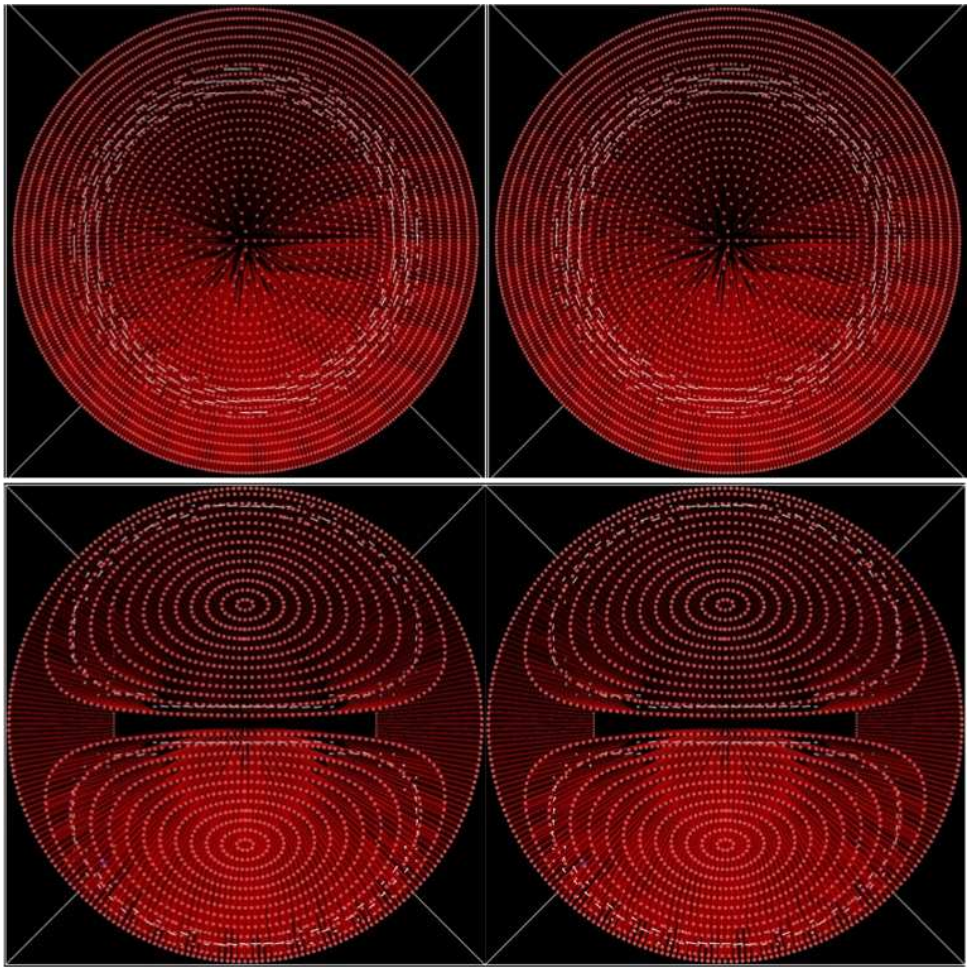

Fig. 5 *Upper panels:* The two extrema of the Alfvén mode for $n = 0$. This mode is also referred to as torsional Alfvén mode. In this figure (and in Figures 5–7), the red dotted ropes represent the magnetic field lines, while the white arrows describe the velocity field. *Lower panels:* The Alfvén mode for $n = 1$. Notice that the magnetic surfaces are decoupled, but that they are more intricately configured when compared with the torsional ($n = 0$) Alfvén mode displayed in the upper panels. The movie associated with this figure is available from *http://swat.group.shef.ac.uk/fluxtube.html*.

are taken to be ρ_i, p_i and ρ_e, p_e respectively. The resulting dispersion relations, assuming no energy propagation towards or away from the flux tube (thus we allow only $m_e^2 > 0$) are the following (Edwin & Roberts 1983),

$$m_i\rho_e(k_z^2v_{A_e}^2-\omega^2)\frac{K_n(m_er_a)}{K_n'(m_er_a)} = m_e\rho_i(k_z^2v_{A_i}^2-\omega^2)\frac{I_n(m_ir_a)}{I_n'(m_ir_a)}, \text{ for } m_i^2>0, \tag{13}$$

$$n_0\rho_e(k_z^2v_{A_e}^2-\omega^2)\frac{K_n(m_er_a)}{K_n'(m_er_a)} = m_e\rho_i(k_z^2v_{A_i}^2-\omega^2)\frac{J_n(n_0r_a)}{J_n'(n_0r_a)}, \text{ for } -m_i^2=n_0^2>0, \tag{14}$$

where,

$$m_i^2 = \frac{(k_z^2v_{s_i}^2-\omega^2)(k_z^2v_{A_i}^2-\omega^2)}{(v_{A_i}^2+v_{s_i}^2)(k_z^2v_{T_i}^2-\omega^2)}, \tag{15}$$

$$m_e^2 = \frac{(k_z^2v_{s_e}^2-\omega^2)(k_z^2v_{A_e}^2-\omega^2)}{(v_{A_e}^2+v_{s_e}^2)(k_z^2v_{T_e}^2-\omega^2)}, \tag{16}$$

are the internal and external radial wavenumbers, n is the azimuthal wavenumber and k_z is the longitudinal wavenumber which in the present work is along the $\hat{\boldsymbol{z}}$ direction. For the case where $m_i^2 > 0$ (see Equation 13), the amplitude of the resulting eigenmodes is heavily localised near the boundary of the flux tube and so these are referred to as surface modes. When $m_i^2 < 0$ the behaviour of the solutions inside the flux tube is oscillatory, and since only evanescent solutions are permitted outside the flux tube, the largest wave amplitudes are observed inside (and in the vicinity of) the flux tube.

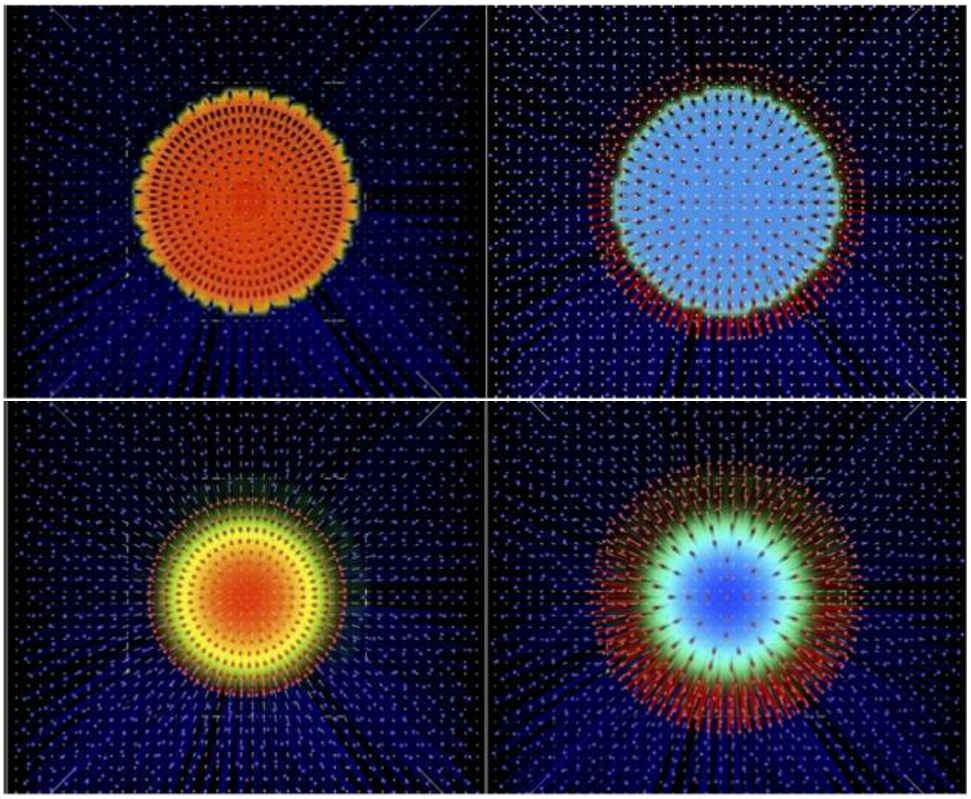

Fig. 6 The upper panels represent the slow sausage mode ($n = 0$), while the lower panels describe the fast sausage mode ($n = 0$). The density perturbation ($\delta\rho$) above the equilibrium background, ρ_i, is highlighted using warmer colours with red denoting the maximum perturbation. Conversely, density perturbations below the equilibrium are illustrated with cooler colours, with blue representing the minimum. The blue dotted ropes represent the magnetic field outside the flux tube. Notice that the dominant velocity component for the slow sausage mode is in the direction along the flux tube, while for the fast sausage mode ($n = 0$) this component is zero. The density perturbation and external magnetic field are represented in similar fashion in Figure 7. The movie associated with this figure is available from *http://swat.group.shef.ac.uk/fluxtube.html*.

These modes are referred to as body waves. The schematic diagram in Figure 1 depicts velocity and density perturbations characteristic to the fast and slow magnetoacoustic modes for $n = 0$ (sausage mode) and $n = 1$ (kink mode). Surface and body waves exhibit similar characteristics associated with the slow/fast magnetoacoustic and Alfvén modes. However, these modes have a substantially different behaviours when compared with the eigenmodes studied in § 3.2. The parallel component of the wavevector, $\boldsymbol{k}$, to the magnetic field, $\boldsymbol{B}_0$, is here defined as k_z. The azimuthal wavevector, n, and the radial wavevectors, m_i or m_e, form the perpendicular component to the magnetic field.

With that in mind, let us explore the similarities and differences of the corresponding eigenmodes in § 3.2 and the modes present in a magnetic flux tube. First notice that the Alfvén mode, shown in Figure 5, and the slow mode (see Figures 6 & 7), when present, exist even when the wavevector (in cylindrical coordinates in this case) is perpendicular to the magnetic field. This is not the case in § 3.2 (see Equation 11) for the slow mode considering $\boldsymbol{k}\cdot\boldsymbol{B}_0 = 0$ when $\boldsymbol{k} \perp \boldsymbol{v}_A$. Additionally, the fast magneto-acoustic mode in § 3.2 (for the case where $\beta \ll 1$) was approximately isotropic, while the fast mode in the magnetic cylinder is highly anisotropic and does not exist for some azimuthal wavenumbers. Also, the behaviour of radial harmonics for the fast mode is entirely different. For instance, for the fast sausage mode ($n = 0$) the main restoring force is the total pressure, while magnetic tension has only a minor role, while the fast kink mode ($n = 1$) appears to be nearly incompressible with the main restoring force being magnetic tension (e.g., see Figures 7 & 1). Nevertheless, despite the differences between the eigenmodes for the uniform medium and the magnetic flux tube, the velocities of the three modes present within a magnetic flux tube are still mutually perpendicular to one another. The practical implication of this is that the slow and Alfvén modes are incredibly difficult to detect in chromospheric flux tubes, while the fast magneto-acoustic mode is the most prominent. However, even for fast magneto-acoustic waves we have only successfully detected the sausage (azimuthal wavenumber $n = 0$) and kink ($n = 1$) modes, while modes with $n > 1$ are yet to be observed, mainly as a result of limitations in the spatial and temporal resolutions of the current generation of telescopes and instrumentation (Zhugzhda et al. 2000).

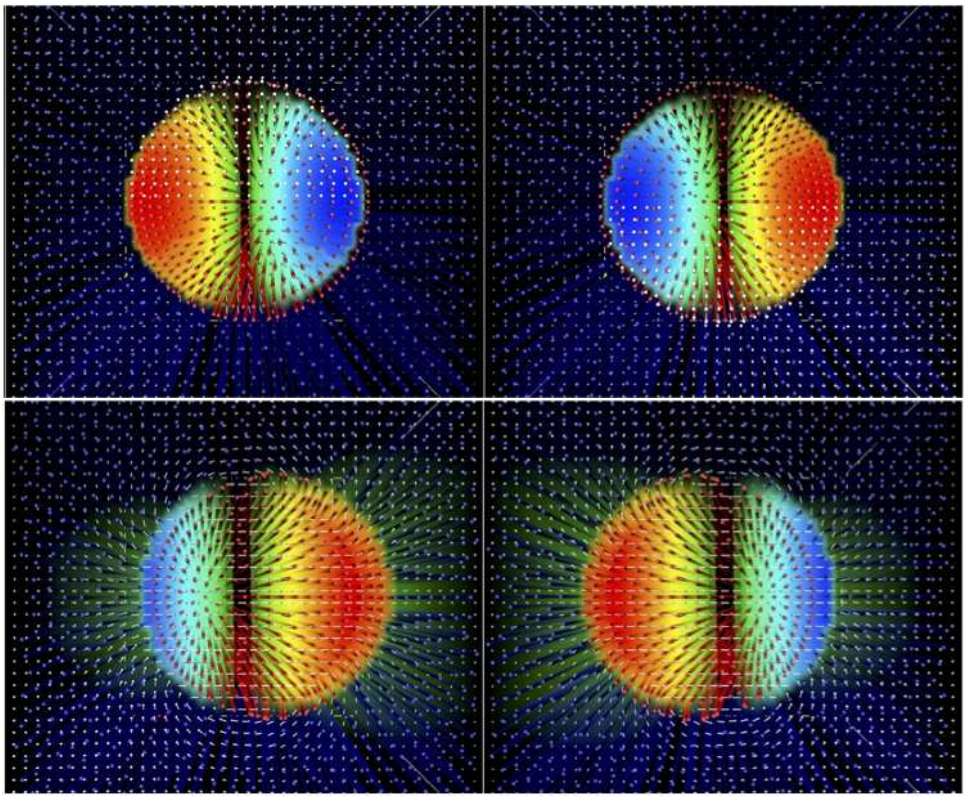

Fig. 7 *Upper panels:* The slow kink mode ($n = 1$). As with the slow sausage mode, the dominant component of the velocity field is along the direction of the magnetic field. *Lower panels:* The fast kink mode ($n = 1$). Note that the velocity component along the magnetic field for this mode is zero, as it is for the fast sausage mode in Figure 6. Another notable feature of this mode is that the divergence of the velocity inside the flux tube is zero, which suggests that this mode is (nearly) incompressible. The movie associated with this figure is available from *http://swat.group.shef.ac.uk/fluxtube.html*

In the following section we will discuss the overwhelming evidence that demonstrates the ubiquitous existence of compressible magneto-acoustic waves in the solar chromosphere. We will overview the observational characteristics which led to the various scientific interpretations, with a particular emphasis placed on the energetics of the detected waveforms. Importantly, we will show that such oscillatory motion can be readily generated and driven at the photospheric layers, with the resulting upwardly propagating waves acting as potentially important conduits for supplying continual energy to the upper regions of the solar atmosphere.

4 Compressible Waves

As mentioned in § 3.2, compressible waves are characterised by $\nabla \cdot \delta \boldsymbol{v} \neq 0$. Physically, this means that these waves have the ability to perturb the local plasma density. As a result, such perturbations give rise to periodic intensity fluctuations since the plasma emission is modulated by the induced compressions/rarefactions. The manifestation of such waves in the solar atmosphere has been well-documented since the 1960s when researchers first identified periodic fluctuations in both the intensity and velocity fields of solar optical observations (Leighton 1960; Leighton et al. 1962; Noyes & Leighton 1963). At first, these intensity and velocity oscillations were interpreted as purely acoustic waves. This was to be expected since acoustic wave based heating theories had already been proposed earlier by, e.g., Schwarzchild (1948) and Biermann (1948).

4.1 Magnetoacoustic Waves

From an MHD perspective, acoustically dominated magnetoacoustic wave modes should naturally occur in the Sun's atmosphere under all plasma-β regimes (see § 3.1 for the definition of plasma-β). One does not have to assume that waves of an acoustic character can only occur in regions that have little or no magnetic field. The important caveat to add is that in regions of strong magnetic field (i.e., low plasma-β), the acoustically dominated MHD wave modes are very anisotropic, with their direction of propagation significantly aligned to the magnetic field direction (see, e.g., the magnetoacoustic slow mode of a $\beta \ll 1$ homogeneous plasma in Table 2 and the left panel of Figure 4). In the following sections we review studies of these waves in different representative plasma-β regimes of the Sun's chromosphere, i.e., quiet Sun, network locations and active regions.

4.1.1 Quiet Sun and network locations

After intensity oscillations in the solar atmosphere were interpreted as the signatures of acoustically dominated waves, the next logical step was to attempt to track these wave motions higher up in the solar atmosphere. Initial work by Deubner (1971) was able to follow velocity and intensity fluctuations through to the upper-photospheric layers by employing narrowband Na I D_1 and Mg I b_2 filters. Then, utilising the vacuum tower telescope (now the Dunn Solar Telescope) at the National Solar Observatory, New Mexico, alongside dedicated chromospheric Hα measurements, Deubner (1974, 1975) was able to detect propagating waves down to spatial scales on the order of a few arcseconds. However, these measurements were designed to shed light on the geometrical formation heights of the spectral lines used in the study, and therefore made no estimation of the energetics carried by these waves. Subsequent work revealed that the upward phase velocity of the waves was too large to be explained by traditional acoustic phenomenon, and instead the embedded magnetic field must also be considered to better understand the wave energies and dynamics (Osterbrock 1961; Mein & Mein 1976; Ulmschneider 1976). Many publications followed which addressed the energetics of upwardly propagating magnetoacoustic waves (Athay & White 1978, 1979a,b; White & Athay 1979a,b; Lites & Chipman 1979; Mein & Mein 1980; Schmieder & Mein 1980), but none were able to find sufficient mechanical flux to balance the heavy radiative losses experienced in the solar chromosphere. Of course, the main purpose of this review article is not to provide an in-depth overview of historical results, but instead review recent advances in the field of propagating wave phenomena. Therefore, for a more detailed overview of the initial pioneering work undertaken in relation to wave studies in the lower solar atmosphere, we refer the reader to a series of early review articles by Frisch (1972), Bonnet (1981) and Narain & Ulmschneider (1990, 1996), and of course, the references contained therein.

In more recent times, and following the analysis of Transition Region and Coronal Explorer (TRACE; Handy et al. 1999) data, Fossum & Carlsson (2005a, 2006) were unable to detect sufficient power in high-frequency (5–50 mHz; 20–200 s) magnetoacoustic oscillations and concluded that these waves cannot constitute the dominant heating mechanism of the solar chromosphere. However, this study was limited by the cadence TRACE can achieve ($\sim$ 13 s), its coarse spatial sampling ($\approx 0\farcs5$ pixel^{-1}) and the onboard filter transmissions (Fossum & Carlsson 2005b). Consequently, physically small oscillation sites with short coherence lengths may be smeared out by the coarse spatial and temporal resolutions. Furthermore, it was suggested by Jefferies et al. (2006) and Wedemeyer-Böhm et al. (2007) that such methods will overlook dynamic patterns created on sub-resolution scales, and as a direct result severely underestimates the actual mechanical flux (Kalkofen 2007, 2008). In a follow-up article, Cuntz et al. (2007) employed similar UV TRACE observations alongside revised 1D simulations, detailed by Rammacher & Ulmschneider (2003), to reveal that the complex small-scale time-dependent topologies that manifest within the solar chromosphere produce a network of hot filaments embedded into broad cool regions. The authors suggest that the hot chromospheric components of solar emission consist of small pockets embedded in much cooler material that is unrelated to the Ca II emission previously used as a temperature diagnostic. As a result, the limited spatial resolution of the TRACE instrument makes a

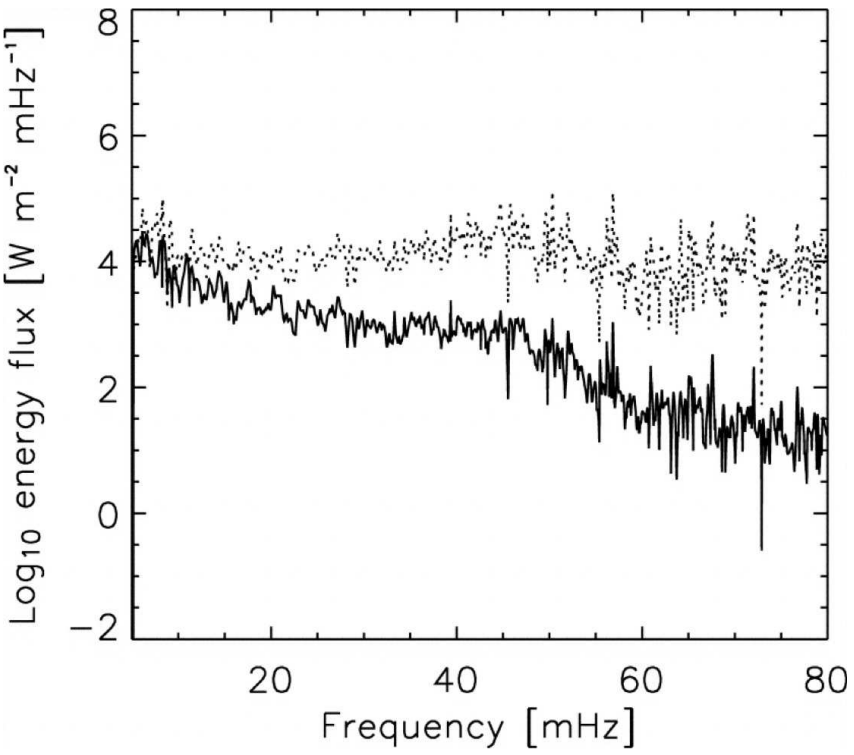

Fig. 8 Observed acoustic energy flux available for chromospheric heating (solid line) and the corresponding acoustic energy flux 86 km below at the $\tau_{500} = 1$ layer (dotted line). Since the radiative damping in the solar photosphere increases with frequency, the flattening of the acoustic spectrum at higher heights is believed to correspond to an increase in the overall high-frequency photospheric acoustic power. However, here the behaviour above 30 mHz ($\lesssim$ 30 s) is critically dependent on the subtraction of inherent noise characteristics, as well as the instrumental temporal and spatial resolutions. It has subsequently been shown that the TRACE instrument may not have sufficient spatial *and* temporal resolutions to accurately define and characterise the acoustic power available for chromospheric heating. Image adapted from Fossum & Carlsson (2006).

direct comparison between the measured radiative fluxes and the implied wave energy fluxes difficult, if not impossible using purely 1D simulations. Employing higher resolution observations from the Göttingen spectrometer/polarimeter (Puschmann et al. 2006; Bello González & Kneer 2008), Bello González et al. (2009, 2010a) were able to find significant energy flux ($\sim$ 2000 W m^{-2}) for magnetoacoustic periodicities as low as 40 s at lower chromospheric heights. Then, utilising the Imaging Magnetograph eXperiment (IMaX; Martínez Pillet et al. 2011) two-dimensional spectropolarimeter onboard the Sunrise balloon-based observatory (Solanki et al. 2010; Barthol et al. 2011), Bello González et al. (2010b) uncovered yet more evidence to support the hypothesis that the lower chromosphere is bombarded with high-energy magnetoacoustic waves with energies on the order of $6400 - 7700$ W m^{-2}. The work of Bello González et al. (2009, 2010a,b) strengthened the support for atmospheric heating through magnetoacoustic wave dissipation, and coupled with the opposing findings of Fossum & Carlsson (2005a, 2006, Figure 8) inspired many groups to push the examination of magnetoacoustic waves to even smaller spatial extents, especially with kG strength magnetic bright points (MBPs; Dunn & Zirker 1973; Stenflo 1985; Solanki 1993; Sanchez Almeida & Martinez Pillet 1994; Berger & Title 2001; Steiner et al. 2001; Crockett et al. 2009, 2010; Jess et al. 2010b; Keys et al. 2011b, 2013; Utz et al. 2013) offering potentially efficient waveguides on sub-arcsecond scales.

McAteer et al. (2002) studied MBPs in network locations with high resolution ground-based observations and found a multitude of magnetoacoustic wave power spanning the deep photosphere through to the upper chromosphere. Follow-up work incorporating phase analysis routines allowed the authors to characterise the waves as upwardly propagating, with their magnetoacoustic nature potentially offering a means for energy deposition on small spatial scales (McAteer et al. 2003). Kontogiannis et al. (2010) employed period-mapping techniques to investigate the linkage between small-scale concentrated photospheric magnetic flux elements to oscillations found in simultaneous chromospheric Hα time series (Figure 9). The authors uncovered a complex relationship depending on both the strength and orientation of the encompassing magnetic fields, but ultimately found evidence for waves tracing the path of small-scale magnetic fields through to chromospheric heights, indicative of acoustically dominated waves in a low plasma-β regime. Using detailed cross-correlation methods on Solar Optical Telescope (SOT; Tsuneta et al. 2008a; Suematsu et al. 2008) data

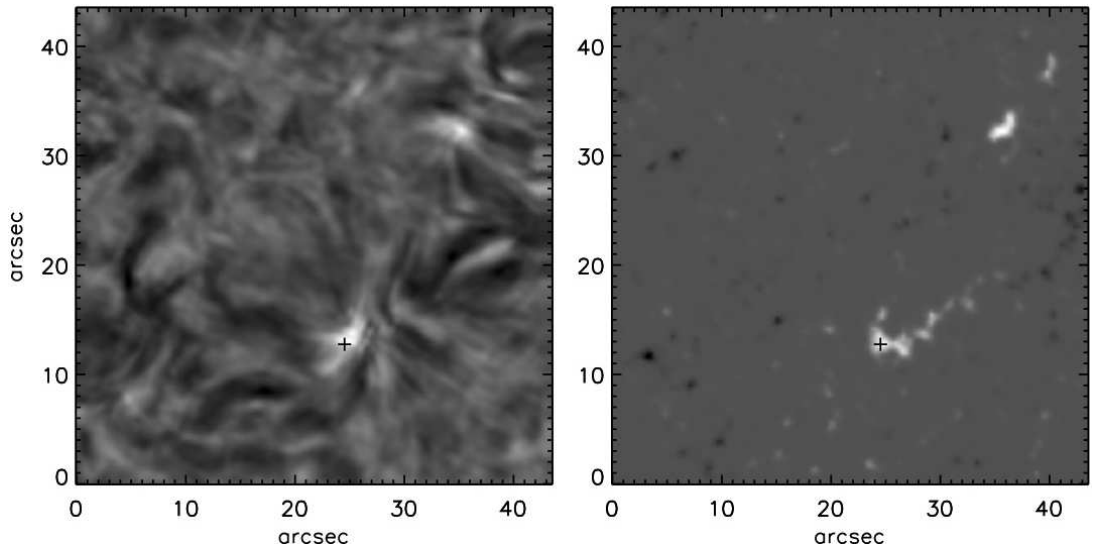

Fig. 9 A chromospheric Hα core image (left) and co-spatial line-of-sight magnetogram (right). The black cross indicates the location of concentrated magnetic fields in the solar photosphere, with field strengths exceeding 1000 G, which can connect upwards through various layers of the solar atmosphere, thus providing an efficient channel for the propagation of compressible waves. Image adapted from Kontogiannis et al. (2010).

from the Hinode spacecraft (Kosugi et al. 2007), Lawrence & Cadavid (2012) demonstrated a direct linkage between upwardly propagating magnetoacoustic modes and aureoles of enhanced oscillatory power at chromospheric heights, suggesting how powerful photospheric motions at periodicities nearing the acoustic cut-off may be able to produce shock-wave heating of the localised chromospheric plasma (Carlsson & Stein 1992; Theurer et al. 1997; Krijger et al. 2001; Bloomfield et al. 2004; Vecchio et al. 2009). However, most shock phenomena arises at the interface with downflowing material in the mid-chromosphere, and as a consequence little of the resulting heat and motion can be found within the upper regions of the solar chromosphere (Carlsson & Stein 1997). While shock waves may not be a dominant heating mechanism for the magnetised solar chromosphere, current research is investigating their possible role in the generation of incompressible wave modes at higher atmospheric heights (e.g., De Pontieu et al. 2004; Rouppe van der Voort et al. 2007; Cauzzi et al. 2008; Rutten et al. 2008; Kuridze et al. 2013).

In a series of papers, Beck et al. (2009, 2012, 2013a,b) employed sub-arcsecond resolution observations from the POlarimetric LIttrow Spectrograph (POLIS; Beck et al. 2005) on the Vacuum Tower Telescope, Tenerife, to analyse and track the velocity and intensity perturbations of small-scale magnetic elements reaching chromospheric heights. The authors found that, even for small-scale magnetic elements, the embodied magnetoacoustic energy was simply insufficient to maintain the chromospheric temperature rise by a factor of about five. However, Liu et al. (2014b) have recently shown that many structures (including omnipresent spicules, mottles and fibrils) in the lower solar atmosphere demonstrate signatures of the superposition of both upwardly and downwardly propagating magnetoacoustic wave modes, indicating that while the upwardly propagating signatures dominate, the mere presence of downwardly propagating waves may artificially reduce the derived magnetoacoustic energy flux (Figure 10).

Over the last 50 years there has been an abundance of studies attempting to quantify the role magnetoacoustic waves play in the heating of the outer solar atmosphere. As time progressed and new high resolution facilities became commissioned (TRACE, Hinode/SOT, etc.), researchers attempted to probe the energetics of magnetoacoustic waves further still by harnessing the improved spatial and/or temporal resolutions on offer. However, each time (Fossum & Carlsson 2005a, 2006; Beck et al. 2009; Bello González et al. 2009, 2010a,b; Beck et al. 2012, 2013a,b) the authors were unable to conclusively verify that these wave modes carry sufficient energy to play a dominant role in atmospheric heating. Perhaps, as highlighted by the work of Jefferies et al. (2006), Wedemeyer-Böhm et al. (2007), Kalkofen (2007, 2008), to name but a few, we still require yet higher spatial and temporal resolutions to be able to accurately constrain the rapid fluctuating dynamics synonymous with propagating magnetoacoustic wave modes in small-scale magnetic elements. With the upcoming National Large Solar Telescope (NLST; Hasan et al. 2010), Daniel K. Inouye Solar Telescope (DKIST, formerly the Advanced Technology Solar Telescope, ATST; Keil et al. 2003; Rimmele et al. 2010), Solar Orbiter (Müller et al. 2013), Solar–C (Shimizu et al. 2011) and European Solar Telescope (EST; Collados et al. 2010) facilities all offering unprecedented views of the Sun, it is only a matter of time until we are able to accurately quantify the contribution of magnetoacoustic waves to plasma heating.

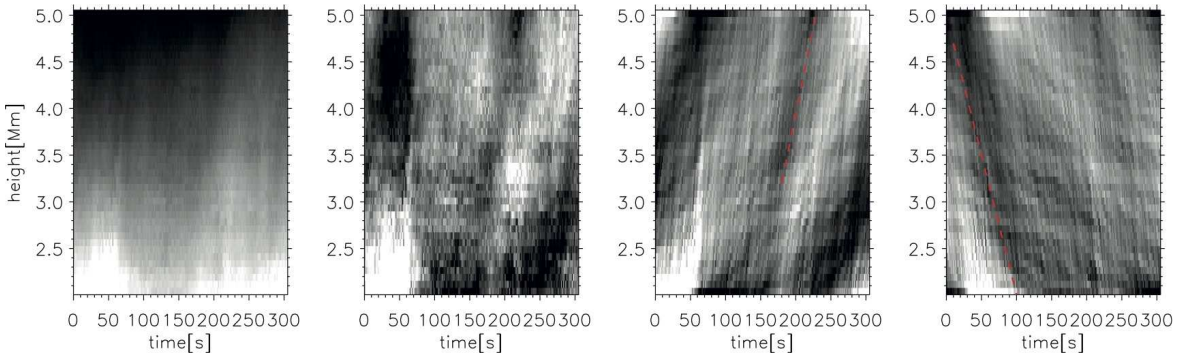

Fig. 10 Time–distance intensity maps of off-limb spicules, from left to right, of original Hinode/SOT Ca II H data, background-subtracted data, and those filtered for upwardly and downwardly propagating magnetoacoustic modes, respectively. Here, the 'height' measurement is indicative of the atmospheric height above the solar photosphere, and therefore represents magnetoacoustic wave modes reaching chromospheric heights. The presence of both upwardly and downwardly propagating waves (as indicated by the dashed red lines orientated in different directions) suggests the superposition of such phenomena may cause previous evaluations of magnetoacoustic energy flux to be underestimated. Image adapted from Liu et al. (2014b).

4.1.2 Active regions

Active regions are typically large-scale structures extending throughout the solar atmosphere and visible as an intense manifestation of magnetic fields. Sunspots, pores and plage are the usual constituent representation of the magnetic field topology in the solar chromosphere, with overall sizes in the range of 30–10 000 million square km (10–3000 micro solar hemispheres; Kopecký & Mayer 1953; Howard 1992; Martinez Pillet et al. 1993; Baumann & Solanki 2005) and field strengths regularly exceeding 1000 G at the photospheric level, with over 6000 G documented in extreme cases (Livingston et al. 2006). Thus, solar active regions provide idealised conduits for wave and energy transportation into the outer solar atmosphere. Indeed, a wide variety of wave phenomena has been observed in active region structures for over 40 years (Beckers & Tallant 1969; Bogdan & Judge 2006). Initial work on oscillatory phenomena in sunspots helped validate the detection of long-period magnetoacoustic oscillations, which are generated by the response of the convectively-inhibiting sunspot to the 5-minute global p-mode oscillations (Thomas et al. 1982; Lites 1992). While oscillations in solar active regions are dominated by periodicities intrinsically linked to the global p-mode spectrum (on the order of 3–5 minutes; Goldreich & Keeley 1977a,b; Gabriel 1992; Baudin et al. 1996; Lazrek et al. 1997, and the references therein), an extended range of alternative wave periods can also be identified in the active region locality, spanning three orders-of-magnitude from in-excess of one hour (Demchenko et al. 1985) through to less than several seconds (Jess et al. 2007).

Running penumbral waves (RPWs) are a common sight in the chromospheric layer of sunspots (Nye & Thomas 1974). Giovanelli (1972) and Zirin & Stein (1972) provided the first observational evidence of this phenomenon when they detected concentric wave fronts propagating outwards through the penumbra of the sunspot in narrowband Hα images (Figure 11). Interpreted as magnetoacoustic modes, Brisken & Zirin (1997) and Kobanov & Makarchik (2004) demonstrated how the wave signatures are actually comprised of the superposition of many individual wave periods, each propagating with independent phase speeds. Kobanov et al. (2006) examined the relationship between propagating intensity and velocity disturbances to conclude that the frequencies and phase speeds of RPWs are largest (> 3 mHz or $<$ 300 s, 40 km s^{-1}) at the inner penumbral boundary, decreasing to their lowest values (< 1 mHz or > 1000 s, 10 km s^{-1}) at the outer penumbral edge. Additionally, Kobanov (2000) has shown evidence that the RPWs can propagate to distances exceeding $\sim 15''$ ($\sim 10\,000$ km) from the outer edge of the penumbral boundary, suggesting the waves have considerable energy to overpower the signatures of ubiquitous quiet-Sun p-mode oscillations. However, while RPWs are readily observed in chromospheric imaging and spectroscopic sequences, their origin has been under intense debate ever since their discovery. Some consider RPWs to be a purely chromospheric phenomenon driven by trans-sunspot waves, while others believe they are the observational signature of upwardly propagating magnetoacoustic waves guided along the intense magnetic fields of the underlying sunspot (Christopoulou et al. 2000, 2001; Georgakilas et al. 2000; Centeno et al. 2006; Tziotziou et al. 2006, 2007). The recent work of Bloomfield et al. (2007) has added momentum to the interpretation that RPWs are a chromospheric visualisation of upwardly propagating magnetoacoustic oscillations through use of high-resolution spectroscopic measurements, obtained with the Tenerife Infrared Polarimeter (TIP; Martínez Pillet et al. 1999) attached to the German Vacuum Tower Telescope in Tenerife, Canary Islands. Here, the authors suggested that RPWs can readily propagate along magnetic field lines in a low plasma-β regime (i.e., dominated by magnetic pressure) environment, and therefore most likely explained as a signature of the channelling of magnetoacoustic waves through to chromospheric heights. Indeed, in the lower solar atmosphere the strong magnetic field strengths associated with sunspot

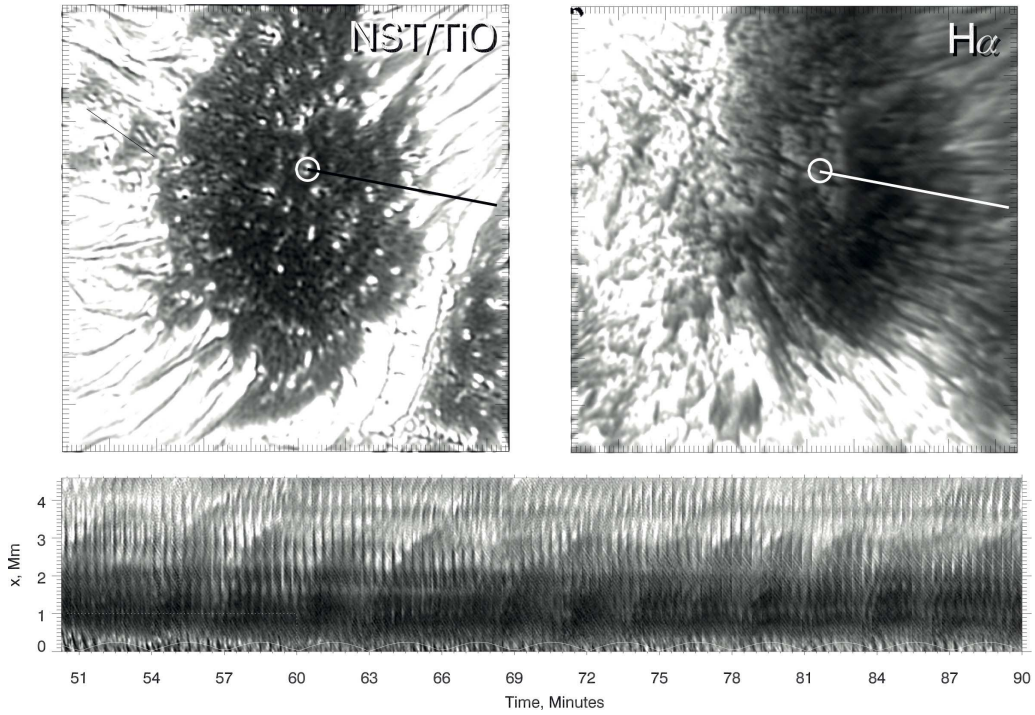

Fig. 11 A photospheric TiO image (upper left) and a simultaneous and co-spatial Hα core snapshot (upper right) of a sunspot acquired by the high-resolution NST. Both images have been unsharp masked to better reveal fine-scale details, while the long tick marks on the axes represent 1000 km intervals. The black and white lines indicate the location of the time–distance cut displayed in the lower panel, while the large white circles highlight the position of a photospheric umbral dot that forms the starting point of the time–distance cut. The propagation of RPWs is clearly evidenced by the diagonal trends present in the time–distance diagram, where curved features either represent the acceleration of wave activity or the superposition of differing wave periodicities along the observational line-of-sight. The white curve at the bottom of the lower panel displays a constant 3 minute periodicity to highlight the repetitive and ubiquitous nature of all RPW phenomena. Images adapted from Yurchyshyn et al. (2014).

structures (up to ~ 6000 G; Livingston et al. 2006) results in extremely large magnetic pressures when compared to the localised gas pressure (i.e., plasma-$\beta \ll 1$; Mathew et al. 2004). Under these conditions MHD wave modes can exist that have field-aligned perturbations which are much larger than the cross-field perturbations. These compressive and acoustically dominated MHD wave modes are strongly guided by the magnetic field and hence are very anisotropic, thus producing stable waveguides for oscillations to propagate along (Roberts & Webb 1978; Nakariakov & Roberts 1995; Erdélyi & Hargreaves 2008; Hindman & Jain 2008; Luna-Cardozo et al. 2012; Williamson & Erdélyi 2014). While Bloomfield et al. (2007) provided tentative evidence that RPWs are in-fact upwardly propagating magnetoacoustic waves, their evidence relied on single-slit spectroscopic measurements with a spatial resolution of $0\farcs8$. As a result, all locations within the vicinity of the sunspot were not examined with a high degree of precision, and the conclusive proof as to the origin of RPWs remained elusive.

Pushing the boundaries yet further by employing high-resolution images obtained with the Rapid Oscillations in the Solar Atmosphere (ROSA; Jess et al. 2010c) and Hydrogen-Alpha Rapid Dynamics camera (HARDcam; Jess et al. 2012a) instruments on the Dunn Solar Telescope, Jess et al. (2013) compared the dynamics of RPWs with magnetic field extrapolations obtained with the Helioseismic and Magnetic Imager (HMI; Schou et al. 2012) onboard the Solar Dynamics Observatory (SDO; Pesnell et al. 2012). The authors found that the composition of both the observed frequencies and the spatial locations at which they were present conclusively agreed with the predicted cut-off frequencies imposed by the geometry of the magnetic fields at chromospheric heights, something which was initially proposed by Reznikova et al. (2012) who used lower resolution UV data from the Atmospheric Imaging Assembly (AIA; Lemen et al. 2012) onboard SDO. Furthermore, Jess et al. (2013) were able to determine the phase speeds of the propagating magnetoacoustic RPWs as a function of their oscillatory period by decomposing the original time series into narrow frequency bands through implementation of 3–dimensional Fourier filtering techniques (Figure 12). The authors were able to corroborate the results of Kobanov et al. (2006), but place more stringent thresholds on the periodicities and phase speeds of the RPWs as a direct result of the high temporal and spatial resolutions offered by the ROSA and HARDcam instruments. Consequently, the linkage between the photospheric p-mode spectrum, the geometry changes of the magnetic field lines with atmospheric height, and the resulting wave signatures visible in simultaneous chromospheric

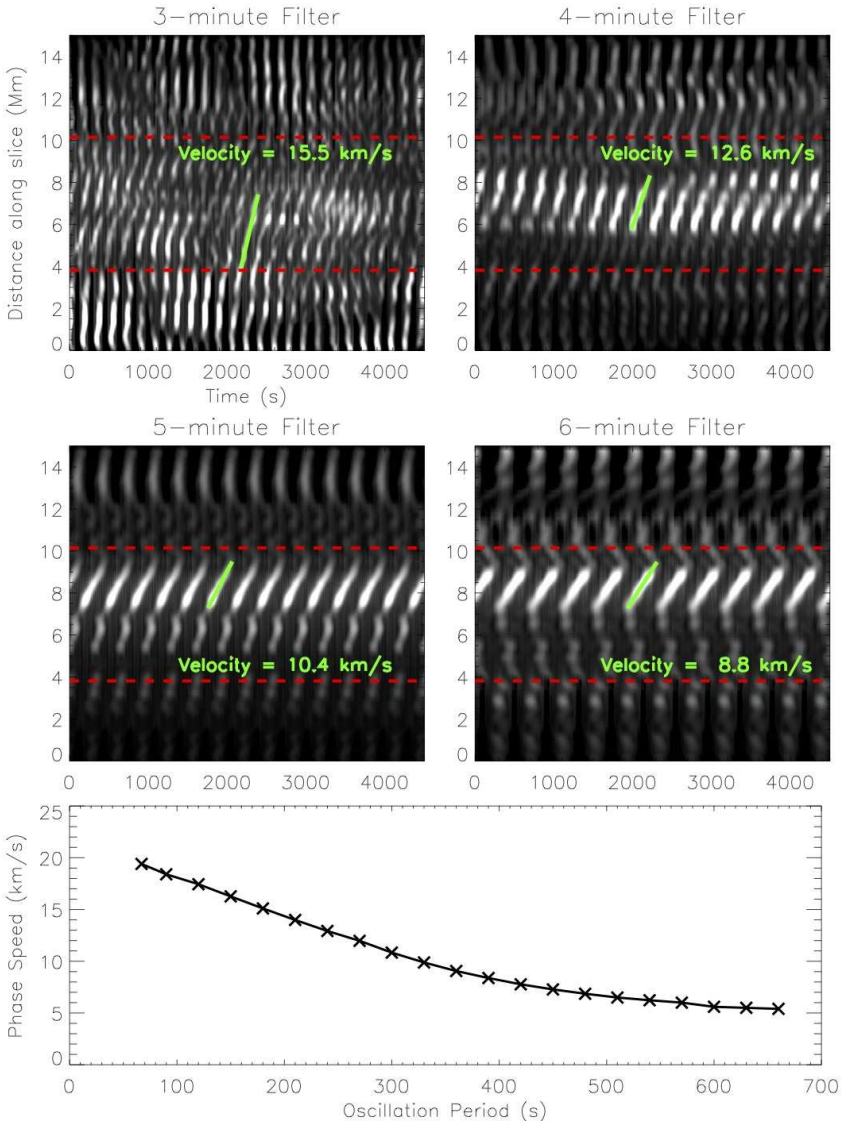

Fig. 12 Time–distance diagrams of chromospheric sunspot data (upper and middle panels), where 0 Mm indicates the centre of the underlying umbra. Each time–distance slice was extracted using identical solar coordinates, but with Fourier filtering techniques previously employed to isolate particular periodicities corresponding to 3 (upper-left), 4 (upper-right), 5 (middle-left), and 6 (middle-right) minutes. Red horizontal dashed lines highlight the inner- and outer-penumbral boundaries at ≈ 3.8 and ≈ 10.1 Mm, respectively, from the centre of the umbra. Solid green lines indicate the lines-of-best-fit used to calculate the gradient in each of the time–distance diagrams, and thus represents a measure of the period-dependent phase speeds. The lower panel displays the RPW phase speed (in $\mathrm{km\,s^{-1}}$) as a function of oscillatory period. Image reproduced from Jess et al. (2013).

observations directly supports the interpretation that RPW phenomena are the chromospheric signature of upwardly-propagating magnetoacoustic waves generated in the photosphere. This has since been further substantiated by Yuan et al. (2014b), who utilised chromospheric UV AIA images to reveal how the distribution of oscillatory power varied in the vicinity of a sunspot as a function of spatial location, and further suggested how such wave characteristics may reflect on the localised magnetic and thermal composition. However, while it has been demonstrated through multiwavelength chromospheric observations that upwardly propagating magnetoacoustic oscillations are rife within sunspot penumbrae, the energetics associated with these waves are negligible with regards to the overall radiative losses experienced in chromospheric active regions (Nye & Thomas 1976; Galloway 1978).

Oscillations manifesting in the near-vertical magnetic field configurations of sunspot umbrae have recently began to attract the attention of the solar physics community again. Magnetic fan and plume structures are commonly observed to extend outwards from sunspots into the solar corona, often with lengths exceeding many hundreds of Mm (Curdt et al. 2008; Krishna Prasad et al. 2012b; Raouafi & Stenborg 2014). One of the first studies which uncovered propagating

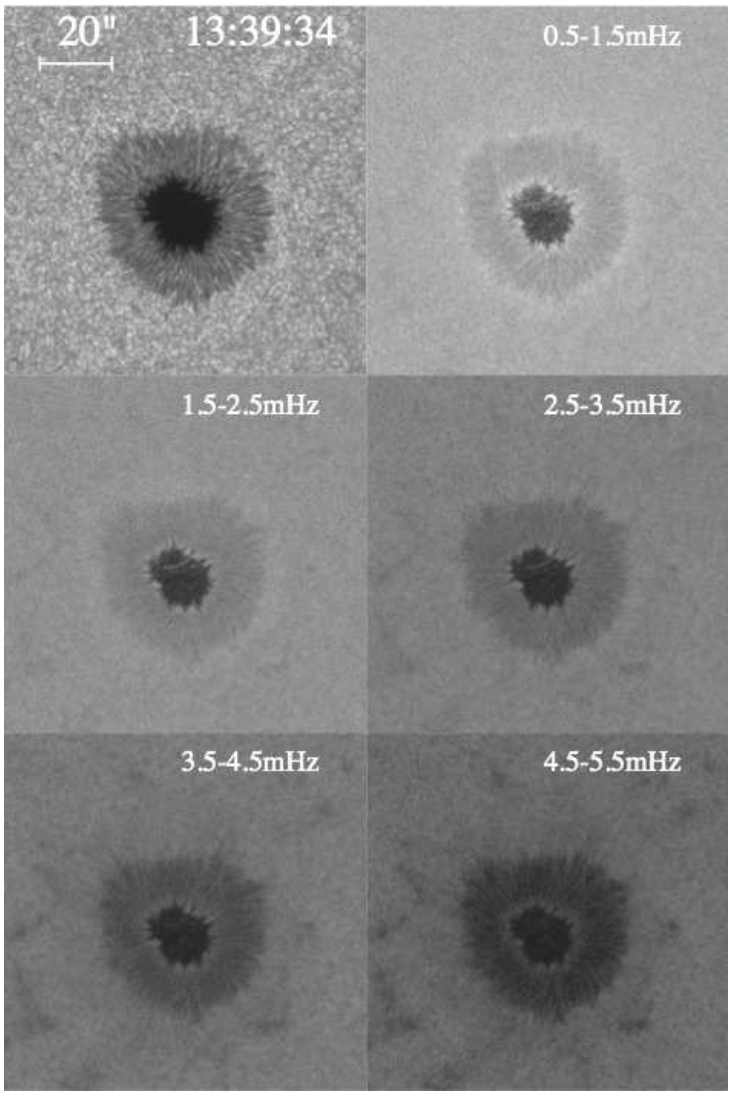

Fig. 13 A photospheric G-band image (upper-left) of an active region observed by the SOT instrument onboard Hinode on 2007 January 8. The remaining panels depict the spatial mapping of Fourier power of magnetoacoustic oscillations in narrow frequency bins corresponding to 0.5–1.5 mHz (667–2000 s), 1.5–2.5 mHz (400–667 s), 2.5–3.5 mHz (285–400 s), 3.5–4.5 mHz (222–285 s) and 4.5–5.5 mHz (180–222 s). It is clear that highly magnetic locations surpress magnetoacoustic power over all frequency ranges. Image reproduced from Nagashima et al. (2007).

wave phenomena in such coronal structures was by Deforest & Gurman (1998), who used the Extreme-ultraviolet Imaging Telescope (EIT; Delaboudinière et al. 1995) onboard the Solar and Heliospheric Observatory (SoHO; Domingo et al. 1995) to identify quasi-periodic perturbations in the brightness of EUV image sequences. More recent studies, incorporating higher resolution telescopes such as TRACE, interpreted these oscillations as the signatures of upwardly propagating magnetoacoustic waves with velocities in the range of 70–165 km s^{-1} and periodicities of 180–420 s (Ofman et al. 1999; Ofman & Wang 2002; De Moortel & Hood 2003, 2004; Mendoza-Briceño et al. 2004; Krishna Prasad et al. 2011, 2012a; Kobanov & Chelpanov 2014; Liu & Ofman 2014). However, while the coronal characteristics of magnetic fan and plume oscillations were well documented, the origin of these waves remained elusive. De Moortel et al. (2002) suggested that the most likely explanation would be a photospheric driver directly exciting the magnetic footpoints of the fan and plume structures. This scenario requires the magnetoacoustic wave trains to be able to propagate from the photosphere, through the chromosphere and transition region, and into the corona. Khomenko & Collados (2006) produced numerical simulations of the lower solar atmosphere and revealed how ~ 3 minute magnetoacoustic oscillations generated at the base of a sunspot umbra can readily propagate upwards through the lower layers and into the transition region. Thus, a key science goal was now not only to detect these waves, but to track them through the chromosphere to coronal heights. However, three minute umbral oscillations are notoriously difficult to detect at

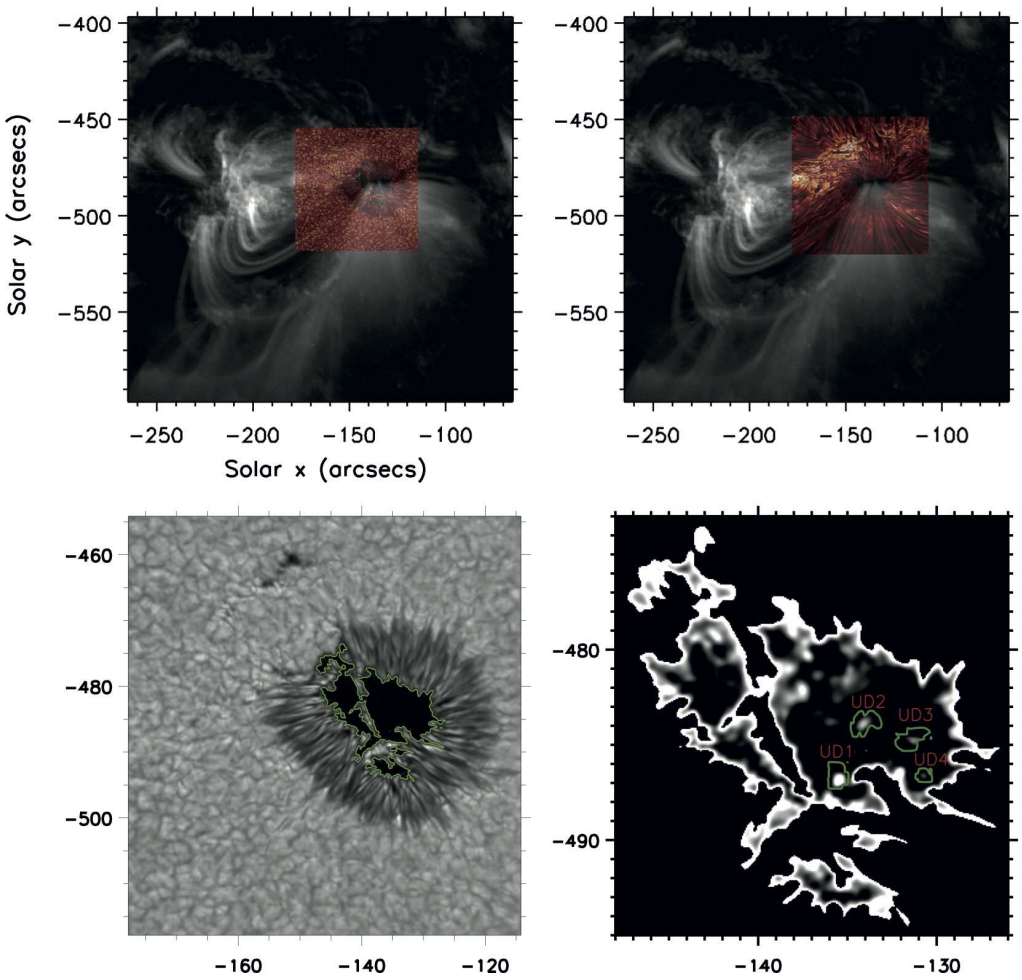

Fig. 14 The top panels display coronal EUV (171 Å) images taken by the AIA instrument onboard SDO on 2011 July 13 and interlaced with co-spatial and co-temporal ROSA 4170 Å continuum (upper left) and Hα (upper right) snapshots. It is clear the high degree of co-alignment precision now possible between multiwavelength *and* multi-instrument image sequences. The lower left panel shows the full ROSA 4170 Å continuum field-of-view, where solid green contours highlight the perimeter of the sunspot umbra. The lower right panel displays a magnification of the umbra itself, and reveals a number of small-scale intensity enhancements within the dark umbral background. Such umbral dots, labelled UD1, UD2, UD3 and UD4, display 3 minute oscillatory power several orders-of-magnitude higher than in the surrounding sunspot umbra (green contours) and are believed to be the locations where the intense coronal fans, each displaying prominent slow magnetoacoustic wave phenomena, are anchored. Images adapted from Jess et al. (2012a).

photospheric heights. Both Lites & Thomas (1985) and Balthasar et al. (1987) were unable to detect photospheric signatures of 3 minute umbral oscillations, claiming they may be swamped by noise due to their very low amplitudes. Employing the higher sensitivity SOT instrument onboard Hinode, Nagashima et al. (2007) revealed how all oscillatory power within sunspot umbrae is drastically reduced (Figure 13); a common phenomenon now referred to as 'acoustic power suppression' (Woods & Cram 1981; Thomas et al. 1982; Title et al. 1992; Parchevsky & Kosovichev 2007; Chou et al. 2009; Ilonidis & Zhao 2011; Couvidat 2013). Even more recently, Kobanov et al. (2008, 2011a,b) were not only able to detect photospheric 3 minute oscillations, but the authors tentatively claimed that the locations of minimum photospheric power also corresponded to heightened power in co-spatial chromospheric observations. Unfortunately the spatial resolution obtained by the Horizontal Solar Telescope (Kobanov et al. 2009) at the Sayan Solar Observatory, Russia, was on the order of $1''$, thus preventing precise characterisation of the exact umbral structures displaying the 3 minute periodicities.

Undertaking a multiwavelength study spanning the near infrared through to the EUV, Jess et al. (2012a) were able to provide evidence that small-scale photospheric umbral dots directly contribute to the presence of propagating magnetoacoustic waves observed in coronal fan structures. First, it was noted that umbral dots, visible as concentrated brightenings in the sunspot umbra with diameters $\sim 0\farcs5$, displayed 3 minute oscillatory power several orders of magnitude higher than the surrounding umbral locations. Regions of heightened and localised power were also co-spatial in simultane-

ous chromospheric Hα and Ca II image sequences. Employing spectral imaging techniques with the Interferometric BIdimensional Spectrometer (IBIS; Cavallini 2006), Jess et al. (2012a) were able to compare the phase relationship between intensity and line-of-sight velocity measurements to categorise the wave signatures as upwardly propagating slow magnetoacoustic modes. Then, by interlacing co-temporal EUV images from the AIA instrument onboard SDO with the chromospheric observations, it was found that the footpoints of the coronal fans lay directly on top of the umbral dot structures displaying heightened oscillatory power (Figure 14). Almost unbelievably, it appears that photospheric structures with diameters $\sim 0\farcs5$ (360 km) can drive propagating magnetoacoustic oscillations in coronal structures not only several thousand km above their position, but on structures which have expanded into the local plasma to diameters often exceeding $10''$ (7000 km). Estimations of the energy carried by such propagating disturbances has been performed by Deforest & Gurman (1998) and De Moortel et al. (2000), producing an incredible span of values in the range of 0.1–100 W m^{-2}, thus opening up possibilities for such magnetoacoustic waves to contribute significantly to the heating of the lower corona through compressive dissipation. Recent work by Kiddie et al. (2012) and Uritsky et al. (2013) have verified the temperature-dependent nature of the propagation speeds of disturbances in fan/plume structures, suggesting the magnetic field topology from the photosphere upwards may play an important role in the observed dynamics; similar to the frequency filtering observed in RPW phenomena (Reznikova et al. 2012; Jess et al. 2013; Yuan et al. 2014b). However, in contrast to coronal fan and plume structures observed directly above sunspots, those positioned within active regions, yet in non-sunspot locations, appear to display vastly different characteristics. Often the non-sunspot structures display wave periodicities longer than 10 minutes (Berghmans & Clette 1999; Marsh et al. 2009; Wang et al. 2009), and as a result cannot be interpreted in terms of upwardly propagating p-mode oscillations (Wang et al. 2013). Another outstanding issue is how such low frequency waves actually penetrate into the corona since acoustic-based cutoff theories cannot explain this. Subsequently, it has been suggested that small-scale nanoflare activity in the solar chromosphere may be able to trigger such low-frequency wave phenomena (Ofman et al. 2012), although conclusive evidence for such a distinctly different driver has not yet been observed.

Solar pores are often described as the first evolutionary stage of a typical sunspot structure. Their defining characteristics at lower atmospheric heights are a relatively small (compared to fully developed sunspots) umbral core without the presence of surrounding penumbrae (Sobotka et al. 1999). Cho et al. (2010, 2013) have recently provided observational evidence to support numerous numerical studies (e.g., Knoelker & Schuessler 1988; Cameron et al. 2007) that suggest how rapid cooling within pore umbrae, through the inhibition of convective motion, drives strong downflows which collide with the dense lower layers below the photosphere, producing reflected upflows that can assist with the transportation of significant energy flux to chromospheric heights. Furthermore, the general properties associated with pores are often similar to those found in fully developed sunspot umbrae, including their temperatures and magnetic field inclination angles (Kopp & Rabin 1992; Muglach et al. 1994; Sütterlin et al. 1996; Criscuoli et al. 2012). As with sunspots, the highly magnetic nature of pores allow them to act as efficient waveguides for magnetoacoustic oscillations. Using the TRACE satellite, Balthasar et al. (2000) studied the upward propagation of magnetoacoustic waves in near-circular pores to chromospheric heights. The authors found that the observational signatures best fitted the 'whispering gallery' mode first put forward by Zhugzhda et al. (2000), whereby the detected magnetoacoustic waves induced larger-amplitude magnetic field oscillations than for physically larger magnetic structures (e.g., sunspots). These oscillations rapidly diminish in amplitude towards the edge of the pore's magnetic radius (thus defining a discontinuity boundary of the magnetic field; Hirzberger 2003), which can be substantially larger than its visible radius when observed in optical wavelengths (Keppens & Martinez Pillet 1996). However, due to poor seeing conditions and the resulting inability to accurately co-align their ground-based data with that from the TRACE satellite, Balthasar et al. (2000) were unable to evaluate the energy flux of magnetoacoustic waves reaching chromospheric heights, but instead pointed out the need for higher resolution (both temporally and spatially) observations to better isolate propagating wave trains.

Employing the IBIS instrument on the DST, Stangalini et al. (2011, 2012) and Sobotka et al. (2012, 2013) found evidence for magnetoacoustic waves, with periodicities in the range of $100-1000$ s, leaking upwards into the chromosphere along the pore's inclined magnetic fields. The authors claimed that the energy flux of the upwardly propagating waves was sufficient to balance the entire radiative losses of the pore's chromosphere structure, deemed to be ~ 3400 W m^{-2} averaged over the surface area of the pore, with localised peaks reaching in excess of 10 000 W m^{-2} for particularly bright regions of the pore's chromosphere (Figure 15). It appears from the recent literature that the small-scale, yet highly magnetic nature of solar pores provide idealised wave conduits to efficiently transport energy into higher layers of the solar atmosphere. Interestingly, however, Sobotka et al. (2013) uncovered distinct wave characteristics in a solar pore that also incorporated a light bridge. The authors found that the three minute oscillations dominated the pore umbra, while significant five minute periodicities were observed above the light bridge. Recently, Yuan et al. (2014a) were able to identify identical wave characteristics in a large-scale sunspot that also displayed a prominent light bridge. Here, the authors suggested that the presence of significant five minute oscillations above the light bridge may be the result of the creation of standing magnetoacoustic waves along the thin edge of the light bridge. Ultimately, such findings pose

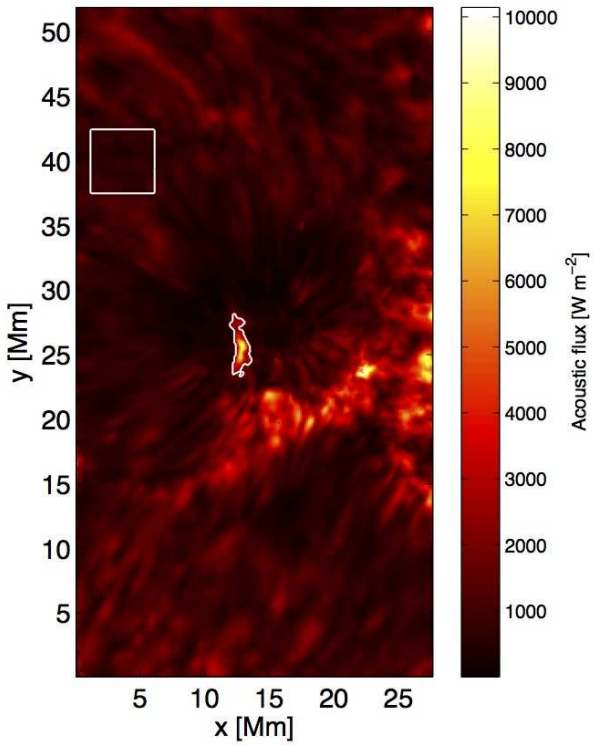

Fig. 15 Map of the total magnetoacoustic power flux, measured from a series of Dopplergrams acquired with the IBIS instrument at the DST, and summed over all magnetoacoustic wave periods in the range of $100 - 1000$ s. The solid white line highlights the extreme localised energy flux, often exceeding $10\,000$ W m^{-2} in the chromosphere, found in a light-bridge region separating two distinct solar pores. A white box outlines a region of the quiet chromosphere, which still displays heightened magnetoacoustic flux on the order of 1000 W m^{-2}. Image reproduced from Sobotka et al. (2013).

challenges to the connectivity and traditional suppression of five minute p-mode oscillations typically observed within the highly magnetic vicinity of pore and sunspot features. Thus, as suggested by Yuan et al. (2014a), modelling the p-mode interaction with a pore and/or sunspot that has a prominent light bridge will be an interesting topic for future theoretical consideration.

A limiting factor in the quest for a global heating mechanism is the fact that solar pores, just like their larger sunspot counterparts, are not sufficiently common to provide continual energy flux to the outer layers of the Sun's atmosphere. Furthermore, due to their limited size, and thus their inability to efficiently inhibit the surrounding convective motions on long-term time scales, solar pores often display minimal signatures at higher atmospheric heights (transition region and corona). Sütterlin (1998) and Sütterlin & Wiehr (1998) employed full-Stokes analysis of pore structures and found that they displayed a vertical magnetic field gradient of ~ 5 G km^{-1}, marginally inflated when compared to large-scale sunspots (1–3 G km^{-1}; Pahlke & Wiehr 1990; Bruls et al. 1995; Rüedi et al. 1995; Berlicki et al. 2006), thus depleting their observational (and magnetic) signatures rapidly as one moves away from the photospheric layer. Nevertheless, pore structures provide observers with one of the most idealised wave conduits in the lower solar atmosphere: a nearly circularly symmetric waveguide that is heavily susceptible to external motions, buffeting and driving forces. As a result, it is foreseen that a multitude of focussed efforts will be undertaken on solar pores in the near future in an attempt to compare observations more readily with MHD wave theory, thus opening up possibilities of being able to refine and/or refute theoretical wave flux predictions.

4.2 Sausage Waves

Sausage oscillations have proven to be one of the most difficult of the compressible wave modes to identify observationally. These waves are typically identified through simultaneous periodic intensity *and* area fluctuations in magnetic solar structures including pores, spicules and coronal loops. The high spatial resolution necessary to identify the fractional area changes meant that early attempts were limited to studying oscillations in the radio emission of coronal loops (e.g., Dröoge 1967). However, more recently Nakariakov et al. (2003) demonstrated that incorrect theoretical interpretation

of the dispersion relations had been applied to previous radio observations. It was found that the long-wavelength cutoff and the highly dispersive nature of the phase speeds were not considered, and therefore the earlier results needed to be revisited to apply these corrections. Aschwanden et al. (2004) subsequently catalogued the relevant radio observations and derived refined properties for these waves through the new theoretical understanding. The oscillations presented were shown to be fast sausage-mode oscillations which were confined to small segments of the magnetic loop that corresponded to higher harmonic modes. The radio frequencies of these waves were shown to be able to constrain the plasma density since the oscillations could only exist at atmospheric heights greater than ~ 40 Mm, representing the apex of the loop where the density contrast with respect to the background is greatest. This work also confirmed the observations of global fast sausage modes by Asai et al. (2001), whereby oscillatory behaviour was evident throughout the entire magnetic loop. These observations were made using microwave images from the Nobeyama Radioheliograph (NoRH; Nakajima et al. 1994) and images from the Yohkoh soft X-ray telescope (SXT; Tsuneta et al. 1991), and provided the first observational evidence that sausage-mode waves may be able to propagate through the lower solar atmosphere providing the magnetic field guidance was sufficiently strong ($B \simeq 40$ G; Asai et al. 2001). In the years since, there have been numerous studies conducted on sausage-mode oscillations at coronal heights (e.g., Srivastava et al. 2008), but evidence to support their existence within the solar chromosphere has proved to be much more elusive.

The first lower atmospheric observations of sausage-mode waves were by Dorotovič et al. (2008). White light observations of a magnetic pore were taken with the Swedish Vacuum Solar Telescope (SVST, now renamed the SST; Scharmer et al. 1985). Periodic area changes in the photospheric pore were observed by analysing the area time series using the wavelet analysis techniques of Torrence & Compo (1998) . This analysis identified area oscillations with periods on the order of $20 - 70$ minutes, and it was suggested that the long periods present were the signature of magnetoacoustic gravity modes, although the existence of these waves have yet to be directly confirmed observationally. This work verified the existence of sausage modes at photospheric heights and showed that highly magnetic pore structures were viable conduits for these waves.

With the development of sensitive high-cadence camera systems (e.g., ROSA), it has become possible in recent years to study sausage-mode oscillatory phenomena at unprecedentedly high spatial and temporal resolutions. Morton et al. (2011) imaged a group of magnetic pores using a blue continuum (4170 Å) channel with ROSA, thus maximising the diffraction-limited spatial resolution and allowing highly sensitive measurements of any area changes to be undertaken. In this study, Morton et al. (2011) employed Empirical Mode Decomposition (EMD; Huang et al. 1998) techniques to identify simultaneous oscillations in the pore area and intensity, with periodicities in the range of $50-600$ s detected. The shorter periods, when compared to the results of Dorotovič et al. (2008), were thought to be a result of the waves being driven by the global solar p-mode spectrum instead of magnetoacoustic gravity modes. However, the majority of the sausage oscillations were only observed in the area time series, without simultaneous intensity perturbations, indicating that they did not possess a large quantity of wave energy. For those oscillations that were concurrently observed in both the area and intensity, it was determined that the intensity fluctuations were 180° out-of-phase with the area changes. Although this characteristic was not interpreted at the time, such a phase relationship was later shown to be evidence that these oscillations were fast sausage mode waves (Moreels et al. 2013). Further study of photospheric sausage modes was conducted by (Dorotovič et al. 2014), with the aim of distinctly identifying features of fast and slow modes. Employing active region observations acquired with the SVST and the Dutch Open Telescope (DOT; Rutten et al. 2004), wavelet analysis was performed on pore and sunspot features to identify fluctuations in the areas and intensities of these structures, with the resulting phase relationships studied using EMD. Standing photospheric oscillations were identified with periods ranging from $4 - 32$ minutes, with the observed modes interpreted as a combination of fast surface and slow sausage modes. Such photospheric work has shown that sausage modes can form in magnetically active structures such as pores and sunspots at photospheric heights, and that both fast and slow modes can exist in the photosphere. This supports the possibility that these waves can carry energy from the solar surface to higher heights to aid atmospheric heating, although the search for such waves within the chromosphere is in it's infancy.

A major piece of work that has initiated our improved understanding of sausage-mode waves in the solar chromosphere was that by Morton et al. (2012). In this study, Hα observations were acquired using ROSA on the DST, with the field-of-view cropped in order to observe a 34×34 Mm^2 region of the quiet chromosphere. The imaged region contained hundreds of fine-scale structures, composed of elongated fibrils and short mottles, which accurately mimic a theoretical flux tube. Alongside the observed incompressible kink modes (see § 5), periodic intensity fluctuations were also seen to exist alongside the expansions and contractions of the visible cross-sections of these chromospheric structures. A difficulty arose when attempting to isolate multiple wave periods as a result of the short lifetimes of the waveguides. Instead, intensity perturbations in a series of time–distance diagrams which lay along the axis of the structure were used (Figure 16). The extracted intensity perturbations, alongside simultaneous area oscillations, identified the presence of sausage-mode waves that were seen in numerous structures across the entire field-of-view. Traditionally, intensity fluctuations observed through narrowband filters are often considered synonymous with density perturbations of the

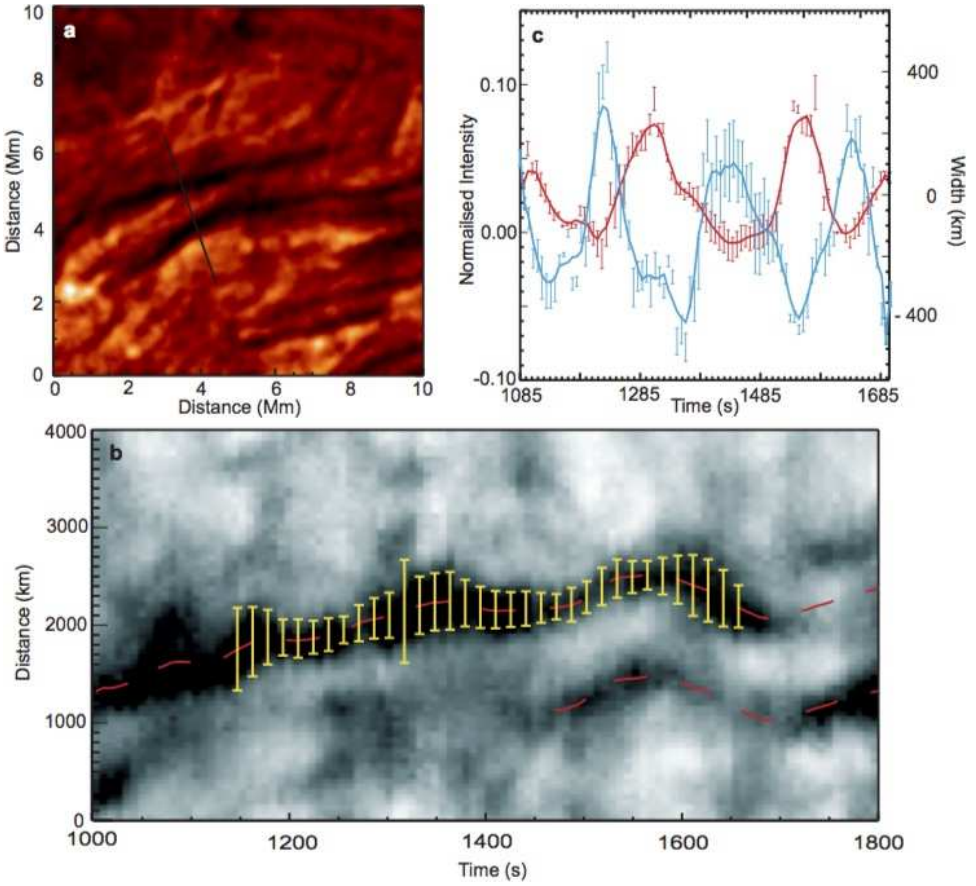

Fig. 16 Panel (a) depicts a cropped ROSA Hα snapshot containing a pair of relatively large dark chromospheric flux tubes. Using the cross-cut (black line) to extract intensity information, panel (b) displays the resulting time–distance diagram revealing the dynamic motion of the waveguides. Times are given in seconds from the start of the data set, while the overplots are the results from a Gaussian fitting routine to show the non-linear fast MHD kink wave (red line shows the central axis of the structure) and the fast MHD sausage mode (yellow bars show the measured width of structure). The transverse motion has a period of 232 ± 8 s and bi-directional phase speeds equal to 71 ± 22 km s^{-1} upwards and 87 ± 26 km s^{-1} downwards. The typical velocity amplitudes are 5 km s^{-1}. The fast MHD sausage mode has a period of 197 ± 8 s, a phase speed of 67 ± 15 km s^{-1} and apparent velocity amplitudes of $1 - 2$ km s^{-1}. Panel (c) displays a comparison between the detected intensity (blue) and width (red) perturbations resulting from the Gaussian fitting. The data points have been fitted with a smoothed 3-point boxcar function. The observed out-of-phase behaviour is typical of fast MHD sausage waves. The error bars plotted are the one-sigma errors on each value calculated from the Gaussian fitting. Image reproduced from Morton et al. (2012).

plasma (e.g., Klimchuk & Bradshaw 2014). However, additional circumstances can manifest that may introduce alternative interpretations for observed intensity fluctuations. As mentioned in § 2, line-of-sight Doppler shifts can result in a narrowband filter sampling a different part of an absorption profile (i.e., the blue/red wings instead of the line core), thus causing a shift in observed intensity (see, e.g., Jess et al. 2007). Also, when employing a broadband filter, the observed intensities can be thought of as following a simple Planck function under the assumption of local thermodynamic equilibrium. Thus, any perturbations in intensity can be interpreted as a signature of local temperature fluctuations. However, this interpretation hinges upon the accuracy of the local thermodynamic equilibrium approximation. Propagation speeds were deduced by Morton et al. (2012), and were shown to be on the order of the Alfvén speed, thus indicating that they are most likely fast sausage modes. It was also inferred that some of these waves are propagating upwards through the atmosphere. This is due to many of the chromospheric structures being inclined with respect to the solar surface, allowing upwardly propagating waves to be identified within single-channel images. Analysis of the energetic properties of these waves was conducted to ascertain their potential suitability as conduits for atmospheric heating. An important parameter to calculate when undertaking energy analyses is the dimensionless variable, 'ka', the product of the wavenumber, k, and waveguide half-width, a. Waves are defined as 'trapped', whereby they retain energy as they propagate in the absence of external damping, if ka is greater than a constant dependent on the internal and external Alfvén speeds (Cally 1986). In terms of external damping, there is a rich variety of viable dissipation mechanisms identified for various wave modes manifesting throughout the solar atmosphere. These include resonant absorption and phase mixing (e.g., Goossens & De Groof 2001; Ruderman & Roberts 2002; Goossens et al. 2002), turbulent mixing (van Ballegooijen et al. 2011), in

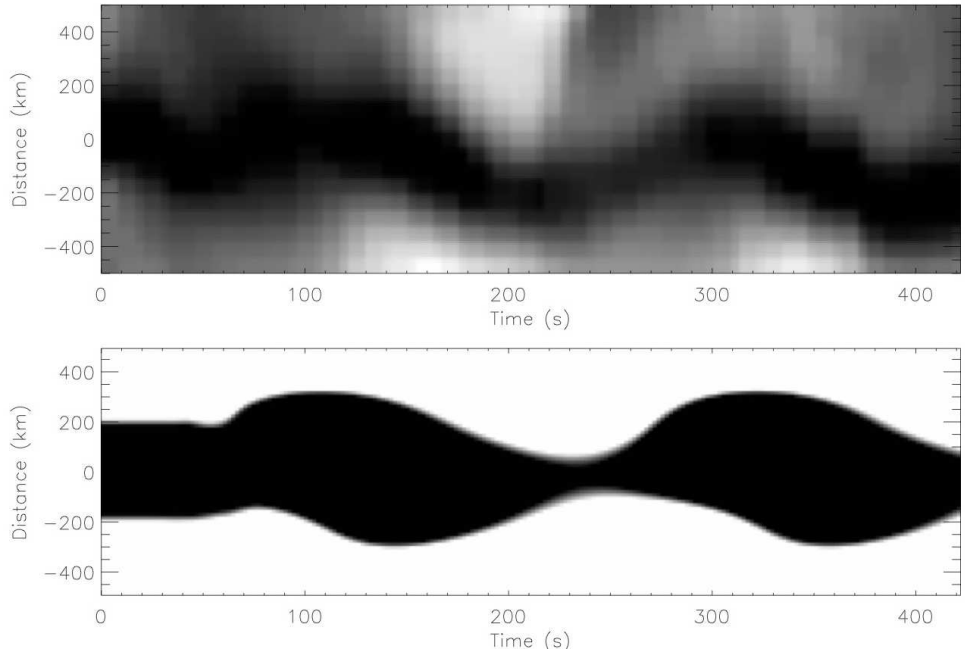

Fig. 17 The top panel displays a time–distance diagram of high-cadence chromospheric Hα observations cut perpendicularly through the central axis of a spicule. The bottom panel displays a comparitive time–distance diagram of simulated chromospheric spicule densities having first been driven by out-of-phase compressive oscillations at the solar surface. There is a remarkable degree of similarity between the two panels, with both kink (transverse displacement of spicule axis) and sausage (periodic compressions and rarefactions) modes visible. This clearly shows how the velocity gradients generated as a result of out-of-phase compressive oscillations at the footpoints of spicule structures can create both compressible *and* incompressible wave modes at higher atmospheric heights. Image adapted from Jess et al. (2012b).

addition to examples of mode conversion (e.g., Ulmschneider et al. 1991; Kalkofen 1997) and thermal conduction (Ofman & Aschwanden 2002; Mendoza-Briceño et al. 2004; Erdélyi et al. 2008). Furthermore, the waves may be defined as 'leaky' should they readily dissipate their embodied energy without first being prompted by external effects. Morton et al. (2012) estimated the internal and external Alfvén speeds based on the known properties of a cold, dense chromosphere and defined the ka value at which the waves transferred across the trapped/leaky divide as $ka \simeq 0.2$. The wave activity displayed in Figure 16 was used to estimate $ka \sim 0.09 \pm 0.03$, with the results suggesting that the observed sausage-mode waves lie within the leaky regime and will therefore radiate energy away from the magnetic structure without the need for external damping. This is clearly an advantageous characteristic to promote localised atmospheric heating, and estimates of the individual wave energies produced values on the order of 11700 ± 3800 W m^{-2}. This is a significant amount of energy, and Morton et al. (2012) highlighted the fact that if only 5% of the chromosphere was connected to the corona via flux tubes then a total energy flux of 460 ± 150 W m^{-2} would be available to the corona for atmospheric heating. Despite contemporaneous SDO imaging, it was unclear how the observed sausage-mode waves interacted with the corona. However, these early results indicate that sausage oscillations may play an important part in supplying both the chromosphere and the corona with the necessary energy flux to maintain their elevated temperatures.

Supplementary images of the lower solar atmosphere highlighted that MBPs may be the photospheric anchor points of the chromospheric waveguides undergoing sausage-mode oscillations (Morton et al. 2012). Although no information is provided by the authors regarding whether simultaneous oscillations are present at lower atmospheric heights, this suggestion is consistent with the previous work of Jess et al. (2012b) who examined the connectivity between photospheric MBPs and chromospheric spicules. The primary aim of this work was not to study sausage-mode oscillations, but instead to examine the mode-coupling between compressible and incompressible waves found in MBPs and their chromospheric spicule counterparts. Through use of G-band, Ca II K and Hα filtergrams obtained with ROSA, Jess et al. (2012b) found compressive fluctuations across the body of an isolated photospheric MBP that coupled into incompressible transverse oscillations in the lower chromosphere. Importantly, the compressive magnetoacoustic oscillations were found to be 90° out-of-phase at opposite sides of the MBP. Employing the Lare2D numerical code (Arber et al. 2001) and modelling a spicule as a thin magnetic flux tube, the authors found that a 90° out-of-phase behaviour at the photospheric level not only produced velocity gradients that caused the spicule axis to displace transversally, but the motions also induced compressions and expansions in the waveguide, thus promoting the manifestation of both compressible sausage modes and incompressible transverse waves at chromospheric heights (Figure 17). The similarity between the observed

and simulated spicule dynamics clearly shows how thin, magnetic structures omnipresent throughout the solar chromosphere can readily support sausage-mode wave generation and propagation. While no analyses of the sausage-mode energetics was performed by Jess et al. (2012b), the work of Morton et al. (2012) highlights the impressive energy these waves can carry; more than sufficient to balance the extreme localised radiative losses experienced in the chromosphere and corona.

The study of sausage mode waves in the chromosphere is a new and developing field of research. Despite the small volume of published material, their importance in terms of energy transport through the dynamic chromosphere is becoming more clear. It has been shown that these waves can be generated in the photosphere through a variety of mechanisms, including the mode-conversion of fundamental p-mode magnetoacoustic oscillations. It has also been established that sausage-mode oscillations can carry a significant energy flux, leading to the conclusion that these waves may act as an energy conduit for supplying higher atmospheric heights with the necessary energy to balance radiative losses. Many of these outstanding questions can be answered by employing new and existing technology. For instance, a key goal for sausage mode research is to utilise multiwavelength imaging to identify propagation from the photosphere to the chromosphere and beyond in an attempt validate the efficiency at which they transport energy. In this regard, the high resolution imaging of ROSA will continue to be vital. Complimentary approaches would involve imaging spectroscopy techniques (through use of the IBIS and CRISP instruments) to examine the line-of-sight velocities, thermal and non-thermal spectral widths, and the manifestation of spectral line asymmetries in order to more accurately categorise the wave modes, phase speeds, oscillation amplitudes and energetics through prominent phase relationships intrinsic to each particular mode (Moreels & Van Doorsselaere 2013).

While the contribution of slow magnetoacoustic waves to energy transportation needs to be re-assessed in light of these recent results, incompressible (or Alfvénic) waves have consistently been a more-favoured mechanism for efficient energy transport. However, it wasn't until 2007 that direct evidence for ubiquitous incompressible waves was first presented. In the following section, we draw upon these post-2007 results and review the publications related to the direct observations of chromospheric incompressible waves. We demonstrate that their ubiquity has allowed for the typical properties of these waves to become relatively well constrained, although there are still some outstanding questions. We also discuss investigations that have provided clues as to how these waves are generated and how they evolve as they propagate through the chromosphere.

5 Incompressible Waves

Incompressible waves are characterised by $\nabla \cdot \delta \boldsymbol{v} = 0$ (see § 3.2). In practice, waves that nearly satisfy this condition are labelled as incompressible. Therefore, from a physical point of view, incompressible waves can exhibit small pressure perturbations while the dominant restoring force is magnetic tension. The lack of compression makes it particularly difficult to dissipate the wave energy unless large gradients in the Alfvén speed exist (e.g., Heyvaerts & Priest 1983). This has made incompressible waves a favourable mechanism for transferring energy from the convective motions in the photosphere up into the upper chromosphere and coronae, playing the role as the dominant energy carrier in many simulations that appear to be able to generate hot corona (e.g., Cranmer & van Ballegooijen 2005; Suzuki & Inutsuka 2005; Verdini & Velli 2007; Matsumoto & Shibata 2010).

In a plasma medium composed of fine-scale magnetic structures, the incompressible (or nearly incompressible) motions can be split into two main categories, those of MHD fast kink motions (in the long wavelength limit, i.e., $\lambda \gg a$, where λ is the wavelength and a is the radius of the waveguide) and the torsional Alfvén mode (for theoretical discussions of the individual mode properties see, e.g., Spruit 1982; Edwin & Roberts 1983; Bennett et al. 1999; Goossens et al. 2009). Over the last eight or so years, periodic motions of fine-scale structures in the magnetically dominated upper chromosphere, in both imaging and spectroscopic observations, have been associated with the presence of both types of incompressible wave. These recent observations have built upon numerous historic reports of periodic variations in Doppler signals and filtergrams of various chromospheric spectral lines, which were often interpreted in terms of Alfvén waves, although the exact nature of the signals remains ambiguous (see, e.g., Nikol'Skii & Sazanov 1967; Pasachoff et al. 1968; Sawyer 1974; or Zaqarashvili & Erdélyi 2009 and Mathioudakis et al. 2013 for recent reviews). The advantage of recent observations is that they possess the ability to observe at high-spatial and temporal resolutions, allowing fine-scale structures in the upper chromosphere, alongside its intrinsic dynamics, to be resolved. This has only been made possible through; *(i)* seeing-free, space-based chromospheric observations provided by Hinode/SOT; *(ii)* advances in reducing atmospheric distortion through both instrumental (e.g., adaptive optics) and image reconstruction techniques such as speckle (Wöger et al. 2008) and Multi-Object Multi-Frame Blind-Deconvolution (MOMFBD; van Noort et al. 2005) suitable for ground-based observations, e.g., ROSA at the DST (Jess et al. 2010c) and CRISP at the SST (Scharmer et al. 2008); *(iii)* increased spectral resolution, e.g., IBIS at the DST (Cavallini 2006) and the TRI-Port Polarimetric Echelle-Littrow spectrograph at the SST (TRIPPEL; Kiselman et al. 2011).

The interpretation of signatures pertaining to the torsional Alfvén wave is still contentious (for a detailed overview see Mathioudakis et al. 2013). On the other hand, the interpretation of the observed motions of fast kink waves is fairly straight-forward, with the displacement of the central axis of the magnetic structure unambiguous in images, e.g., Figures 7,16 & 18.

5.1 Observations and measurements

In this section, we will review the observations of both types of incompressible motions in the chromosphere. However, we believe it necessary to split the observations into separate categories based on the nature of the chromospheric structure. The reason for this will become obvious after consideration of the different observations. Ultimately, these categories essentially pertain to whether the features are thought to be closed within the chromosphere, or open and connected to the corona, which would undoubtedly lead to differing plasma properties, something apparently reflected in the measured properties of the waves.

Before discussing the observations, we bring the readers attention to a particular point of potential interest. The measurements of incompressible wave phenomena have been performed using data from a variety of spectral lines that are typically associated with the chromosphere, e.g., Hα, Ca II H/K and the Ca II infrared triplet at 8542 Å (see § 2 for a more detailed overview). These lines have different properties with respect to opacities and formation regions in the atmosphere (e.g., Rutten 2007; Leenaarts et al. 2009; Leenaarts et al. 2012), hence the local plasma properties could differ for chromospheric features observed in various spectral lines, potentially leading to subtle variations in measured wave parameters. The differing behaviour of the related chromospheric phenomena is highlighted in Rouppe van der Voort et al. (2009), who report higher velocities in Rapid Blue-shifted Events (RBEs) observed in Hα than in Ca II 8542 Å and suggest the larger opacity in Hα allows the sampling of higher layers. While the effects of this are easier to avoid in limb observations, where the apparent height in the atmosphere of a wave measurement can be deduced, this is not the case for on-disk measurements. At present, there is no clear evidence for any variation in wave properties measured using different lines – although this may be due to the fact such an investigation has not yet been undertaken. With this said, we give the wavelength used during each observation discussed in the following but do not give any significance to this when comparing results.

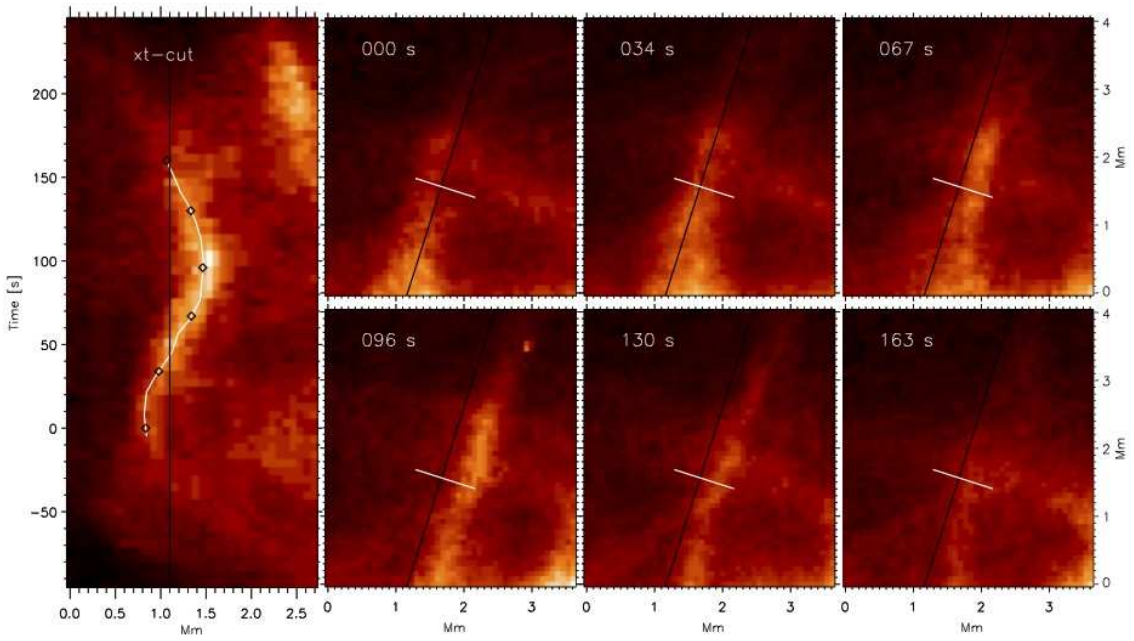

Fig. 18 Examples of fast kink wave motion observed in chromospheric spicule structures. The panels demonstrate the larger amplitude motions observed in spicules, with the largest (left-hand) panel showing a time–distance diagram, while the smaller panels reveal sequential snapshots of the spicule. This is in contrast to the typically smaller-displacement fast kink waves present in fibrils (see Figure 16). Image reproduced from De Pontieu et al. (2007a).

5.1.1 Spicules

It is generally well known that spicules are jets of chromospheric material that outline almost vertical magnetic field lines and penetrate into the upper layers of solar atmosphere (e.g., Beckers 1968). Spicules are predominantly observed at network boundaries, appearing as a dense forest at the limb and best seen on-disk in Hα wing images after the more 'static' component of the chromosphere is removed (Zirin 1988; Rutten 2007). More recently, there has been the sub-classification of spicules into Type-I and Type-II varieties (De Pontieu et al. 2007b). The observation of the second type of spicule is said to be only possible with high cadence, seeing free observations, such as those provided by Hinode/SOT. Type-II spicules are apparently faster moving than the traditional Type-I spicule and the material that composes them is not seen to fall back towards the surface, suggesting the plasma may be heated to coronal temperatures as it rises and these spicules may play an important role in supplying heated mass to the corona (De Pontieu et al. 2011). However, this idea is currently contentious with vigorous opposition to the classification of the spicules (e.g., Zhang et al. 2012) and their contribution to coronal mass supply (Madjarska et al. 2011; Klimchuk 2012; Goodman 2014; Patsourakos et al. 2014; Klimchuk & Bradshaw 2014; Petralia et al. 2014).

Hinode/SOT observations suggested the need for refined spicule classifications, and also revealed that spicules undergo pronounced transverse displacements (De Pontieu et al. 2007a). Limb observations in Ca II H of a coronal hole found that the majority of spicules underwent transverse displacements on the order of $500 - 1000$ km with time-scales of 10 to 300 s, and had typical velocity amplitudes of $10 - 20$ km s^{-1}. It appears that the authors primarily measured uni-directional displacements, i.e., no sign of periodicity, however, they did report that the longer lived spicules demonstrated signatures of oscillatory motion (e.g., Figure 18). Moreover, by comparing the observations to Monte Carlo simulations, the authors estimated that the typical period of oscillations had to lie between $150 - 300$ s. The subsequent interpretation of the authors was that these observations could be explained by Alfvén waves, which led to intense debate (Erdélyi & Fedun 2007a; Van Doorsselaere et al. 2008). As mentioned in the introduction to this section, in a highly structured atmosphere – particularly one that exhibits structuring of the density perpendicular to the direction of the magnetic field – the pure Alfvén wave is a torsional motion. The transverse displacements of the waveguide central axis represents the fast kink mode, which is Alfvénic in the sense that it is highly incompressible in the observable limit and that magnetic tension is the dominant restoring force (Goossens et al. 2009). While this may seem like a technical detail, serious discrepancies can occur in estimates of the wave energy flux depending on whether one assumes the observed waves are Alfvén or kink waves (Goossens et al. 2013; Van Doorsselaere et al. 2014). Assuming the waves were Alfvén waves, De Pontieu et al. (2007a) calculated that they transported around $4000 - 7000$ W m^{-2}. Recently, Van Doorsselaere et al.

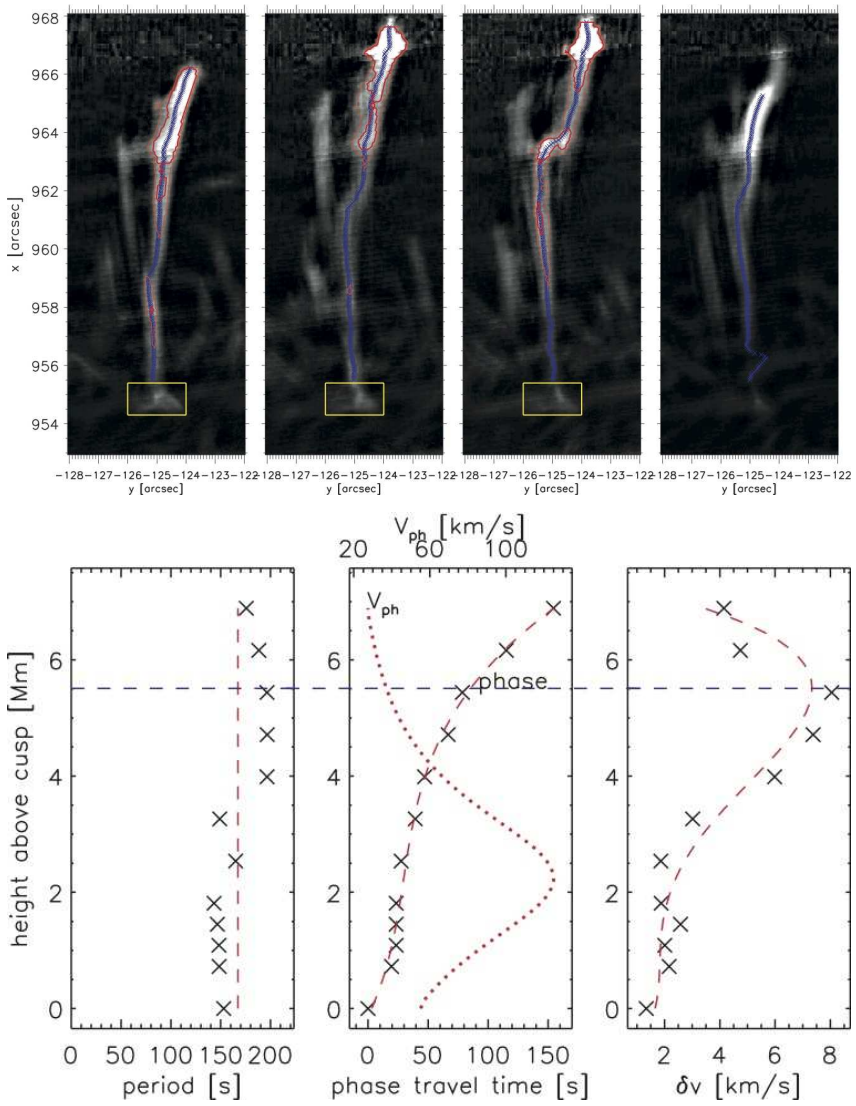

Fig. 19 A spicule oscillation observed with Hinode/SOT, where the upper panels display the spicule structure and highlight the propagation of a wave front along the feature. The lower panels show the measurements of the kink wave properties as a function of atmospheric height. Here δv is the velocity amplitude and v_{ph} is the propagation velocity. Images adapted from He et al. (2009b).

(2014) re-evaluated the estimates of De Pontieu et al. (2007a), and for typical filling factors of $5-15\%$ the energy flux is greatly reduced to $200-700\ \mathrm{W\,m^{-2}}$. The physical reason for this reduction in energy flux is that for a kink wave the energy is strongly localised in the neighbourhood of the flux tube density enhancement. This is not the case for the more idealised bulk Alfvén wave scenario, where the waves are assumed to travel through a homogeneous plasma, resulting in a spatially uniform energy flux. The bulk Alfvén wave model is therefore especially unsuited to thin, overdense magnetic structures such as spicules and fibrils. Additionally, De Pontieu et al. (2007a) provide an estimate for the typical Alfvén speeds in spicules by using previous measurements of spicular magnetic fields ($B \sim 10$ G) and densities ($\rho \sim 10^{-11}-10^{-10}\ \mathrm{kg\,m^{-3}}$), estimating $v_A = B/\sqrt{\mu_0 \rho} \sim 45-200\ \mathrm{km\,s^{-1}}$.

Before continuing, it is worth noting that the values for the propagation speed of the fast kink wave is actually a weighted average of the internal and external Alfvén speeds. The subsequent propagation velocity will then be greater than the internal Alfvén speed of the spicule plasma, i.e. that quoted by De Pontieu et al. (2007a). Nonetheless, it is clear that the fast kink waves, if propagating, will traverse a typical spicule length in a matter of tens of seconds to minutes. Additionally, the value of magnetic field used is conservative, with spectropolarimetric inversions suggesting field strengths up to ~ 50 G may be present (Trujillo Bueno et al. 2005; López Ariste & Casini 2005; Centeno et al. 2010), hence, potentially providing larger values of the Alfvén speed than those given. Combining the fast propagation speeds with the long wavelengths of kink waves, e.g., 20 000 km for a wave with a period of 100 s, this makes it

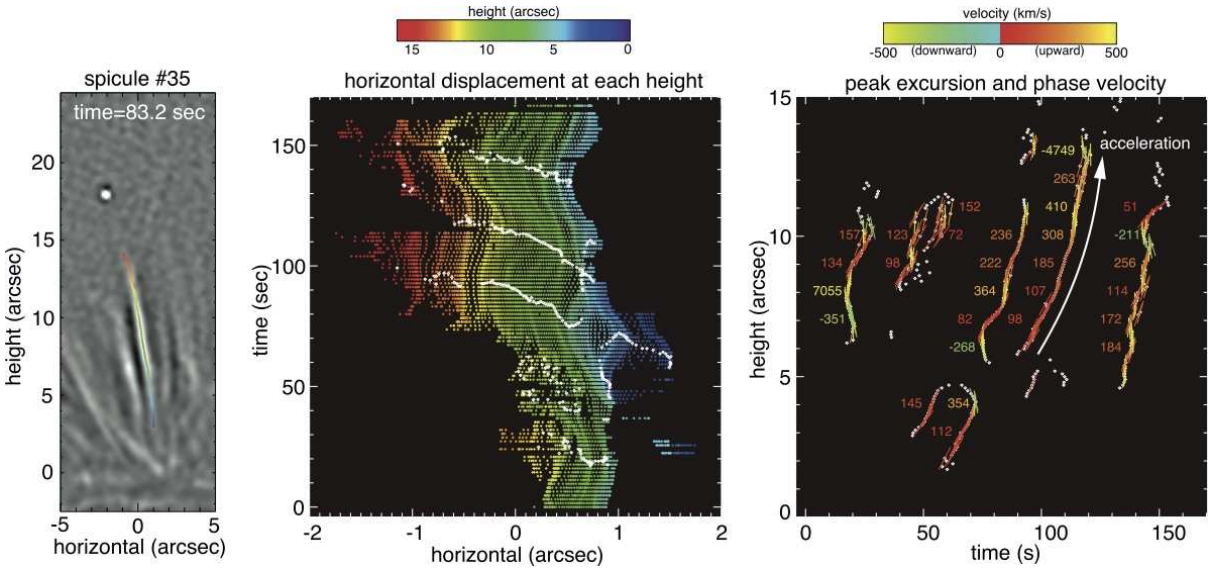

Fig. 20 Examples of wave propagation along an off-limb spicule. The left panel shows the spicule that has been highlighted with coloured line, where the colour variation corresponds to increasing atmospheric height. The middle panel shows the results from following the spicule over time. The colours correspond to those in the first panel and show the transverse displacement at each height along spicule (horizontal axis) with time (vertical axis). The displacement is observed to travel along the spicule, which is highlighted by the white lines. The right panel shows the propagation speeds calculated from the gradient of the white lines. Image reproduced from Okamoto & De Pontieu (2011).

extremely difficult to observe and measure the propagation of the waves along spicules unless high cadence data is used and rigorous measurement techniques are employed.

The presence of transverse motions of spicules was also reported in Suematsu et al. (2008), giving similar values for amplitudes but, interestingly, noting that the lateral motions and oscillations become more prominent as height increases. This would suggest that the amplitude of the waves increases with height in the atmosphere, and would imply a decrease in the average density with height as one might expect (see § 5.2). Furthermore, Suematsu et al. (2008) highlight that some spicules show evidence for rotational motions. A number of authors also investigated spicules with Hinode/SOT, analysing a few individual spicule oscillations in more detail. Kim et al. (2008) studied three spicule oscillations in what appears to be a coronal hole region. Using time–distance diagrams, they saw wave motion at numerous heights along the spicules and reported that there was no evidence of phase shifts between the differing heights, hence the authors gave an estimate for the phase speeds of the perturbations as $260 - 460$ km s^{-1}. However, the data used has a cadence of 16 s and it is unclear which techniques were used to measure spicule displacement and phase shifts, adding to the uncertainty in the given values.

A thorough analysis of four spicule oscillations in a coronal hole was undertaken by He et al. (2009a). Notably, they found evidence for waves with periods < 50 s, significantly less than that suggested by the Monte Carlo comparisons of De Pontieu et al. (2007a). Additionally, He et al. (2009a) provided the first measurements of propagation speeds of the kink waves using cross-correlation of signals from time-distance diagrams that were generated at various positions along the spicules. The measured propagation speeds ranged between $59 - 150$ km s^{-1} and all waves were upwardly propagating. They also show evidence for an increase in wave amplitude with height along two of the spicules analysed, supporting the reports of Suematsu et al. (2008). Another investigation into fast kink waves in spicules was carried out by He et al. (2009b), although this time only one event was studied in detail. The spicule was located above plage in an active region. In this event, the amplitude and phase speed were able to be measured at 12 separate positions along the spicule (see Figure 19). The measurements clearly showed initial increases in velocity amplitude and phase speed, followed by decreases in both quantities. Perhaps surprisingly, the measured phase speed of the wave is as little as 25 km s^{-1} in the upper sections of the spicule, suggesting a weakening of magnetic field with height. The observed variations of the velocity amplitude and phase speed are not simultaneous, suggesting a complex variation in plasma parameters (see § 5.2 for further details).

A significant investigation into the wave properties of spicules was performed by Okamoto & De Pontieu (2011). Again, the focus was on the properties of coronal hole spicules, although a unique automated technique to track the spicules was developed, extracting spicules from images, locating the central axis of the spicules along their length and following them over time. The technique is subject to various conditions, first removing short-lived and small-scale structures. A total of 89 suitable spicules were identified and used for further study, with the authors suggesting

that they are likely isolating Type-II spicules. In Figure 20 we show an example of their results. The middle panel in the figure contains a significant amount of information and we will try to provide a brief summary here, however, it is strongly suggested an interested reader refers to Okamoto & De Pontieu (2011) for a full explanation. The middle panel shows the horizontal displacements of a spicule as a function of time, for each position along the spicule length, where each position is given a different colour. The maximum displacements of the spicule are highlighted by the white lines. It can be seen that the position of the maximum displacements moves upwards or downwards along the spicule as time increases, suggesting the maximum displacement is propagating along the spicule. Using the gradient of these white lines, propagation velocities of the waves can be obtained and are shown in the right hand panel. The average properties of the waves observed gave typical periods of 45 ± 30 s and velocity amplitudes of 7.4 ± 3.7 km s^{-1}. Interestingly, this is almost half the value suggested by the measurement of predominantly uni-directional motions in De Pontieu et al. (2007a). This has implications for the estimated energy flux – if the amplitudes are half those of previously reported it means the spicules may only carry a quarter of the energy flux previously estimated by De Pontieu et al. (2007a). The authors find that a majority of the waves are upwardly propagating, with approximately one third downwardly propagating. The results also suggest that, on average, the phase speeds increase with height. The authors additionally refer to the presence of standing waves being present, however, the observational evidence is unconvincing. The authors suggest that when upwardly and downwardly propagating waves pass each other a standing wave is present (these features are seen in Figure 20 as anomalously high values of phase speed). A superposition of counter propagating waves is not, however, a standing wave. By definition a standing wave has fixed nodes which do not oscillate. What appears to be observed is just the temporary superposition of counter propagating waves, which would cause the apparent anomalous high phase speeds. Further objections to the interpretation of standing waves are given in Lipartito et al. (2014).

Another significant and thorough analysis of spicule properties was carried out by Pereira et al. (2012), and the results also included statistics on spicule displacements from coronal holes, quiet Sun locations and active regions. The study provides statistically significant measurements for both transverse displacements and velocity amplitudes. The authors measure both uni-directional and sinusoidal motions, further splitting the results between spicules that show either parabolic or linear trajectories, which essentially tries to distinguish between Type-I and Type-II varieties. They suggest that 'linear spicules' are dominant in both coronal holes and quiescent regions, with parabolic profiles rarely occurring in these regions. A few other papers have also reported the transverse motions in spicules, and we briefly summarise them here. Tavabi et al. (2011) and Ebadi et al. (2012) both demonstrate examples of spicules that undergo transverse displacements but do not provide any solid analysis of the events. Jess et al. (2012b) provide a unique study of spicules with an on-disk observation in Hα and provide evidence regarding the potential excitation mechanism (see § 5.3 for further discussion). Yurchyshyn et al. (2012) also note the presence of periodic and linear transverse motions in Hα observations of on-disk Type-II spicules. However, these observations appear to be of RBEs rather than Type-II spicules (although there is the suggestion that these two phenomenon are one in the same – Rouppe van der Voort et al. 2009).

Aside from the transverse displacement of the spicules, evidence for torsional motions in spicules has been provide by De Pontieu et al. (2012). Using both Hα and Ca II H, the authors are able to resolve oppositely directed Doppler shifts on either side of the spicule suggesting motion in opposite directions. Using Monte-Carlo simulations, the authors suggested that amplitudes of ~ 30 km s^{-1} and periodicities of $100 - 300$ s represent the observed Doppler signatures well. However, it has been demonstrated by Goossens et al. (2014) that it also possible to interpret the observed Doppler velocity in terms of a kink motion (see, § 3 for more details). Rutten (2013) also reports evidence for torsional motions in spicules using Dopplergrams, showing examples of spicules with red and blue shifts apparently on opposite sides of the feature. However, the author compares red and blue wing Hα ($\pm$600 mÅ) images that are taken 1 minute apart so it is unclear whether this is torsional behaviour or just transverse displacement of the spicule along the observer's line-of-sight. As the torsional motions are likely to propagate at the Alfvén speed, they will traverse the spicule relatively quickly. Hence, the blue-red asymmetry across the spicule will undergo a relatively rapid evolution, fading and then reappearing with the asymmetry on opposite sides due to the periodicity of the waves.

5.1.2 Fibrils

Chromospheric fibrils are elongated structures that span supergranular cells, lying almost horizontally in the chromosphere (Foukal 1971; Zirin 1972). The fibrils are typically associated with strong concentrations of photospheric flux, i.e., network boundaries or plage regions. They spread out from these regions, showing a greater degree of topological organisation in active regions compared to quiet regions. The other footpoint of fibrils is assumed to lie within opposite polarity flux, but this is not always evident (Reardon et al. 2011). Fibrils appear as dark features in the line cores of chromospheric absorption lines as a result of them being a local density enhancement that leads to increased scattering of the photospheric radiation (e.g., Leenaarts et al. 2012). The first resolved observation of kink waves in fibrils appears to be

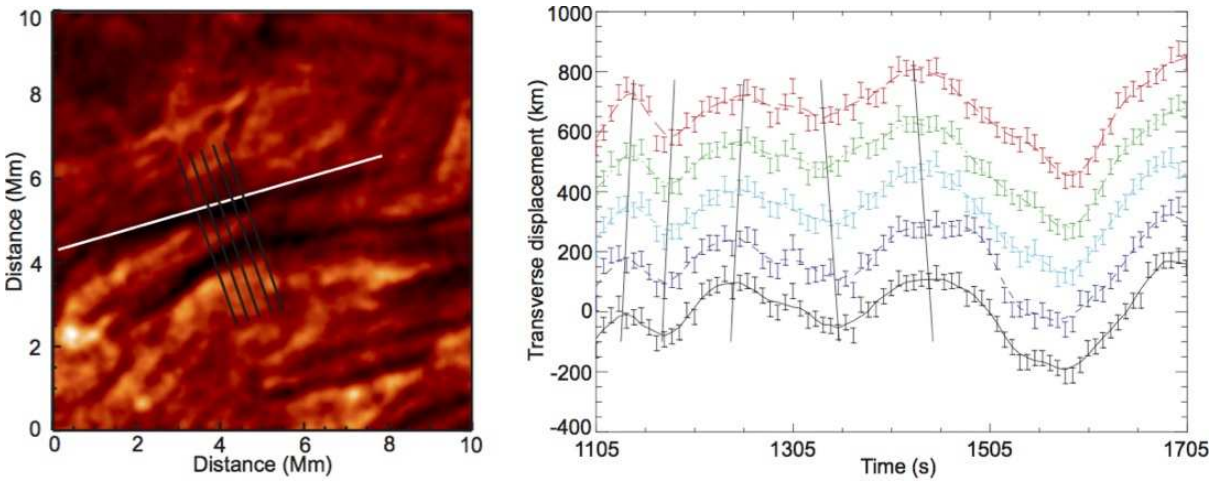

Fig. 21 Hα observations of chromospheric fibrils. The left panel displays a cropped field-of-view containing elongated dark fibril structures, with one axis highlighted by the solid white line (same fibrilar structures as displayed in Figure 16). Perpendicular black lines indicate locations where cross-cuts were made, with the right panel displaying the displacement of the fibrils central axis from each of the cross-cuts. The straight lines connect the peaks and troughs of the sinusoidal displacement and highlight the propagation of waves along the fibril. Image reproduced from Morton et al. (2012).

that of Pietarila et al. (2011), who measured a single oscillating feature in Ca II 8542 Å – although the authors mention that there is evidence for further transverse displacements in other features. It was found that the velocity amplitude of the wave was on the order of $1\ \mathrm{km\,s^{-1}}$, significantly less than that typically associated with the fast kink waves measured in spicules. Additionally, an attempt was made to measure the speed of propagation from phase analysis, where small phase shifts were measured giving a value of $190\ \mathrm{km\,s^{-1}}$. However, the authors suggest that the measurement is subject to large uncertainties and are not convinced by the estimated value, stating that the actual speed of propagation may be either too fast (leading to small phase shifts) to be measured robustly or the wave is simply not propagating.

A more general look at transverse waves in quiet Sun fibrils in Hα is given in Morton et al. (2012), who use data from the ROSA instrument. The authors observe evidence for ubiquitous transverse wave motions of the fibrils, along with evidence for fast propagating compressional modes (see, § 4.2 for further details). They measure the unidirectional displacements of over 50 dark fibrils using time–distance diagrams, but also measure and report a number of sinusoidal displacements. The observed displacements have a mean values of 315 ± 130 km and velocity amplitudes of $6.4 \pm 2.8\ \mathrm{km\,s^{-1}}$, suggesting the waves had significantly smaller amplitudes than those observed at the limb in a similar manner (i.e., De Pontieu et al. 2007a). Additionally, measurements of phase speeds of some of the observed transverse displacements reveal evidence for counter propagating waves travelling with speeds in the region of $50 - 250\ \mathrm{km\,s^{-1}}$ (Figure 21). Subsequent studies of the fibrils in Hα ROSA data were given in Morton et al. (2013, 2014). Here, an advanced feature tracking routine was exploited to examine the periodic motions of the fibrils in time–distance diagrams and ~ 740 and ~ 840 individual measurements were made in active and quiet Sun regions, respectively. This extended analysis suggested that typical displacement amplitudes and velocity amplitudes were smaller than those in Morton et al. (2012) (see Table 3) and periods were 120 ± 50 s. As noted in Morton et al. (2014), these results are subject to a series of observational constraints, with higher frequency waves ($P < 50$ s, where P is period) likely to be underrepresented since they will have displacements on the order of the spatial resolution, while lower frequency waves ($P > 250$ s) will also be underrepresented as the lifetimes of fibrils are of the same order. The large number of events measured additionally enabled the authors to derive the first estimates for the velocity power spectra of the chromospheric transverse displacements – this exciting result will be discussed further in § 5.3.

5.1.3 Other features

In this section we briefly discuss measurements of transverse displacements in other chromospheric structures. This is not to belittle the importance of these features, it is simply because it is unclear how these structures fit into the chromospheric scene.

The first of these are RBEs, which are apparently fast-moving plasma flows observed in the blue wings of chromospheric spectral lines. Rouppe van der Voort et al. (2009) provides a thorough study of the phenomenon, and are able to measure 35 examples of the transverse displacement of the RBEs. The average measured amplitudes are 0.3 Mm for dis-

Table 3 Average (or measured) properties of fast kink waves.

Structure	Region	ξ (km)	P (s)	v (km/s)	c_{ph} (km/s)	No. Events	Reference
Spicule	CH	$200 - 500$	$150 - 350$	20 ± 5	-	95	De Pontieu et al. (2007a)
	CH	-	$60 - 240$	20 ± 5	-	-	Suematsu et al. (2008)
	CH	1000	130	15	460	1	Kim et al. (2008)
		700	180	8	310	1	
		800	170	9	260	1	
	CH	36	48	4.7	75-150	1	He et al. (2009a)
		36	37	6.1	59-117	1	
		130	45	18.1	73	1	
		166	50	20.8	109-145	1	
	CH	55 ± 50	45 ± 30	7.4 ± 3.7	160-305	89	Okamoto & De Pontieu (2011)
		600	180	22	-	1	Ebadi et al. (2012)
	QS	670	220	19.2	-	1	Jess et al. (2012b)
		630	139	28.3	-	1	
		160	65	14.8	-	1	
		410	158	16.2	-	1	
		380	129	18.5	-	1	
		200	105	11.8	-	1	
		190	171	7.2	-	1	
	AR	283 ± 218	–	14 ± 112	-	112	Type-I -Pereira et al. (2012)
	AR	463 ± 402	–	18 ± 12	-	58	Type-II
	QS	245 ± 211	–	16 ± 11	-	174	
	CH	342 ± 257	–	20 ± 12	-	170	
Fibrils		135	135	1	190	1	Pietarila et al. (2011)
	QS	315 ± 130	–	6.4 ± 2.8	50-90	103	Morton et al. (2012)
	QS	71 ± 37	94 ± 61	4.5 ± 1.8	-		Morton et al. (2013)
	QS	94 ± 47	116 ± 59	5.5 ± 2.4	-	841	Morton et al. (2014)
	AR	73 ± 36	130 ± 92	4.4 ± 2.4	-	744	
RBEs		300	–	8	-	35	Rouppe van der Voort et al. (2009)
	CH	200	–	$4 - 5$	-	960	Sekse et al. (2012)
	QS	200	–	8.5	-	1951	average - Sekse et al. (2013)
		220	–	11.7	-	1951	maximum
Mottles	QS	200 ± 67	165 ± 51	8.0 ± 3.6	-	42	Kuridze et al. (2012)
	QS	~ 172	120 ± 10	~ 9	50	1	Kuridze et al. (2013)
	QS	252	180 ± 10	8.8 ± 31	101 ± 14	1	
	QS	327	180 ± 10	11.4 ± 3.3	79 ± 8	1	

placement and $8\ \mathrm{km\,s^{-1}}$ for velocity. Subsequent studies by Sekse et al. (2012, 2013) provide similar numbers following a larger statistical survey (see Table 3), and the authors demonstrate that the distributions are similar for measurements in both Hα and Ca II 8542 Å. They also show that the average transverse velocity ($4 - 8\ \mathrm{km\,s^{-1}}$) is approximately one-third to a half of that associated with the maximum transverse velocities ($8 - 11\ \mathrm{km\,s^{-1}}$). Sekse et al. (2013) takes an additional step and classifies the RBEs in relation to the type of transverse displacement they observe, i.e. uni-directional and periodic. Subsequently, they found that the maximum velocity amplitudes for the periodic motions ($7.5\ \mathrm{km\,s^{-1}}$) are less than the uni-directional motions ($11.8\ \mathrm{km\,s^{-1}}$), similar to measurements in both spicules and fibrils. Kuridze et al. (2012, 2013) analysed the transverse displacements of chromospheric mottles thought to be connected to spicules. A number of periodic events are analysed and provide displacements, velocity amplitudes and periods that are in line with those seen in spicules. Kuridze et al. (2012) also measure the time variation of the amplitude, which in a number of cases appear to decay with time. Although the authors talk about damping times in the paper, it is likely that the events are propagating wave packets of finite length rather than damped wave motion.

Preceding the spicule observations of apparent torsional motions, Jess et al. (2009) also demonstrate evidence for torsional Alfvén waves in the chromospheric counterpart to an MBP. Utilising the Hα line, the authors measured periodic variations in the non-thermal line widths. The indicator that the observed variation was torsional was a 180° phase delay between signals on the opposite sides of the chromospheric MBP, with the resulting chromospheric absorption profile shifts displayed in Mathioudakis et al. (2013).

5.1.4 Summary

It is clear from this growing body of evidence that the fast kink waves are ubiquitous throughout the chromosphere and present in almost all chromospheric features. However, the amplitudes of the waves can be very different for the various features (e.g., Table 3, Figure 22). We highlight this further with two histograms that show the distributions of wave amplitudes in the different structures. Although spicules have larger velocity amplitudes, it is unclear whether they carry a greater energy flux than other chromospheric features (energy flux is given roughly by $F \sim \rho c_{ph} v^2$, where c_{ph} is the phase speed of the wave and v is the velocity amplitude). For example, the density of fibrils appears to be $100 - 1000$ times that of spicules (Beckers 1972; Leenaarts et al. 2012), which gives approximately equal values for the energy flux in both features. (Note, this number isn't the total energy flux associated with spicules/fibrils since it doesn't account for differing filling factors of the structures, and therefore is simply the approximate energy flux per wave packet.) The fate of the observed wave energy is likely to be different. Spicules have a connection to the corona and the observations of Okamoto & De Pontieu (2011) suggest that some of the waves leave the chromosphere to deposit their energy elsewhere.

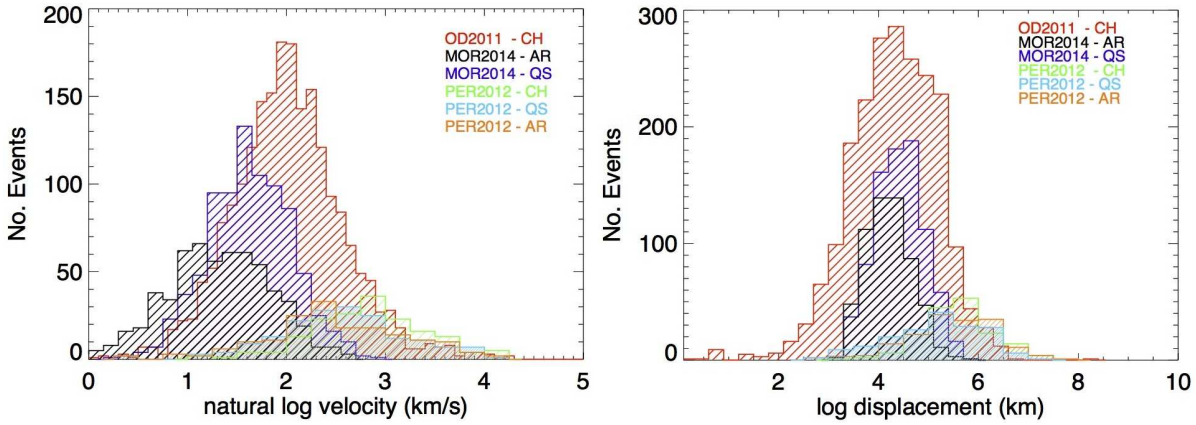

Fig. 22 Histograms showing the distributions of velocity (left) and displacement (right) amplitudes for different chromospheric features. The labels correspond to: OD2011 – Okamoto & De Pontieu (2011); MOR2014 – Morton et al. (2014); PER2012 – Pereira et al. (2012).

Fibrils, on the other hand, appear to be closed to the upper atmosphere, which means the energy likely stays contained in the chromosphere. It is then likely that the waves within these two structures play different roles in energy transport through the solar atmosphere.

5.2 Magneto-seismology

Solar magnetoseismology (SMS) has its origins in exploiting MHD oscillations in the corona to determine the physical conditions in the local plasma (Uchida 1970; Roberts et al. 1984). To date, there have been numerous successful applications in the corona (i.e., coronal seismology) with significant focus on fast MHD kink waves (e.g., Nakariakov & Verwichte 2005; Ruderman & Erdélyi 2009; Andries et al. 2009). However, the associated coronal scale-heights and time-scales for evolution are typically (much) larger than chromospheric values. Fortunately, most of the assumptions used to derive the SMS techniques for coronal applications are still largely applicable to oscillations in chromospheric structures. However, in the chromosphere one needs to carefully consider the influence of flows on the SMS techniques because the effects of such phenomena become important when the flow speed, U, is on the order of the kink speed, c_k. This can be seen in the governing wave equation when flow is included, e.g., Morton & Erdélyi (2009), Ruderman (2011), Soler et al. (2011) and Terradas et al. (2011), where terms on the order of $(U/c_k)^2$ are present. The full development of SMS techniques that include the influence of flows should be the next step for those who are theoretically minded and would improve the applicability of SMS to a wider selection of situations.

To date, very few applications of SMS have been made to chromospheric features. The first attempt was made by Kim et al. (2008), who were able to measure parameters for a few oscillatory events described in § 5.1.1. The authors use the following relationship,

$$B_0 = \sqrt{\frac{\mu_0}{2}} \frac{\lambda}{P} \sqrt{\rho_i + \rho_e} \,, \tag{17}$$

where B_0 is the magnetic field, μ_0 is the magnetic permeability, P is the period, ρ is the plasma density, λ is the wavelength, and the subscripts i and e refer to internal and external values, respectively[1]. The authors use previously measured spicules densities and values for the phase speed to derive the wavelength, thus estimating values of $10 - 80$ G for the magnetic field strength. The large range of values is partially due to the fact that density estimates for spicules vary by an order-of-magnitude. Secondly, the fact that the authors are not able to measure the phase speed directly also adds to the uncertainty.

A more advanced SMS application was given in Verth et al. (2011), where the authors exploited the measurements of a propagating fast kink wave along an active region spicule from He et al. (2009b), specifically the amplitude and phase speed values (see, § 5.1.1 and Figure 19). Combining these measured quantities with the theory that describes fast kink waves in a magnetic flux tube with longitudinal variations in the magnetic field and plasma density (e.g., Verth & Erdélyi 2008, Ruderman et al. 2008), the gradients in plasma density and magnetic field strength can be estimated. The normalised variation in each of these quantities is shown in Figure 23. Note, that the absolute values of quantities cannot

[1] Note, that the value B_0 is the root of the sum of the squares of the external and internal magnetic fields, i.e., $\langle B \rangle = \sqrt{B_i^2 + B_e^2}$.

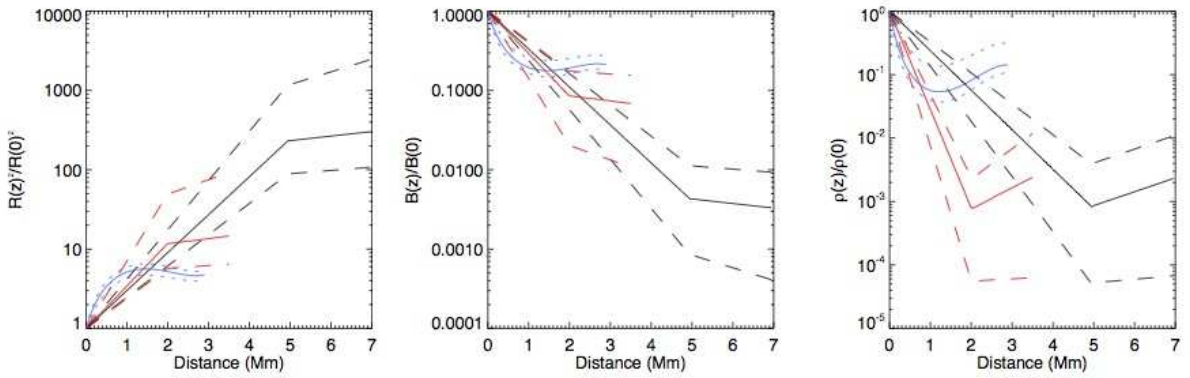

Fig. 23 Results from magneto-seismological inversions assuming no wave damping. Displayed are the normalised variations in area (left), magnetic field (middle) and plasma density (right). The results are from: spicules (black – Verth et al. 2011, blue – Morton 2014); and mottles (red – Kuridze et al. 2013). The dashed lines are the 95% confidence bounds for the seismologically determined results. Note that each observation does not start at the same atmospheric height, so the horizontal axis corresponds to the distance from the first measurement along the spicule. Note that the results here come from either limb or disk observations, which could mean line-of-sight effects may play a role in differences between them.

be measured from the observations. Additional information would be required to do this, i.e., a value for the magnetic field or density at a particular height.

The general trend measured for the plasma density gradient is that likely to be expected, i.e., the density is found to decrease with height. This shows agreement (within errors) with the gradient in plasma density estimated through other techniques, e.g., Makita (2003) from eclipse spectra. There is the suggestion that the density begins to increase towards the top of the spicule, although a constant or decreasing density profile is within the error bars. It is also expected the magnetic field weakens with height as it expands to fill the coronal volume as a result of magnetic structures increasing in size. This is precisely what is found from the SMS inversions. The inferred expansion suggests a significant increase in the spicule radius, a factor 10, which leads to a factor of 100 decrease in magnetic field strength. This may seem large, but let us assume that the spicule is anchored in a MBP with an initial field strength ~ 1000 G. The value at the spicule head is then 10 G, in line with approximate coronal values of magnetic field strength (e.g., Verwichte et al. 2013). The rate of decrease in the magnetic field strength is then ~ 0.25 G km^{-1}, which is comparable to the rate of decrease observed in sunspots and active regions between the photosphere and chromosphere (e.g., Leka & Metcalf 2003, and the discussion in § 4.1.2). Additionally, the seismologically derived expansion is less than the estimated upper bound for the expansion of flux tubes from the photosphere to the corona (Tsuneta et al. 2008b).

Similar analysis is performed by Kuridze et al. (2013) for a mottle observed on-disk. The results (Figure 23) suggest a similar variation in quantities to the inversion of Verth et al. (2011). The increase in radius up to 2 Mm is a factor of ~ 3 for both observations, and consequently the variation in magnetic field is also similar. Interestingly, the density gradient is steeper in the mottle and only decreases by a factor $\sim 10^{-3}$. This coherent behaviour is not unexpected as the density along the spicules should drop from chromospheric values ($\sim 10^{-9}$ kg m^{-3}) to coronal values ($\sim 10^{-12}$ kg m^{-3}). Morton (2014) recently undertook a study of a fast kink wave along a spicule that occurred in the penumbra of a sunspot. The inversions revealed similar variations in spicule expansion and magnetic field gradient to the previous two studies, although the gradients are steeper. Significantly, Morton (2014) was also able to directly measure the expansion along the spicule by fitting a Gaussian to the spicules cross-sectional flux profile. He found good agreement between the seismologically determined values and the directly measured value after taking into account optical effects from the telescope. The density decrease along the spicule was almost an order-of-magnitude less than that found in Verth et al. (2011) and Kuridze et al. (2013).

One feature that all these observations have in common is that the rate of change of magnetic field strength reduces drastically at a certain height, and perhaps surprisingly, the density appears to begin to increase again with height. The second of these quirks can easily be explained. Firstly, the amplitude of the wave is dependent upon the density (i.e., $\xi \propto \langle\rho\rangle^{-1/4}$- Morton 2014) and is independent of the magnetic field. Note that the relationship of the kink wave amplitude to density is similar to that found for the Alfvén wave. It is expected that the fast kinkfast kink waves will undergo some form of damped motion, with resonant absorption an excellent candidate for such damping (e.g., Goossens et al. 2011). The relations used for the SMS inversions do not take into account the possibility of damping. Hence, if any of the observed waves are being damped, the standard SMS technique will underestimate the gradient in density, and consequently gradients in expansion and magnetic field strength (as pointed out in Verth et al. 2011). If the

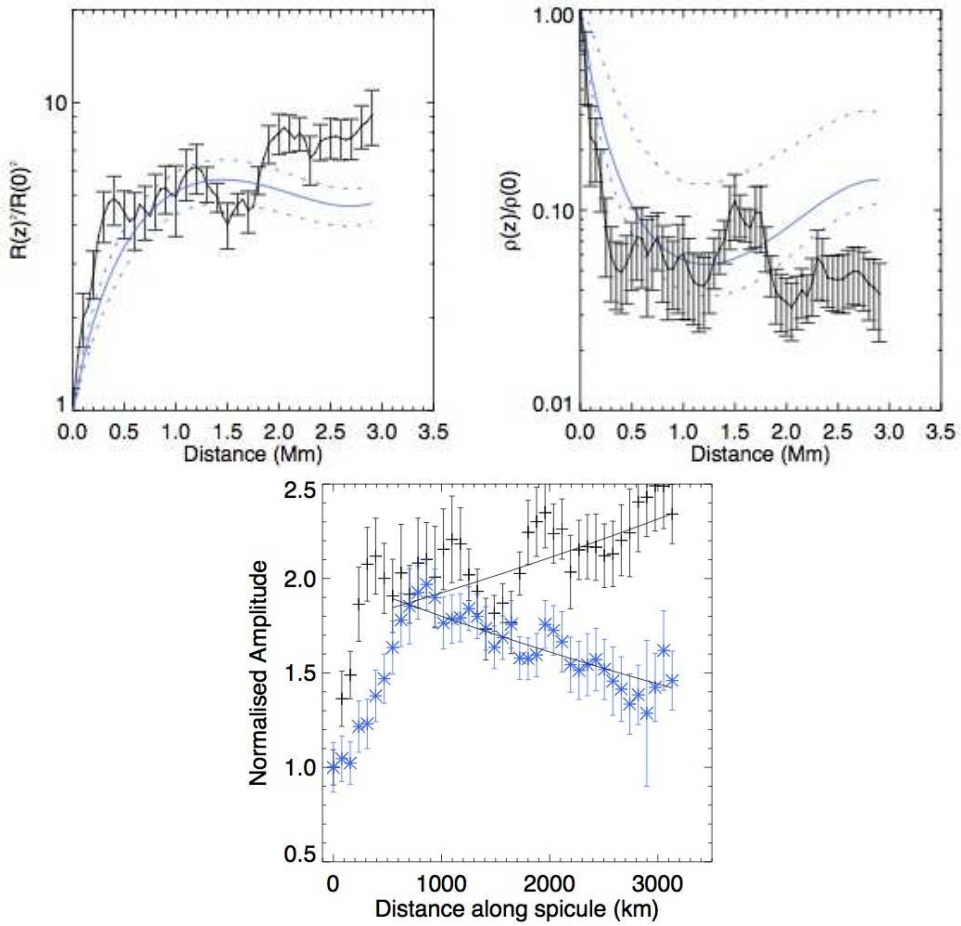

Fig. 24 Results from magneto-seismological inversions combining spicule width variations. Displayed are the normalised variations in area (upper-left) and plasma density (upper-right). The blue lines are the inversions shown in Figure 23. The black line in the upper-left panel shows the expansion inferred from the measurements of the Gaussian width of the spicule with σ error bars given. The black line in the upper-right panel is the density gradient determined using a combination of the measured width and measured phase speed. The lower panel displays the measured amplitude of an fast kink wave along a spicule (blue stars) and the amplitude determined from the measured expansion and the phase speed measurements (black crosses). The difference between the two amplitudes suggest the wave is damped as it propagates along the spicule. The black solid lines correspond to exponential fits to each amplitude profile. Image reproduced from Morton (2014).

evolution of the amplitude is dominated by the damping rather than the variation of plasma parameters, then it is likely that non-physical results will be obtained from the inversions. As Morton (2014) was able to measure the expansion along the spicule via another technique (for a comparison see Figure 24), this could be combined with the measured phase speed to derive the actual variation in density along the structure. As should be expected, the density decreases continuously along the spicule (Figure 24). Using this density profile, the expected amplitude variation along the spicule for an undamped wave was calculated, with comparison to the measured amplitude suggesting the spicule's wave motion was indeed damped (Figure 24 and see § 5.3 for further details). The damping is found to have a quality factor, ξ_E, equal to $\tau_D/P = L_D/\lambda \sim 0.34$, where τ_D is the damping time and L_D is the damping length.

The initial, rapid change in magnetic field strength inferred from all observations may also have a relatively straightforward explanation. Spicules are jets of chromospheric plasma that follow vertical field lines, reach well into the corona, and as a result may be departures from the traditional gravitationally stratified atmosphere. However, if it is assumed that the spicules are superimposed on the traditional atmospheric profile, then the external values for both density and magnetic field strength will rapidly decrease at the height at which the spicule crosses the transition region. This may also be related to the magnetic flux merging height, which depends on the flux distribution in the photosphere. If the magnetic flux distribution is of the small scale 'salt and pepper' format then the merging height will be quite low compared to a more simple large scale dipole source. The important point is that the merging height and the height of the transition region could vary over all atmospheric locations. This is suggested by the SMS results in Figure 23. Note, that while the external values of density and magnetic field may change drastically, the internal values along the spicule may

not. The measured variations are the average values of these quantities, which will reflect the average highly localised behaviour.

Finally, we mention that the fast kink waves are not the only useful tool for probing the chromosphere, but torsional Alfvén waves also have the potential to reveal information about the local plasma conditions. Inspired by the observations of Jess et al. (2009), Verth et al. (2010a, 2011) and Fedun et al. (2011) have demonstrated that the torsional motions can be used to map the magnetic field in the chromosphere. This is another exciting avenue for SMS and hopefully will be built upon with future observations.

5.3 Wave generation and damping

From the preceding sections it is apparent that the chromosphere is subject to ubiquitous incompressible motions, with the body of evidence for this ever increasing. This leaves us with two very pertinent questions: how are these waves generated and what is the fate of the energy that they transport?

The first of these questions is perhaps somewhat easier to provide answers to. It has been postulated that the horizontal component of the convective motions is able to excite incompressible motions (e.g., Hollweg 1972; Spruit 1981; Choudhuri et al. 1993) and this forms the basis for many simulations related to the heating of the solar atmosphere and solar wind acceleration via MHD waves (e.g., Cranmer & van Ballegooijen 2005; Suzuki & Inutsuka 2005; Fedun et al. 2011) and spicule formation (e.g, Matsumoto & Shibata 2010). Complementary mechanisms of wave generation may also be present. For example, p-modes (or more generally slow magnetoacoustic waves) can also excite fast MHD waves via mode conversion (Carlsson & Bogdan 2006), although this only occurs along inclined magnetic fields. Additionally, it is well known that magnetic reconnection can also release some of its energy in the form of MHD waves (e.g., Yokoyama & Shibata 1996), with periodic reconnection mechanisms also viable (e.g., McLaughlin et al. 2009). Observational evidence that demonstrates the excitation mechanisms of incompressible waves is very limited at present, and is typically restricted to isolated examples. Both He et al. (2009b) and Yurchyshyn et al. (2012) show examples of oscillating spicules with an inverted Y-shaped structure, which they suggest shows evidence of a reconnection event – following Shibata et al. (2007). Consequently, they put forward the idea that some of the energy released from the reconnection is used to generate the kink wave.

Evidence for mode conversion generating transverse waves in spicules has been offered by Jess et al. (2012b). The authors use the multiwavelength capabilities of the ROSA instrument to identify and examine the photospheric footpoints of the spicules. The spicules are observed to be rooted in MBPs found in G-band images, which correspond to strong regions of magnetic field (Berger & Title 2001; Jess et al. 2010c). The MBPs are found to display significant intensity oscillations that are upwardly propagating, and can be interpreted as slow magnetoacoustic waves. Importantly, the intensity oscillations are 90° out-of-phase across the bright point, suggesting a double 'piston-like' action. This out-of-phase behaviour leads to velocity gradients across the spicule and excites the fast kink wave. Hints at excitation mechanisms for incompressible waves in fibrils have also been reported in Morton et al. (2013, 2014). In Morton et al. (2013), the multiwavelength capabilities of the ROSA instrument are again exploited in an attempt to connect the dynamics of the photosphere to the chromosphere. The authors identify an MBP that is associated with the footpoints of fibrils and the bright point appears to exist within a photospheric vortex. It has been demonstrated that these photospheric vortices can generate significant Poynting flux (Shelyag et al. 2011, 2012; Moll et al. 2012; Wedemeyer-Böhm et al. 2012) and excite MHD waves (Fedun et al. 2011; Vigeesh et al. 2012; Shelyag et al. 2013). The authors observe quasi-periodic twisting motions of the chromospheric counterpart of the MBP that can be identified as torsional Alfvén waves. Additionally, there appears to be a coupling between the torsional motions of the large-scale magnetic structure and the transverse motions of the fibrils, although the underlying physics is unclear. While not apparently periodic, magnetic features that show evidence for uni-directional 'swirling' motion have also been identified in Ca II 8542 Å observations (Wedemeyer-Böhm & Rouppe van der Voort 2009). Wedemeyer-Böhm et al. (2012) related these motions to photospheric vorticities which had been observed previously by Bonet et al. (2008). It was also revealed that the emission in the upper solar atmosphere simultaneously increased, suggesting localised plasma heating during the lifetime of a swirl event.

A more general attempt at identifying the driver of fast kink waves in fibrils was undertaken in Morton et al. (2014). The authors measured the velocity power spectrum of the observed chromospheric waves in order to compare it to spectra measured from granular flows (e.g., Matsumoto & Kitai 2010; Stangalini et al. 2013) and motions of MBPs (Chitta et al. 2012). This involved measuring over 700 sinusoidal transverse displacements in fibrils in order to produce a statistically significant spectra. Comparison of the photospheric and chromospheric spectra demonstrated a good correlation between the gradients at low frequencies (Figure 25), hinting that the granular motions play a dominant role in

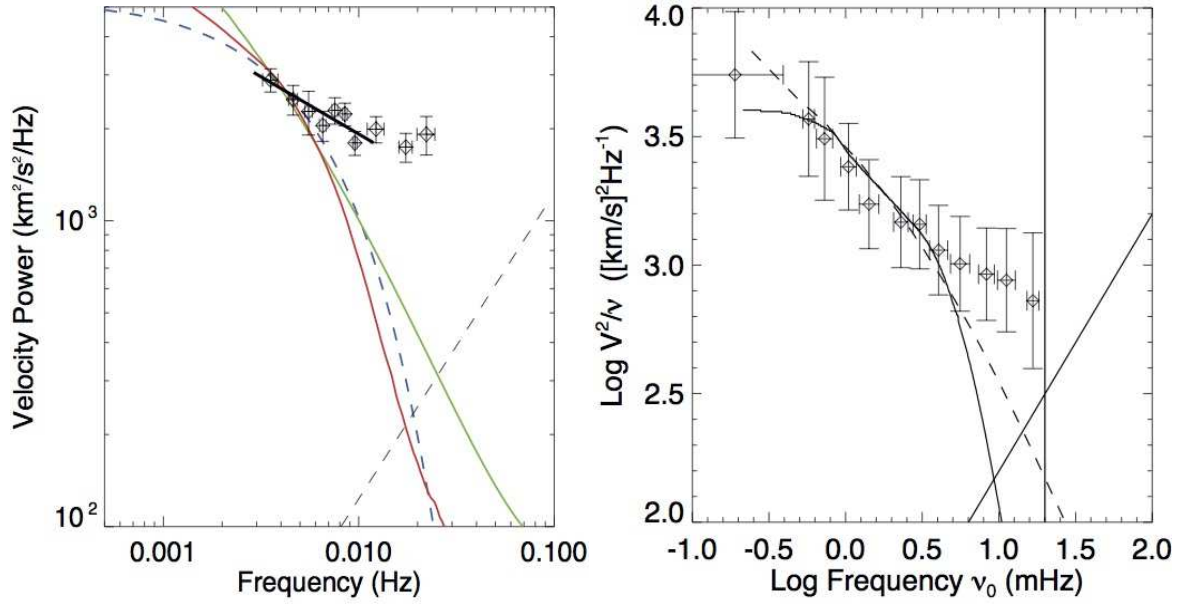

Fig. 25 Velocity power spectra of incompressible motions. The left panel shows the velocity power spectra measured from the transverse displacements of quiescent chromospheric fibrils (data points) in Morton et al. (2014). The coloured lines correspond to photospheric velocity power spectra from Matsumoto & Shibata (2010, red dash-dot line) and Chitta et al. (2012, green solid and blue dashed lines). The right hand panel is the velocity power spectra of transverse displacements of prominence threads from Hillier et al. (2013, data points). Again the over plotted lines show the photospheric power spectra.

generating the transverse waves in fibrils. These conclusions are given support from similar observations in prominences (Hillier et al. 2013), where the longer lifetimes of the prominence structures (relative to fibrils) allows the extension of the 'chromospheric' power spectra to even lower frequencies (Figure 25).

As for the fate of the observed waves, there have been few observational hints. This is partly due the short time-scales of the chromospheric structures, with both spicules and fibrils having lifetimes on the order of $100 - 300$ s (Pereira et al. 2012; Morton et al. 2014). This does not mean that the magnetic fields vary on such short time-scales, but is instead related to the variations in the dense plasma that defines the structures. The short visible lifetimes mean that it becomes difficult to track wave packets for an extended period of time, unfortunately reducing the chance of observing their full evolution. Additionally, short length-scales, both of the features ($\sim 4 - 10$ Mm) and the chromospheric scale heights ($500 - 1000$ km), means that fast propagating waves can travel along the structures in tens of seconds leading to large variations in the wave amplitudes and phase speeds. Hence, as suggested earlier, careful measurements of high-quality data is needed to reveal information regarding the details of the waves propagation over extend distances (see, § 5.2 for details on measurements of this type).

The first clue that incompressible waves suffer from wave damping at chromospheric heights came from He et al. (2009b). As discussed in § 5.2, the authors were able to measure the variation in amplitude of an embedded kink wave over an extended range of heights. An initial increase in amplitude is observed, followed by a decrease in amplitude which the authors suggested may be due to damping. However, it was not possible to prove this, as changes in plasma density can also lead to variations in amplitude, although it would seem unlikely that the spicule density would increase with height. A similar profile for the amplitude of a kink wave along a mottle was also observed in Kuridze et al. (2013). Very recently, a strong observational case was made for wave damping in spicules. Morton (2014) observed a similar amplitude evolution for a kink wave in a spicule as outlined by the two previous publications. However, a key step was that Morton (2014) was also able to directly measure the variation in the width of the spicule with height. This additional information was combined with the phase speed measurements allowing the true density profile along the spicule to be derived. Using this information, the expected variation in amplitude in the absence of wave damping was estimated, and it was demonstrated that the amplitude should have continued to increase with height (Figure 24). In light of the this additional information, wave damping was suggested as the cause for the observed amplitude profile, and allowed for an estimate of the quality factor ($\xi_E = 0.34$) and the frequency-independent α factor ($\alpha = L_D/P = 0.07$ Mm s^{-1}). These values suggested that the damping was significantly stronger than that associated with the damping of propagating coronal waves, where measured values are on the order of $\xi_E \sim 2.69$ and $\alpha \sim 1.6$ Mm s^{-1} (Verth et al. 2010b).

Morton et al. (2014) also provided an insight into the fate of the kink waves. The authors compared the velocity power spectrum measured from Coronal Multi-channel Polarimeter (CoMP; Tomczyk et al. 2008) observations of quiescent coronal loops (Tomczyk & McIntosh 2009) to the chromospheric velocity power spectrum of fibrils. The comparison demonstrated that the coronal power is significantly less than that observed in the chromosphere (some of which is likely due to the poorly resolved velocity amplitudes in the CoMP data), and that the coronal spectra has a much steeper power law. The steeper power law implies a frequency-dependent damping mechanism is in action between the chromosphere and corona, which dissipates higher frequency waves more efficiently. They put forward the idea that the kink waves are mode-converted via resonant absorption on their journey from the chromosphere to the corona, finding an estimate for the quality factor of $\xi_E = 1.35$ and $\alpha = 0.2$ Mm s^{-1}. These estimates are spatially averaged values, which are averaged over the distance from the chromosphere to the height of the CoMP measurements (~ 15 Mm). These results support the idea of enhanced damping of kink waves in the chromosphere and transition region compared to that found in the corona.

6 Future Directions and Concluding Remarks

The question of what heats the outer solar atmosphere to its multi-million degree temperatures has remained at the forefront of astrophysical research for well over 50 years now. In order to conclusively determine the key drivers, transportation processes and dissipation mechanisms we must strive to answer a number of outstanding fundamental science questions, notably: Where is the energy generated; is it locally produced in the outer solar atmosphere, or is it something which manifests below the photospheric layers and is transported outwards through the chromosphere to the corona? If it is the latter, then what physical processes allows this energy to propagate upwards against the steep temperature gradient intrinsically embedded within the solar atmosphere? Is the energy flux carried by magneto-hydrodynamic (MHD) waves, and if so, which mode(s) of oscillation plays a dominant role in the energy transfer? Then, ultimately, how does the wave energy flux dissipate in the form of localised heating, and what physical mechanisms instigate and support this energy conversion?

Of course, the challenging optically thick, photon starved, rapidly changing and magnetically complex nature of the chromosphere often deters observers and theorists alike. However, it is refreshing to see that significant strides are currently being made to detect and understand MHD wave phenomena in the lower solar atmosphere. Indeed, in recent years there has been a multitude of MHD wave observations documenting localised oscillations with sufficiently high energy densities to balance the monumental radiative losses experienced in the high-temperature outer-atmospheric environments. However, the increased radiative losses found in certain active regions place the dominant role MHD waves play more globally in some doubt. Furthermore, there is still a significant way to go until we fully understand the underlying physics and mechanics, since we are yet to physically observe wave dissipation and its subsequent conversion into heat. On the other hand, it is only more recently with the advent of high-order adaptive optics, high-efficiency imaging detectors and vastly improved data reduction and analysis tools that we have begun to probe MHD wave phenomena anywhere close to the intrinsic spatial and temporal scales it is believed to operate on. Ground- and space-based facilities, including IBIS, CRISP, Hinode/SOT, ROSA and HARDcam, have provided the necessary sensitivity to be able to not only detect MHD oscillations, but also to track their dynamic evolution as a function of spatial position, time, and perhaps most importantly, atmospheric height. Thus, we do not have to wait for future missions to increase our understanding – the currently available fleet of instruments can still be exploited to provide crucial pieces to the puzzle.

Looking towards the future, it is currently expected that high-cadence imagers (e.g., Hinode/SOT, ROSA and HARDcam) will be employed simultaneously alongside cutting-edge 2D spectropolarimeters (e.g., IBIS and CRISP) to obtain multiwavelength time series with the highest spatial, temporal and spectral resolutions currently achievable. Such datasets will allow key MHD wave parameters to be extracted with unprecedented accuracy, such as their amplitudes, propagation speeds and phase relationships. The multiwavelength nature of the data will allow detected MHD phenomena to be traced as a function of height, through to the uppermost regions of the solar chromosphere. Then, as these waves bombard the transition region interface, state-of-the-art space-borne satellites, such as IRIS (De Pontieu et al. 2014), will allow the spectroscopic signatures (including thermal widths, shock waves and rebound characteristics) to be fully investigated at the precise location where the steepest temperature gradient resides. Only a simultaneous and comprehensive imaging and spectral catalogue covering a vast array of atmospheric heights will allow observers to uncover the true extent of MHD-governed energy flow through the Sun's tenuous atmosphere. In particular, we draw the readers attention to some key questions that may be answered through the approaches outlined above, notably:

- It is apparent that chromospheric measurements show distinct variations in wave amplitudes for different structures (spicules, mottles, fibrils, etc.) and similar structures in different regions (quiet Sun, active regions, coronal holes, etc., Figure 22). Why? There are at least two potential explanations for this. One being that the variations are due to the differing local plasma conditions of each structure, while another is that different driving mechanisms are responsible for the waves in differing structures. A combination of the two is also possible. A detailed derivation of power spectra in the different structures may help to shed some light on this question.
- Why do measurements of uni-directional motions (i.e., upwardly or downwardly propagating) give significantly higher values for the mean velocity amplitude than the measurement of periodic variations? There seems no clear explanation for this at present. One potential option is that uni-directional motions are not waves and just the result of the relocation of the magnetic field by some unknown process.
- What is driving the diverse variety of MHD waves? Discovering what the main driving mechanism is for incompressible waves, and how this interplays with the omnipresent photospheric p-mode compressible waves, will play a vital role in assessing the validity of various wave heating models. Ultimately, understanding this will also allow the total amount of energy flux available for atmospheric heating to be determined reliably.
- What happens to the wave energy? Again, this is another important question for assessing current wave heating models. However, this question may be much harder to answer. The length-scales for the dissipation of wave energy may be much smaller than current resolution limits and even those planned for the near future, so it is unlikely that

direct evidence for dissipation will be found. Indirect signatures of wave dissipation may potentially be sought but, to the best of our knowledge, non have been suggested. One fate suggested for incompressible kink waves is that they are mode-converted into torsional Alfvén motions due to resonant coupling (e.g, Terradas et al. 2010). However, no direct evidence for this transfer of energy has yet been documented, requiring both imaging and spectroscopic data. While some studies of this nature are under way, it is unclear how straightforward it will be to interpret the Doppler-shift signatures (see, e.g., § 2).

It must be stressed that the above questions are not listed in order of importance. However, we feel that those listed have an overarching central importance when attempting to understand the long-standing problems of atmospheric heating and energy transfer through the chromosphere. In addition, we also highlight that there is huge potential for insights into the chromosphere via solar magnetoseismology (SMS) approaches. Almost every structure in the chromosphere shows detectable wave motion, and therefore there is a wealth of data that is currently awaiting to be exploited using SMS techniques. Thus, the answers to all of the key science questions detailed above will only arise through the novel use of high-resolution chromospheric datasets alongside the rapidly developing field of MHD seismology.

Acknowledgements D.B.J. wishes to thank the UK Science and Technology Facilities Council (STFC) for the award of an Ernest Rutherford Fellowship alongside a dedicated Research Grant. R.J.M is grateful to Northumbria University for their support via the award of an Anniversary Fellowship and the Leverhulme Trust (UK) for the award of an Early Career Fellowship. G.V. acknowledges the support of the Leverhulme Trust (UK). V.F. and D.B.J. are grateful to The Royal Society (Scientific Seminar Scheme) for support in organisation of the India–UK scientific seminar where the ideas contained within this paper were first discussed. S.D.T.G. thanks the Northern Ireland Department for Employment and Learning for a PhD studentship. I.G. would like to thank the University of Sheffield for a SHINE studentship.

References

Acton, L. W., Leibacher, J. W., Canfield, R. C., et al., 1982, *ApJ*, 263, 409
Alfvén, H., 1942, *Nature*, 150, 405
Anderson, L. S., & Athay, R. G., 1989, *ApJ*, 336, 1089
Andić, A., Chae, J., Park, H., et al., 2013, *Sol. Phys.*, 288, 55
Andries, J. & van Doorsselaere, T. & Roberts, B. & Verth, G. & Verwichte, E. & Erdélyi, R., 2009, *Space Sci. Rev.*, 149, 3
Antonucci, E., Dennis, B. R., Gabriel, A. H., & Simnett, G. M., 1985, *Sol. Phys.*, 96, 129
Antonucci, E., Gabriel, A. H., & Dennis, B. R., 1984, *ApJ*, 287, 917
Arber, T. D., Longbottom, A. W., Gerrard, C. L., & Milne, A. M., 2001, *J. Comput. Phys.*, 171, 151
Asai, A., Shimojo, M., Isobe, H., et al., 2001, *ApJL*, 562, L103
Aschwanden, M. J., de Pontieu, B., Schrijver, C. J., & Title, A. M., 2002, *Sol. Phys.*, 206, 99
Aschwanden, M. J., Fletcher, L., Schrijver, C. J., & Alexander, D., 1999, *ApJ*, 520, 880
Aschwanden, M. J., Nakariakov, V. M., & Melnikov, V. F., 2004, *ApJ*, 600, 458
Aschwanden, M. J., Nightingale, R. W., Andries, J., Goossens, M., & Van Doorsselaere, T., 2003, *ApJ*, 598, 1375
Athay, R. G., & White, O. R., 1978, *ApJ*, 226, 1135
Athay, G. R., & White, O. R., 1979a, *ApJ Supp.*, 39, 333
Athay, R. G., & White, O. R. 1979b, *ApJ*, 229, 1147
Ballai, I., Jess, D. B., & Douglas, M., 2011, *A&A*, 534, A13
Balthasar, H., Collados, M., & Muglach, K., 2000, Astronomische Nachrichten, 321, 121
Balthasar, H., Wiehr, E., & Kueveler, G., 1987, *Sol. Phys.*, 112, 37
Barthol, P., Gandorfer, A., Solanki, S. K., et al., 2011, *Sol. Phys.*, 268, 1
Baudin, F., Gabriel, A., Gibert, D., Palle, P. L., & Regulo, C., 1996, *A&A*, 311, 1024
Baumann, I., & Solanki, S. K., 2005, *A&A*, 443, 1061
Beck, C., Khomenko, E., Rezaei, R., & Collados, M., 2009, *A&A*, 507, 453
Beck, C., Rezaei, R., & Puschmann, K. G., 2012, *A&A*, 544, A46
Beck, C., Rezaei, R., & Puschmann, K. G., 2013a, *A&A*, 549, A24
Beck, C., Rezaei, R., & Puschmann, K. G., 2013b, *A&A*, 553, A73
Beck, C., Schmidt, W., Kentischer, T., & Elmore, D., 2005, *A&A*, 437, 1159
Beckers, J. M., 1968, *Sol. Phys.*, 3, 367
Beckers, J. M. 1972, *ARA&A*, 10, 73
Beckers, J. M., & Tallant, P. E., 1969, *Sol. Phys.*, 7, 351
Beeck, B., Collet, R., Steffen, M., et al., 2012, *A&A*, 539, A121
Bello González, N., & Kneer, F., 2008, *A&A*, 480, 265
Bello González, N., Flores Soriano, M., Kneer, F., & Okunev, O., 2009, *A&A*, 508, 941
Bello González, N., Flores Soriano, M., Kneer, F., Okunev, O., & Shchukina, N., 2010a, *A&A*, 522, A31
Bello González, N., Franz, M., Martínez Pillet, V., et al., 2010b, *ApJL*, 723, L134
Bennett, K., Roberts, B., & Narain, U., 1999, *Sol. Phys.*, 185, 41
Berlicki, A., Mein, P., & Schmieder, B., 2006, *A&A*, 445, 1127
Berger, T. E., & Title, A. M., 2001, *ApJ*, 553, 449
Berghmans, D., & Clette, F., 1999, *Sol. Phys.*, 186, 207
Biermann, L., 1948, Zeitschrift fur Astrophysics, 25, 161
Bloomfield, D. S., Lagg, A., & Solanki, S. K., 2007, *ApJ*, 671, 1005
Bloomfield, D. S., McAteer, R. T. J., Mathioudakis, M., Williams, D. R., & Keenan, F. P., 2004, *ApJ*, 604, 936

Bogdan, T. J., & Judge, P. G., 2006, Royal Society of London Philosophical Transactions Series A, 364, 313
Bonet, J. A., Márquez, I., Sánchez Almeida, J., Cabello, I., & Domingo, V., 2008, *ApJL*, 687, L131
Bonnet, R. M., 1981, *Space Sci. Rev.*, 29, 131
Bradshaw, S. J., Klimchuk, J. A., & Reep, J. W., 2012, *ApJ*, 758, 53
Brisken, W. F., & Zirin, H., 1997, *ApJ*, 478, 814
Brown, T. M., Stebbins, R. T., & Hill, H. A., 1978, *ApJ*, 223, 324
Bruls, J. H. M. J., Solanki, S. K., Rutten, R. J., & Carlsson, M., 1995, *A&A*, 293, 225
Caffau, E., Ludwig, H.-G., Steffen, M., Freytag, B., & Bonifacio, P., 2011, *Sol. Phys.*, 268, 255
Cally, P. S., 1986, *Sol. Phys.*, 103, 277
Cameron, R., Schüssler, M., Vögler, A., & Zakharov, V., 2007, *A&A*, 474, 261
Cao, W., Gorceix, N., Coulter, R., et al., 2010, Astronomische Nachrichten, 331, 636
Carlsson, M. & Bogdan, T. J., 2006, Royal Society of London Philosophical Transactions Series A, 364, 395
Carlsson, M., & Leenaarts, J., 2012, *A&A*, 539, A39
Carlsson, M., & Stein, R. F., 1992, *ApJL*, 397, L59
Carlsson, M., & Stein, R. F., 1995, *ApJL*, 440, L29
Carlsson, M., & Stein, R. F., 1997, *ApJ*, 481, 500
Cauzzi, G., Reardon, K., Rutten, R. J., Tritschler, A., & Uitenbroek, H., 2009, *A&A*, 503, 577
Cauzzi, G., Reardon, K. P., Uitenbroek, H., et al., 2008, *A&A*, 480, 515
Cavallini, F., 2006, *Sol. Phys.*, 236, 415
Centeno, R., Collados, M., & Trujillo Bueno, J., 2006, *ApJ*, 640, 1153
Centeno, R., Trujillo Bueno, J., & Asensio Ramos, A., 2010, *ApJ*, 708, 1579
Chen, Y., Feng, S. W., Li, B., et al., 2011, *ApJ*, 728, 147
Chen, Y., Song, H. Q., Li, B., et al., 2010, *ApJ*, 714, 644
Chitta, L. P., van Ballegooijen, A. A., Rouppe van der Voort, L., DeLuca, E. E., & Kariyappa, R., 2012, *ApJ*, 752, 48
Cho, K.-S., Bong, S.-C., Chae, J., Kim, Y.-H., & Park, Y.-D., 2010, *ApJ*, 723, 440
Cho, K.-S., Bong, S.-C., Chae, J., et al., 2013, *Sol. Phys.*, 288, 23
Chou, D.-Y., Liang, Z.-C., Yang, M.-H., Zhao, H., & Sun, M.-T., 2009, *ApJL*, 696, L106
Choudhuri, A. R., Auffret, H., & Priest, E. R., 1993, *Sol. Phys.*, 143, 49
Christopoulou, E. B., Georgakilas, A. A., & Koutchmy, S., 2000, *A&A*, 354, 305
Christopoulou, E. B., Georgakilas, A. A., & Koutchmy, S., 2001, *A&A*, 375, 617
Collados, M., Bettonvil, F., Cavaller, L., et al., 2010, Astronomische Nachrichten, 331, 615
Couvidat, S., 2013, *Sol. Phys.*, 282, 15
Cranmer, S. R. & van Ballegooijen, A. A., 2005, *ApJ Supp.*, 156, 265
Criscuoli, S., Del Moro, D., Giannattasio, F., et al., 2012, *A&A*, 546, A26
Crockett, P. J., Jess, D. B., Mathioudakis, M., & Keenan, F. P., 2009, *MNRAS*, 397, 1852
Crockett, P. J., Mathioudakis, M., Jess, D. B., et al., 2010, *ApJL*, 722, L188
Cuntz, M., Rammacher, W., & Musielak, Z. E., 2007, *ApJL*, 657, L57
Curdt, W., Wilhelm, K., Feng, L., & Kamio, S., 2008, *A&A*, 481, L61
de la Cruz Rodríguez, J., Socas-Navarro, H., Carlsson, M., & Leenaarts, J., 2012, *A&A*, 543, A34
De Moortel, I., 2009, *Space Sci. Rev.*, 149, 65
De Moortel, I., & Brady, C. S., 2007, *ApJ*, 664, 1210
De Moortel, I., & Hood, A. W., 2003, *A&A*, 408, 755
De Moortel, I., & Hood, A. W., 2004, *A&A*, 415, 705
De Moortel, I., Ireland, J., Hood, A. W., & Walsh, R. W., 2002, *A&A*, 387, L13
De Moortel, I., Ireland, J., & Walsh, R. W., 2000, *A&A*, 355, L23
De Pontieu, B., Carlsson, M., Rouppe van der Voort, L. H. M., et al., 2012, *ApJL*, 752, L12
De Pontieu, B., McIntosh, S. W., Carlsson, M., et al., 2011, Science, 331, 55
De Pontieu, B., Erdélyi, R., & James, S. P., 2004, *Nature*, 430, 536
De Pontieu, B., McIntosh, S. W., Carlsson, M., et al., 2007a, Science, 318, 1574
De Pontieu, B., McIntosh, S., Hansteen, V. H., et al., 2007b, *PASJ*, 59, 655
De Pontieu, B., Title, A. M., Lemen, J. R., et al., 2014, *Sol. Phys.*, 289, 2733
Deforest, C. E., & Gurman, J. B., 1998, *ApJ*, 501, L217
Delaboudinière, J.-P., Artzner, G. E., Brunaud, J., et al., 1995, *Sol. Phys.*, 162, 291
Demchenko, B. I., Minasyants, G. S., Makarenko, N. G., & Obashev, S. O., 1985, Astronomicheskij Tsirkulyar, 1360, 3
Deubner, F.-L., 1971, *Sol. Phys.*, 17, 6
Deubner, F.-L., 1974, *Sol. Phys.*, 39, 31
Deubner, F.-L., 1975, *Sol. Phys.*, 40, 333
Domingo, V., Fleck, B., & Poland, A. I., 1995, *Sol. Phys.*, 162, 1
Dorotovič, I., Erdélyi, R., Freij, N., Karlovský, V., & Márquez, I., 2014, *A&A*, 563, A12
Dorotovič, I., Erdélyi, R., & Karlovský, V., 2008, IAU Symposium, 247, 351
Dröoge, F., 1967, *ZAp*, 66, 200
Dunn, R. B., 1969, *S&T*, 38, 368
Dunn, R. B., & Zirker, J. B., 1973, *Sol. Phys.*, 33, 281
Ebadi, H., Zaqarashvili, T. V., & Zhelyazkov, I., 2012, *Ap&SS*, 337, 33
Edwin, P. M., & Roberts, B., 1983, *Sol. Phys.*, 88, 179
Erdélyi, R., 1997, *Sol. Phys.*, 171, 49
Erdélyi, R., & Fedun, V., 2006a, Physics of Plasmas, 13, 032902
Erdélyi, R., & Fedun, V., 2006b, *Sol. Phys.*, 238, 41
Erdélyi, R., & Fedun, V., 2007, Science, 318, 1572
Erdélyi, R., & Fedun, V., 2007, *Sol. Phys.*, 246, 101
Erdélyi, R., & Fedun, V., 2010, *Sol. Phys.*, 263, 63
Erdélyi, R., & Hargreaves, J., 2008, *A&A*, 483, 285

Erdélyi, R., Luna-Cardozo, M., & Mendoza-Briceño, C. A. 2008, *Sol. Phys.*, 252, 305
Fedun, V., Verth, S., Jess, D., & Erdélyi, R., 2011, *ApJL*, 740, L46
Foukal, P., 1971, *Sol. Phys.*, 20, 298
Fossum, A., & Carlsson, M., 2005a, *Nature*, 435, 919
Fossum, A., & Carlsson, M., 2005b, *ApJ*, 625, 556
Fossum, A., & Carlsson, M., 2006, *ApJ*, 646, 579
Frisch, H., 1972, *Space Sci. Rev.*, 13, 455
Gabriel, M., 1992, *A&A*, 265, 771
Galloway, D. J., 1978, *MNRAS*, 184, 49P
Georgakilas, A. A., Christopoulou, E. B., & Koutchmy, S., 2000, *A&A*, 363, 306
Giovanelli, R. G., 1972, *Sol. Phys.*, 27, 71
Goedbloed, J. P. H., & Poedts, S., 2004, Principles of Magnetohydrodynamics, Cambridge University Press
Goldreich, P., & Keeley, D. A., 1977a, *ApJ*, 211, 934
Goldreich, P., & Keeley, D. A., 1977b, *ApJ*, 212, 243
Goodman, M. L., 2014, *ApJ*, 785, 87
Goossens, M., & De Groof, A. 2001, Physics of Plasmas, 8, 2371
Goossens, M., Andries, J., & Aschwanden, M. J. 2002, *A&A*, 394, L39
Goossens, M., Erdélyi, R., & Ruderman, M. S., 2011, *Space Sci. Rev.*, 158, 289
Goossens, M., Hollweg, J. V., & Sakurai, T., 1992, *Sol. Phys.*, 138, 233
Goossens, M., Soler, R., Terradas, J., Van Doorsselaere, T., & Verth, G., 2014, *ApJ*, 788, 9
Goossens, M., Terradas, J., Andries, J., Arregui, I., & Ballester, J. L., 2009, *A&A*, 503, 213
Goossens, M., Van Doorsselaere, T., Soler, R., & Verth, G., 2013, *ApJ*, 768, 191
Hall, J. C., 2008, Living Reviews in Solar Physics, 5, 2
Handy, B. N., Acton, L. W., Kankelborg, C. C., et al., 1999, *Sol. Phys.*, 187, 229
Hansteen, V. H., Carlsson, M., & Gudiksen, B., 2007, The Physics of Chromospheric Plasmas, 368, 107
Hasan, S. S., & Sobouti, Y., 1987, *MNRAS*, 228, 427
Hasan, S. S., Soltau, D., Kärcher, H., Süß, M., & Berkefeld, T., 2010, Astronomische Nachrichten, 331, 628
He, J., Marsch, E., Tu, C., & Tian, H., 2009a, *ApJL*, 705, L217
He, J.-S., Tu, C.-Y., Marsch, E., et al. 2009b, *A&A*, 497, 525
Heyvaerts, J., & Priest, E. R., 1983, *A&A*, 117, 220
Hill, H. A., & Stebbins, R. T., 1975, Seventh Texas Symposium on Relativistic Astrophysics, 262, 472
Hillier, A., Morton, R. J., & Erdélyi, R., 2013, *ApJL*, 779, L16
Hindman, B. W., & Jain, R., 2008, *ApJ*, 677, 769
Hirzberger, J., 2003, *A&A*, 405, 331
Hollweg, J. V., 1972, *ApJ*, 177, 255
Howard, R. F., 1992, *Sol. Phys.*, 137, 51
Huang, N. E., Shen, Z., Long, S. R., et al., 1998, Royal Society of London Proceedings Series A, 454, 903
Ilonidis, S., & Zhao, J., 2011, *Sol. Phys.*, 268, 377
Isobe, H., & Tripathi, D., 2006, *A&A*, 449, L17
Isobe, H., Tripathi, D., Asai, A., & Jain, R., 2007, *Sol. Phys.*, 246, 89
Jackiewicz, J., & Balasubramaniam, K. S., 2013, *ApJ*, 765, 15
Jefferies, S. M., McIntosh, S. W., Armstrong, J. D., et al., 2006, *ApJL*, 648, L151
Jess, D. B., Andić, A., Mathioudakis, M., Bloomfield, D. S., & Keenan, F. P., 2007, *A&A*, 473, 943
Jess, D. B., De Moortel, I., Mathioudakis, M., et al., 2012a, *ApJ*, 757, 160
Jess, D. B., Mathioudakis, M., Browning, P. K., Crockett, P. J., & Keenan, F. P., 2010a, *ApJL*, 712, L111
Jess, D. B., Mathioudakis, M., Christian, D. J., Crockett, P. J., & Keenan, F. P., 2010b, *ApJL*, 719, L134
Jess, D. B., Mathioudakis, M., Christian, D. J., et al., 2010c, *Sol. Phys.*, 261, 363
Jess, D. B., Mathioudakis, M., Crockett, P. J., & Keenan, F. P., 2008a, *ApJL*, 688, L119
Jess, D. B., Mathioudakis, M., Erdélyi, R., et al., 2008b, *ApJ*, 680, 1523
Jess, D. B., Mathioudakis, M., Erdélyi, R., et al., 2009, Science, 323, 1582
Jess, D. B., Mathioudakis, M., & Keys, P. H., 2014, *ApJ*, 795, 172
Jess, D. B., Pascoe, D. J., Christian, D. J., et al., 2012b, *ApJL*, 744, L5
Jess, D. B., Reznikova, V. E., Van Doorsselaere, T., Keys, P. H., & Mackay, D. H., 2013, *ApJ*, 779, 168
Jess, D. B., Shelyag, S., Mathioudakis, M., et al., 2012c, *ApJ*, 746, 183
Kalkofen, W. 1997, *ApJL*, 486, L145
Kalkofen, W., 2007, *ApJ*, 671, 2154
Kalkofen, W., 2008, Journal of Astrophysics and Astronomy, 29, 163
Keil, S. L., Rimmele, T., Keller, C. U., et al., 2003, *Proc. SPIE*, 4853, 240
Keppens, R., & Martinez Pillet, V., 1996, *A&A*, 316, 229
Keys, P. H., Jess, D. B., Mathioudakis, M., & Keenan, F. P., 2011a, *A&A*, 529, A127
Keys, P. H., Mathioudakis, M., Jess, D. B., et al., 2011b, *ApJL*, 740, L40
Keys, P. H., Mathioudakis, M., Jess, D. B., et al., 2013, *MNRAS*, 428, 3220
Khomenko, E., & Collados, M., 2006, *ApJ*, 653, 739
Kiddie, G., De Moortel, I., Del Zanna, G., McIntosh, S. W., & Whittaker, I., 2012, *Sol. Phys.*, 279, 427
Kim, Y.-H., Bong, S.-C., Park, Y.-D., et al., 2008, Journal of Korean Astronomical Society, 41, 173
King, D. B., Nakariakov, V. M., Deluca, E. E., Golub, L., & McClements, K. G., 2003, *A&A*, 404, L1
Kiselman, D., Pereira, T. M. D., Gustafsson, B., et al., 2011, *A&A*, 535, A14
Klein, R. I., Kalkofen, W., & Stein, R. F., 1976, *ApJ*, 205, 499
Klein, R. I., Stein, R. F., & Kalkofen, W., 1978, *ApJ*, 220, 1024
Klimchuk, J. A., 2012, Journal of Geophysical Research (Space Physics), 117, A16
Klimchuk, J. A., & Bradshaw, S. J. 2014, *ApJ*, 791, 60
Klimchuk, J. A., & Cargill, P. J., 2001, *ApJ*, 553, 440

Knoelker, M., & Schuessler, M., 1988, *A&A*, 202, 275
Kobanov, N. I., 2000, *Sol. Phys.*, 196, 129
Kobanov, N. I., & Chelpanov, A. A., 2014, Astronomy Reports, 58, 272
Kobanov, N. I., & Makarchik, D. V., 2004, *A&A*, 424, 671
Kobanov, N. I., Kolobov, D. Y., & Chupin, S. A., 2008, Astronomy Letters, 34, 133
Kobanov, N. I., Kolobov, D. Y., Chupin, S. A., & Nakariakov, V. M., 2011a, *A&A*, 525, A41
Kobanov, N. I., Kustov, A. S., Chupin, S. A., & Pulyaev, V. A., 2011b, *Sol. Phys.*, 273, 39
Kobanov, N. I., Kolobov, D. Y., & Makarchik, D. V., 2006, *Sol. Phys.*, 238, 231
Kobanov, N. I., Kolobov, D. Y., Sklyar, A. A., Chupin, S. A., & Pulyaev, V. A., 2009, Astronomy Reports, 53, 957
Kontogiannis, I., Tsiropoula, G., Tziotziou, K., & Georgoulis, M. K., 2010, *A&A*, 524, A12
Kopecký, M., & Mayer, P., 1953, Bulletin of the Astronomical Institutes of Czechoslovakia, 4, 90
Kopp, G., & Rabin, D., 1992, *Sol. Phys.*, 141, 253
Kosugi, T., Matsuzaki, K., Sakao, T., et al., 2007, *Sol. Phys.*, 243, 3
Krijger, J. M., Rutten, R. J., Lites, B. W., et al., 2001, *A&A*, 379, 1052
Krishna Prasad, S., Banerjee, D., & Gupta, G. R., 2011, *A&A*, 528, L4
Krishna Prasad, S., Banerjee, D., & Singh, J., 2012a, *Sol. Phys.*, 281, 67
Krishna Prasad, S., Banerjee, D., Van Doorsselaere, T., & Singh, J., 2012b, *A&A*, 546, A50
Kuridze, D., Morton, R. J., Erdélyi, R., et al., 2012, *ApJ*, 750, 51
Kuridze, D., Verth, G., Mathioudakis, M., et al., 2013, *ApJ*, 779, 82
Lagg, A., Woch, J., Solanki, S. K., & Krupp, N., 2007, *A&A*, 462, 1147
Lawrence, J. K., & Cadavid, A. C., 2012, *Sol. Phys.*, 280, 125
Lazrek, M., Baudin, F., Bertello, L., et al., 1997, *Sol. Phys.*, 175, 227
Leenaarts, J., Carlsson, M., Hansteen, V., & Rouppe van der Voort, L., 2009, *ApJL*, 694, L128
Leenaarts, J., Carlsson, M., & Rouppe van der Voort, L., 2012, *ApJ*, 749, 136
Leighton, R. B., 1960, IAUS, 12, 321
Leighton, R. B., Noyes, R. W., & Simon, G. W., 1962, *ApJ*, 135, 474
Leka, K. D. & Metcalf, T. R., 2003, *Sol. Phys.*, 212, 361
Lemen, J. R., Title, A. M., Akin, D. J., et al., 2012, *Sol. Phys.*, 275, 17
Li, T., & Zhang, J., 2012, *ApJL*, 760, L10
Lin, Y., 2011, *Space Sci. Rev.*, 158, 237
Lipartito, I., Judge, P. G., Reardon, K., & Cauzzi, G., 2014, *ApJ*, 785, 109
Lites, B. W., 1992, Proceedings of the NATO Advanced Research
Lites, B. W., & Chipman, E. G., 1979, *ApJ*, 231, 570
Lites, B. W., & Thomas, J. H., 1985, *ApJ*, 294, 682
Liu, W., & Ofman, L., 2014, *Sol. Phys.*, 67
Liu, Z., Xu, J., Gu, B.-Z., et al., 2014a, Research in Astronomy and Astrophysics, 14, 705
Liu, Z.-X., He, J.-S., & Yan, L.-M., 2014b, Research in Astronomy and Astrophysics, 14, 299
Livingston, W., Harvey, J. W., Malanushenko, O. V., & Webster, L., 2006, *Sol. Phys.*, 239, 41
López Ariste, A. & Casini, R., 2005, *A&A*, 436, 325
Luna, M., Knizhnik, K., Muglach, K., et al., 2014, *ApJ*, 785, 79
Luna, M., Terradas, J., Oliver, R., & Ballester, J. L., 2008, *ApJ*, 676, 717
Luna-Cardozo, M., Verth, G., & Erdélyi, R., 2012, *ApJ*, 748, 110
McAteer, R. T. J., Gallagher, P. T., Williams, D. R., et al., 2002, *ApJL*, 567, L165
McAteer, R. T. J., Gallagher, P. T., Williams, D. R., et al., 2003, *ApJ*, 587, 806
McIntosh, S. W., de Pontieu, B., Carlsson, M., et al., 2011, *Nature*, 475, 477
McLaughlin, J. A., De Moortel, I., Hood, A. W., & Brady, C. S., 2009, *A&A*, 493, 227
Madjarska, M. S., Vanninathan, K., & Doyle, J. G., 2011, *A&A*, 532, L1
Makita, M., 2003, Publications of the National Astronomical Observatory of Japan, 7, 1
Marsh, M. S., Walsh, R. W., & Plunkett, S., 2009, *ApJ*, 697, 1674
Martínez Pillet, V., Collados, M., Bellot Rubio, L. R., et al., 1999, Astronomische Gesellschaft Abstract Series, 15, 89
Martínez Pillet, V., Del Toro Iniesta, J. C., Álvarez-Herrero, A., et al., 2011, *Sol. Phys.*, 268, 57
Martinez Pillet, V., Moreno-Insertis, F., & Vazquez, M., 1993, *A&A*, 274, 521
Mathew, S. K., Solanki, S. K., Lagg, A., et al., 2004, *A&A*, 422, 693
Mathioudakis, M., Jess, D. B., & Erdélyi, R., 2013, *Space Sci. Rev.*, 175, 1
Matsumoto, T. & Kitai, R., 2010, *ApJL*, 716, L19
Matsumoto, T. & Shibata, K., 2010, *ApJ*, 710, 1857
Mein, N., & Mein, P., 1976, *Sol. Phys.*, 49, 231
Mein, N., & Mein, P., 1980, *A&A*, 84, 96
Mendoza-Briceño, C. A., Erdélyi, R., & Sigalotti, L. D. G., 2004, *ApJ*, 605, 493
Moll, R., Cameron, R. H., & Schüssler, M., 2012, *A&A*, 541, A68
Moreels, M. G., & Van Doorsselaere, T., 2013, *A&A*, 551, A137
Moreels, M. G., Goossens, M., & Van Doorsselaere, T., 2013, *A&A*, 555, A75
Morton, R. J., 2014, *A&A*, 556, 90
Morton, R. & Erdélyi, R., 2009, *A&A*, 605, 493
Morton, R. J., Erdélyi, R., Jess, D. B., & Mathioudakis, M., 2011, *ApJL*, 729, L18
Morton, R. J., Verth, G., Fedun, V., Shelyag, S., & Erdélyi, R., 2013, *ApJ*, 768, 17
Morton, R. J., Verth, G., Hillier, A., & Erdélyi, R., 2014, ApJ, 784, 29
Morton, R. J., Verth, G., Jess, D. B., et al., 2012, Nature Communications, 3, 1315
Muglach, K., Solanki, S. K., & Livingston, W. C., 1994, Solar Surface Magnetism, 127
Müller, D., Marsden, R. G., St. Cyr, O. C., & Gilbert, H. R., 2013, *Sol. Phys.*, 285, 25
Nagashima, K., Sekii, T., Kosovichev, A. G., et al., 2007, *PASJ*, 59, 631
Nakajima, H., Nishio, M., Enome, S., et al., 1994, IEEE Proceedings, 82, 705

Nakariakov, V. M., & Ofman, L., 2001, *A&A*, 372, L53
Nakariakov, V. M., & Roberts, B., 1995, *Sol. Phys.*, 159, 213
Nakariakov, V. M., & Verwichte, E., 2005, Living Reviews in Solar Physics, 2, 3
Nakariakov, V. M., Melnikov, V. F., & Reznikova, V. E., 2003, *A&A*, 412, L7
Nakariakov, V. M., Pascoe, D. J., & Arber, T. D., 2005, *Space Sci. Rev.*, 121, 115
Nakariakov, V. M., Ofman, L., Deluca, E. E., Roberts, B., & Davila, J. M., 1999, Science, 285, 862
Narain, U., & Ulmschneider, P., 1990, *Space Sci. Rev.*, 54, 377
Narain, U., & Ulmschneider, P., 1996, *Space Sci. Rev.*, 75, 453
Nikol'Skii, G. M. & Sazanov, A. A., 1967, *Sov. Astron.*, 10, 774
Noyes, R. W., & Leighton, R. B., 1963, *ApJ*, 138, 631
Nye, A. H., & Thomas, J. H., 1974, *Sol. Phys.*, 38, 399
Nye, A. H., & Thomas, J. H., 1976, *ApJ*, 204, 582
Ofman, L., & Aschwanden, M. J. 2002, *ApJL*, 576, L153
Ofman, L., Nakariakov, V. M., & Deforest, C. E., 1999, *ApJ*, 514, 441
Ofman, L., & Wang, T., 2002, *ApJL*, 580, L85
Ofman, L., Romoli, M., Poletto, G., Noci, G., & Kohl, J. L., 1997, *ApJL*, 491, L111
Ofman, L., Wang, T. J., & Davila, J. M., 2012, *ApJ*, 754, 111
Okamoto, T. J. & De Pontieu, B., 2011, *ApJL*, 736, L24
Osterbrock, D. E., 1961, *ApJ*, 134, 347
Pahlke, K.-D., & Wiehr, E., 1990, *A&A*, 228, 246
Parchevsky, K. V., & Kosovichev, A. G., 2007, *ApJL*, 666, L53
Parker, E. N., 1988, *ApJ*, 330, 474
Pasachoff, J. M., Noyes, R. W., & Beckers, J. M., 1968, *Sol. Phys.*, 5, 131
Patsourakos, S., Klimchuk, J. A., & Young, P. R., 2014, *ApJ*, 781, 58
Penn, M. J., & Labonte, B. J., 1993, *ApJ*, 415, 383
Pereira, T. M., De Pontieu, B., & Carlsson, M., 2012, *ApJ*, 759, 16
Pesnell, W. D., Thompson, B. J., & Chamberlin, P. C., 2012, *Sol. Phys.*, 275, 3
Petralia, A., Reale, F., Orlando, S., & Klimchuk, J. A., 2014, *A&A*, 567, 70
Pietarila, A., Aznar Cuadrado, R., Hirzberger, J., & Solanki, S. K., 2011, *ApJ*, 739, 92
Prakapavičius, D., Steffen, M., Kučinskas, A., et al., 2013, Memorie della Societa Astronomica Italiana Supplementi, 24, 111
Priest, E. R., 1986, *Sol. Phys.*, 104, 1
Priest, E., 2014, Magnetohydrodynamics of the Sun, Cambridge University Press
Priest, E. R., & Schrijver, K., 1999, *Sol. Phys.*, 190, 1
Puschmann, K. G., Kneer, F., Seelemann, T., & Wittmann, A. D., 2006, *A&A*, 451, 1151
Rammacher, W., & Ulmschneider, P., 2003, *ApJ*, 589, 988
Raouafi, N.-E., & Stenborg, G., 2014, *ApJ*, 787, 118
Reardon, K. P., Yang, Y. M., Muglach, K., & Warren, H. P., 2011, *ApJ*, 742, 119
Reznikova, V. E., Shibasaki, K., Sych, R. A., & Nakariakov, V. M., 2012, *ApJ*, 746, 119
Rimmele, T. R., Wagner, J., Keil, S., et al., 2010, *Proc. SPIE*, 7733,
Roberts, B., Edwin, P. M., & Benz, A. O., 1984, *ApJ*, 279, 857
Roberts, B., 1981a, *Sol. Phys.*, 69, 27
Roberts, B., 1981b, *Sol. Phys.*, 69, 39
Roberts, B., & Webb, A. R., 1978, *Sol. Phys.*, 56, 5
Rouppe van der Voort, L. H. M., De Pontieu, B., Hansteen, V. H., Carlsson, M., & van Noort, M., 2007, *ApJL*, 660, L169
Rouppe van der Voort, L., Leenaarts, J., de Pontieu, B., Carlsson, M., & Vissers, G., 2009, *ApJ*, 705, 272
Ruderman, M. S., 2011, *Sol. Phys.*, 271, 41
Ruderman, M. S., & Erdélyi, R., 2009, *Space Sci. Rev.*, 149, 199
Ruderman, M. S., & Roberts, B. 2002, *ApJ*, 577, 475
Ruderman, M. S., Verth, G., & Erdélyi, R., 2008, *ApJ*, 686, 694
Rüedi, I., Solanki, S. K., & Livingston, W. C., 1995, *A&A*, 293, 252
Rutten, R. J., 2007, in Astronomical Society of the Pacific Conference Series, Vol. 368, The Physics of Chromospheric Plasmas, ed. P. Heinzel, I. Dorotovič, & R. J. Rutten, 27
Rutten, R. J., 2013, in Astronomical Society of the Pacific Conference Series, Vol. 470, 370 Years of Astronomy in Utrecht, ed. G. Pugliese, A. de Koter, & M. Wijburg, 49
Rutten, R. J., Hammerschlag, R. H., Bettonvil, F. C. M., Sütterlin, P., & de Wijn, A. G., 2004, *A&A*, 413, 1183
Rutten, R. J., van Veelen, B., Sütterlin, P., 2008, *Sol. Phys.*, 251, 533
Sanchez Almeida, J., & Martinez Pillet, V., 1994, *ApJ*, 424, 1014
Sawyer, C., 1974, *Sol. Phys.*, 35, 63
Scharmer, G. B., Bjelksjo, K., Korhonen, T. K., Lindberg, B., & Petterson, B., 2003, *Proc. SPIE*, 4853, 341
Scharmer, G. B., Narayan, G., Hillberg, T., et al., 2008, *ApJL*, 689, L69
Scharmer, G. B., Pettersson, L., Brown, D. S., & Rehn, J., 1985, *Appl. Opt.*, 24, 2558
Schmidt, W., von der Lühe, O., Volkmer, R., et al., 2012, Astronomische Nachrichten, 333, 796
Schmieder, B., & Mein, N., 1980, *A&A*, 84, 99
Schou, J., Scherrer, P. H., Bush, R. I., et al., 2012, *Sol. Phys.*, 275, 229
Schwarzschild, M., 1948, *ApJ*, 107, 1
Scullion, E., Erdélyi, R., Fedun, V., & Doyle, J. G., 2011, *ApJ*, 743, 14
Sekse, D. H., Rouppe van der Voort, L., & De Pontieu, B., 2012, *ApJ*, 752, 108
Sekse, D. H., Rouppe van der Voort, L., & De Pontieu, B., 2013, *ApJ*, 764, 164
Shelyag, S., Cally, P. S., Reid, A., & Mathioudakis, M., 2013, *ApJL*, 776, L4
Shelyag, S., Fedun, V., Keenan, F. P., Erdélyi, R., & Mathioudakis, M., 2011, Annales Geophysicae, 29, 883
Shelyag, S., Mathioudakis, M., & Keenan, F. P., 2012, *ApJL*, 753, L22
Shen, Y., Ichimoto, K., Ishii, T. T., et al., 2014, *ApJ*, 786, 151

Shibata, K., Nakamura, T., Matsumoto, T., et al., 2007, Science, 318, 1591
Shimizu, T., Tsuneta, S., Hara, H., et al., 2011, *Proc. SPIE*, 8148,
Sobotka, M., Del Moro, D., Jurčák, J., & Berrilli, F., 2012, *A&A*, 537, A85
Sobotka, M., Švanda, M., Jurčák, J., et al., 2013, *A&A*, 560, A84
Sobotka, M., Vázquez, M., Bonet, J. A., Hanslmeier, A., & Hirzberger, J., 1999, *ApJ*, 511, 436
Socas-Navarro, H., McIntosh, S. W., Centeno, R., de Wijn, A. G., & Lites, B. W., 2009, *ApJ*, 696, 1683
Solanki, S. K., 1993, *Space Sci. Rev.*, 63, 1
Solanki, S. K., Barthol, P., Danilovic, S., et al., 2010, *ApJL*, 723, L127
Soler, R., Ballester, J. L., & Zaqarashvili, T. V., 2015, *A&A*, 573, AA79
Soler, R., Carbonell, M., & Ballester, J. L., 2013, *ApJ Supp.*, 209, 16
Soler, R., Terradas, J., Verth, G., & Goossens, M., 2011, *ApJ*, 736, 10
Spruit, H. C., 1981, *A&A*, 98, 155
Spruit, H. C., 1982, *Sol. Phys.*, 75, 3
Srivastava, A. K., & Goossens, M., 2013, *ApJ*, 777, 17
Srivastava, A. K., Dwivedi, B. N., & Kumar, M., 2013, *Ap&SS*, 345, 25
Srivastava, A. K., Zaqarashvili, T. V., Uddin, W., Dwivedi, B. N., & Kumar, P., 2008, *MNRAS*, 388, 1899
Stangalini, M., Berrilli, F., & Consolini, G., 2013, *A&A*, 559, A88
Stangalini, M., Del Moro, D., Berrilli, F., & Jefferies, S. M., 2011, *A&A*, 534, A65
Stangalini, M., Giannattasio, F., Del Moro, D., & Berrilli, F., 2012, *A&A*, 539, L4
Steiner, O., Hauschildt, P. H., & Bruls, J., 2001, *A&A*, 372, L13
Stenflo, J. O., 1985, *Sol. Phys.*, 100, 189
Suematsu, Y., Ichimoto, K., Katsukawa, Y., et al., 2008, in Astronomical Society of the Pacific Conference Series, Vol. 397, First Results From Hinode, ed. S. A. Matthews, J. M. Davis, & L. K. Harra, 27
Suematsu, Y., Tsuneta, S., Ichimoto, K., et al., 2008, *Sol. Phys.*, 249, 197
Sütterlin, P., 1998, *A&A*, 333, 305
Sütterlin, P., & Wiehr, E., 1998, *A&A*, 336, 367
Sütterlin, P., Rutten, R. J., & Skomorovsky, V. I., 2001, *A&A*, 378, 251
Sütterlin, P., Schröter, E. H., & Muglach, K., 1996, *Sol. Phys.*, 164, 311
Suzuki, T. K. & Inutsuka, S.-i., 2005, *ApJL*, 632, L49
Taroyan, Y., & Erdélyi, R., 2009, *Space Sci. Rev.*, 149, 229
Tavabi, E., Koutchmy, S., & Ajabshirizadeh, A., 2011, *New A.*, 16, 296
Terradas, J., Arregui, I., Verth, G., & Goossens, M., 2011, *ApJL*, 729, L22
Terradas, J., Goossens, M., & Verth, G., 2010, *A&A*, 524, A23
Terzo, S., Reale, F., Miceli, M., et al., 2011, *ApJ*, 736, 111
Testa, P., De Pontieu, B., Martínez-Sykora, J., et al., 2013, *ApJL*, 770, L1
Theurer, J., Ulmschneider, P., & Kalkofen, W., 1997, *A&A*, 324, 717
Thomas, J. H., Cram, L. E., & Nye, A. H., 1982, *Nature*, 297, 485
Title, A. M., Topka, K. P., Tarbell, T. D., et al., 1992, *ApJ*, 393, 782
Tomczyk, S. & McIntosh, S. W., 2009, *ApJ*, 697, 1384
Tomczyk, S., Card, G. L., Darnell, T., et al., 2008, *Sol. Phys.*, 247, 411
Torrence, C., & Compo, G. P., 1998, *Bull. Amer. Meteor.*, 79, 61
Trujillo Bueno, J., Merenda, L., Centeno, R., Collados, M., & Landi Degl'Innocenti, E., 2005, *ApJL*, 619, L191
Tsuneta, S., Acton, L., Bruner, M., et al., 1991, *Sol. Phys.*, 136, 37
Tsuneta, S., Ichimoto, K., Katsukawa, Y., et al., 2008a, *Sol. Phys.*, 249, 167
Tsuneta, S., Ichimoto, K., Katsukawa, Y., et al., 2008b, *ApJ*, 688, 1374
Tziotziou, K., Tsiropoula, G., Mein, N., & Mein, P., 2006, *A&A*, 456, 689
Tziotziou, K., Tsiropoula, G., Mein, N., & Mein, P., 2007, *A&A*, 463, 1153
Uchida, Y., 1970, *PASJ*, 22, 341
Uitenbroek, H., 1997, *Sol. Phys.*, 172, 109
Uitenbroek, H., 2001, *ApJ*, 557, 389
Uitenbroek, H., 2002, *ApJ*, 565, 1312
Uitenbroek, H., & Briand, C., 1995, *ApJ*, 447, 453
Ulmschneider, P., 1976, *Sol. Phys.*, 49, 249
Ulmschneider, P., Zaehringer, K., & Musielak, Z. E. 1991, *A&A*, 241, 625
Ulrich, R. K., 1970, *ApJ*, 162, 993
Uritsky, V. M., Davila, J. M., Viall, N. M., & Ofman, L., 2013, *ApJ*, 778, 26
Utz, D., Hanslmeier, A., Veronig, A., et al., 2013, *Sol. Phys.*, 284, 363
van Ballegooijen, A. A., Asgari-Targhi, M., Cranmer, S. R., & DeLuca, E. E. 2011, *ApJ*, 736, 3
Van Doorsselaere, T., Birtill, D. C. C., & Evans, G. R., 2009a, *A&A*, 508, 1485
Van Doorsselaere, T., Brady, C. S., Verwichte, E., & Nakariakov, V. M., 2008, *A&A*, 491, L9
Van Doorsselaere, T., Gijsen, S. E., Andries, J., & Verth, G., 2014, *ApJ*, 795, 18
Van Doorsselaere, T., Nakariakov, V. M., & Verwichte, E., 2007, *A&A*, 473, 959
Van Doorsselaere, T., Verwichte, E., & Terradas, J., 2009b, *Space Sci. Rev.*, 149, 299
van Noort, M., Hubeny, I., & Lanz, T., 2002, *ApJ*, 568, 1066
van Noort, M., Rouppe van der Voort, L., & Löfdahl, M. G., 2005, *Sol. Phys.*, 228, 191
Vecchio, A., Cauzzi, G., & Reardon, K. P., 2009, *A&A*, 494, 269
Verdini, A., & Velli, M., 2007, *ApJ*, 662, 669
Verth, G. & Erdélyi, R. 2008, *A&A*, 486, 1015
Verth, G., Erdélyi, R., & Goossens, M., 2010a, *ApJ*, 714, 1637
Verth, G., Erdélyi, R., & Jess, D. B., 2008, *ApJL*, 687, L45
Verth, G., Goossens, M., & He, J.-S., 2011, *ApJL*, 733, L15
Verth, G., Terradas, J., & Goossens, M., 2010b, *ApJL*, 718, L102

Verwichte, E., Nakariakov, V. M., Ofman, L., & Deluca, E. E., 2004, *Sol. Phys.*, 223, 77
Verwichte, E., Van Doorsselaere, T., Foullon, C., & White, R. S., 2013, *ApJ*, 767, 16
Vigeesh, G., Fedun, V., Hasan, S. S., & Erdélyi, R., 2012, *ApJ*, 755, 18
von Uexkuell, M., & Kneer, F., 1995, *A&A*, 294, 252
Vourlidas, A., Sanchez Andrade-Nuño, B., Landi, E., et al., 2010, *Sol. Phys.*, 261, 53
Wang, T., 2011, *Space Sci. Rev.*, 158, 397
Wang, T., Ofman, L., & Davila, J. M., 2013, *ApJL*, 775, L23
Wang, T. J., & Solanki, S. K., 2004, *A&A*, 421, L33
Wang, T. J., Ofman, L., Davila, J. M., & Mariska, J. T., 2009, *A&A*, 503, L25
Wedemeyer-Böhm, S. & Rouppe van der Voort, L., 2009, *A&A*, 507, L9
Wedemeyer-Böhm, S., Scullion, E., Steiner, O., et al., 2012, *Nature*, 486, 505
Wedemeyer-Böhm, S., Steiner, O., Bruls, J., & Rammacher, W., 2007, The Physics of Chromospheric Plasmas, 368, 93
White, O. R., & Athay, R. G., 1979a, *ApJ Supp.*, 39, 317
White, O. R., & Athay, R. G., 1979b, *ApJ Supp.*, 39, 347
Williamson, A., & Erdélyi, R., 2014, *Sol. Phys.*, 289, 1193
Withbroe, G. L., & Noyes, R. W., 1977, *ARA&A*, 15, 363
Wöger, F., von der Lühe, O., & Reardon, K., 2008, *A&A*, 488, 375
Woods, D. T., & Cram, L. E., 1981, *Sol. Phys.*, 69, 233
Yokoyama, T. & Shibata, K., 1996, *PASJ*, 48, 353
Yuan, D., Nakariakov, V. M., Huang, Z., et al., 2014a, *ApJ*, 792, 41
Yuan, D., Shen, Y., Liu, Y., et al., 2013, *A&A*, 554, A144
Yuan, D., Sych, R., Reznikova, V. E., & Nakariakov, V. M., 2014b, *A&A*, 561, A19
Yurchyshyn, V., Abramenko, V., Kosovichev, A., & Goode, P., 2014, *ApJ*, 787, 58
Yurchyshyn, V., Kilcik, A., & Abramenko, V., 2012, ArXiv e-prints
Zaqarashvili, T. V. & Erdélyi, R., 2009, *Space Sci. Rev.*, 149, 355
Zhang, Y. Z., Shibata, K., Wang, J. X., et al., 2012, *ApJ*, 750, 16
Zhugzhda, Y. D., & Nakariakov, V. M., 1999, Physics Letters A, 252, 222
Zhugzhda, Y. D., Balthasar, H., & Staude, J., 2000, *A&A*, 355, 347
Zirin, H., 1970, *S&T*, 39, 215
Zirin, H., 1972, *Sol. Phys.*, 22, 34
Zirin, H., 1988, Astrophysics of the sun (Cambridge and New York, Cambridge University Press)
Zirin, H., & Stein, A., 1972, *ApJL*, 178, L85